

The Role of P2X4 and P2X7 on the Formation of Ca²⁺ Microdomains in T cells

Dissertation

Zur Erlangung der Würde des Doktors der Naturwissenschaften
des Fachbereichs Biologie der Fakultät für Mathematik, Informatik und Naturwissenschaften
der Universität Hamburg

vorgelegt von

Valerie Johanna Brock

aus Celle, Deutschland

Hamburg, 2022

Folgende Gutachter empfehlen die Annahme der Dissertation:

Prof. Dr. rer. nat. Dr. med. habil. Andreas H. Guse

Prof. Dr. Eva Tolosa

Datum der Disputation: 21.09.2022

Content

CONTENT

ABBREVIATION	II
ABSTRACT	V
ZUSAMMENFASSUNG	VII
1. INTRODUCTION	1
1.1 Immunity	1
1.1.1 TCR stimulation	1
1.2 Calcium: Universal signaling ion	3
1.2.1 Ca ²⁺ signaling in T cells	3
1.3 Purinergic signaling in immunity	6
1.3.1 ATP release	8
1.3.2 P2X channels	9
1.3.3 P2Y receptors	11
1.3.4 Purinergic Ca ²⁺ signaling in T cells	12
1.4 Ca²⁺ imaging: Ca²⁺ indicators	13
1.4.1 Ca ²⁺ imaging: image restoration	15
1.5 Study objective	16
2. PUBLICATIONS	18
2.1. Publication I	18
2.1.1 Publication I: Contribution	36
2.2. Publication II	37
2.2.1 Publication II: Contribution	51
2.2.2 Publication II: Paper of the Month	52
3. DISCUSSION	53
3.1 Summary of the results implemented in this thesis	53
3.2 Ca²⁺ signaling: image restoration	53
3.3 The complexity of the Ca²⁺ channel network	55
3.4 P2X4 and P2X7: structural and functional differences	57
3.5 ATP release	61
3.6 Species-dependent differences: transferability of mouse data	63
3.7 Cell type-specific signaling and channelopathy	65
3.8 Outlook	68
REFERENCES	71
FIGURE INDEX	92
ORAL AND POSTER PRESENTATIONS	93
EIDESSTÄTLICHE VERSICHERUNG	94
ACKNOWLEDGEMENTS	95

Abbreviation

Abbreviation

A, Ala	alanine
AC	adenylate cyclase
ADP	adenosine diphosphate
AM	acetoxymethyl
AMD	age-related macular degeneration
AMP	adenosine monophosphate
AP	activator protein
APC	antigen-presenting cell
approx.	approximate
ARTC2.2	ecto-adenosine diphosphate-ribosyltransferase C2.2
ATP	adenosine 5'-triphosphate
BD	blind deconvolution
BCR	B cell receptor
C, Cys	cysteine
[Ca ²⁺] _i	free cytosolic calcium concentration
CAD	CRAC activation domain
cADPR	cyclic adenosine diphosphate ribose
CALHM1	calcium homeostasis modulator 1
CaM	calmodulin
cAMP	cyclic adenosine monophosphate
CaV	voltage-activated calcium channel
CBX	carbenoxolone
CC1	coiled-coil 1 region
CLL	chronic lymphocytic leukemia
CNX	connexin hemichannels
CR	calretinin
CRAC	calcium release activated calcium (channel)
DAG	diacylglycerol
DC	dendritic cell
DPA	dipicolylamine
E, Glu	glutamic acid
ectodomain	extracellular domain
EF-SAM	EF-hands and sterile α motif
eNTPDase1	ecto-nucleoside triphosphate diphosphohydrolase 1
ER	endoplasmic reticulum
ERK	extracellular signal-regulated kinase
FRET	Förster fluorescence resonance energy transfer
Gd ³⁺	gadolinium
GECI	genetically encoded calcium indicator
GFP	Green Fluorescence Protein
GPCR	heterotrimeric guanine nucleotide-binding protein-coupled receptor
G protein	heterotrimeric guanine nucleotide-binding protein
H, His	histidine
hMSC	human bone marrow-derived mesenchymal stem cells

Abbreviation

HN1L	hematological and neurological expressed 1-like protein
hP2X3	human P2X3
HPLC	high performance liquid chromatography
I, Ile	isoleucine
IP ₃	D- <i>myo</i> -inositol 1,4,5-trisphosphate
IP ₃ R	D- <i>myo</i> -inositol 1,4,5-trisphosphate receptor
IRF	interferon regulatory factor
ITAM	immunoreceptor tyrosine-based activation motif
JPT2	Jupiter microtubule-associated homolog 2
K _d	effective dissociation constant
L, Leu	leucine
LAT	linker of activated T cells
M, Met	methionine
MAC	maxi-anion channel
MAM	mitochondria-associated membranes
MAP	mitogen-activated protein
MAIT	Mucosa-associated invariant T cells
MCU	mitochondrial calcium uniporter
NAD ⁺	nicotinamide adenine dinucleotide
NAADP	nicotinic acid adenine dinucleotide phosphate
NFAT	nuclear factor of activated T cells
NKG2D	activating natural killer cell receptor
NKT	natural killer T cells
P, Pro	proline
P1	adenosine receptor
P2	purinergic receptor
P2X	purinergic ligand-gated cation channels
P2Y	purinergic heterotrimeric guanine nucleotide-binding protein-coupled receptor
PANX1	pannexin-1 hemichannel
PIP ₂	phosphatidylinositol 4,5-bisphosphate
PKA	protein kinase A
PKC	protein kinase C
PLC γ 1	phospholipase C γ 1
PM	plasma membrane
PMCA	plasma membrane calcium transporter
pMHC	peptide-loaded major histocompatibility complex
PSF	point spread function
PTK	protein tyrosine kinase
Pyk2	proline-rich tyrosine kinase 2
R, Arg	arginine
rP2X7	rat P2X7
RYR	ryanodine receptor
S, Ser	serine
S1P	sphingosine-1-phosphate
SERCA	sarco/endoplasmic reticulum calcium ATPase
SH2	Src homology 2
SNP	single nucleotide polymorphism

Abbreviation

SNR	signal-to-noise ratio
SOAR	STIM1 ORAI activating region
SOCE	store-operated calcium entry
SR	sarcoplasmic reticulum
Src	sarcoma
STIM1	calcium sensors stromal interaction molecule 1
STIM2	calcium sensors stromal interaction molecule 2
T, Thr	threonine
TCR	T cell receptor
TLR	toll-like receptor
TM	transmembrane domain
TPC	two-pore channel
TRP	non-selective transient receptor potential
UDP	uridine diphosphate
UTP	uridine 5'-triphosphate
VNUT	vesicular nucleotide transporter
VRAC	volume-regulated anion channel
Y, Tyr	tyrosine
zfP2X4	zebrafish P2X4

Abstract

The adaptive immune response is initiated by the activation of T cells. Following this activation, calcium (Ca^{2+}) signals translate an external stimulus into intracellular responses. These signals are characterized by initial, spatiotemporally restricted Ca^{2+} microdomains in T cells. T cell receptor (TCR) stimulation triggers the formation of second messengers like *D-myo*-inositol 1,4,5-trisphosphate (IP_3), cyclic adenosine diphosphate ribose (cADPR) or nicotinic acid adenine dinucleotide phosphate (NAADP). The recently identified hematological and neurological expressed 1-like protein (HN1L)/ Jupiter microtubule-associated homolog 2 (JPT2) orchestrates the NAADP activating the ryanodine receptors (RyR) in the membrane of the endoplasmic reticulum (ER). The RyR releases Ca^{2+} from the ER. Thus, the Ca^{2+} release-activated channel (CRAC) ORAI1 initiates store-operated Ca^{2+} entry (SOCE) through the plasma membrane (PM). These spatiotemporally restricted Ca^{2+} signals influence downstream effects like the translocation of the nuclear factor of activated T cells (NFAT), which further stimulates the production of cytokines and cell proliferation.

The visualization of highly dynamic Ca^{2+} microdomain signals is challenging due to low signal-to-noise ratios (SNR). Computational image restoration is one approach to improve the quality of low SNR images. Hence, in this study, a deconvolution algorithm emphasizing the characteristics of low SNR fluorescence images was extended for image sequences to increase not only spatial resolution but also temporal resolution (2.1; Woelk et al., 2021). Common algorithms were adjusted for single-frame images but also used on image sequences regardless of the temporal relationships of a multi-frame series. The extended algorithm now emphasizes both, the spatial and temporal features of an image sequence. Moreover, it was tested on Ca^{2+} microdomain sequences measured with different setups and compared with common algorithms. Finally, the comparisons highlight the improvements of using our extended algorithm on Ca^{2+} microdomain visualization.

Additionally, in this thesis, for the first time, the purinergic ligand-gated cation channels (P2X) P2X4 and P2X7 were demonstrated to influence the formation of the local, highly dynamic Ca^{2+} microdomains before and after T cell stimulation (2.2; Brock et al., 2022). Thus, using a high-resolution live-cell imaging technique Ca^{2+} microdomains were shown to be significantly reduced in *P2rx4^{-/-}* and *P2rx7^{-/-}* T cells and cells incubated with pharmacological inhibitors or inhibiting nanobodies for these channels after TCR/CD3 stimulation. Removal of the extracellular adenosine 5' triphosphate (ATP), which activates the P2X channels, or inhibition of the ATP releasing channel pannexin-1 (PANX1), significantly decreased the number of Ca^{2+} microdomains after T cell activation. Interestingly, P2X4 and PANX1 but not P2X7 influence the formation of TCR/CD3-independent Ca^{2+} microdomains, indicating different time periods

Abstract

of channel activity. These results and further colocalization analysis, global Ca^{2+} imaging and expression or proliferation analysis reveal functional differences between P2X4 and P2X7 activity.

In summary, this thesis established a computational approach to significantly improve the resolution of dynamic Ca^{2+} motions in fluorescence image sequences with very low SNRs. Furthermore, this work highlights the previously unexpected influence of the purinergic channels P2X4, P2X7 and the ATP-releasing channel PANX1 on the formation of Ca^{2+} microdomains, the fine-tuning of which may direct the adaptive immune response.

Zusammenfassung

Die adaptive Immunantwort wird initiiert durch die Aktivierung von T Zellen. In Folge dieser Aktivierung wird durch Calcium (Ca^{2+}) Signale ein externer Stimulus in eine intrazelluläre Antwort übersetzt. Diese Ca^{2+} Signale sind in T Zellen durch sogenannte initiale, räumlich und zeitlich begrenzte Ca^{2+} Mikrodomänen charakterisiert. Durch die Stimulation des T Zellrezeptors (TCR) werden sekundäre Botenstoffe wie D-*myo*-Inositol 1,4,5-Trisphosphat (IP_3), zyklische Adenosindiphosphat Ribose (cADPR) oder Nikotinsäureadeninucleotidphosphat (NAADP) gebildet. Das kürzlich identifizierte Protein „hematological and neurological expressed 1-like protein“ (HN1L) / “Jupiter microtubule-associated homolog 2” (JPT2) interagiert mit NAADP und aktiviert so Ryanodin Rezeptoren (RZR) in der Membran des Endoplasmatischem Retikulums (ER). Ca^{2+} wird durch den RZR aus dem ER freigesetzt. Der durch Ca^{2+} -Freisetzung aktivierte Kanal (CRAC) ORAI1 initiiert im Folgenden den „store-operated Ca^{2+} entry“ (SOCE), dies führt zu einem Ca^{2+} Einstrom über die Plasmamembran (PM). Die lokal und zeitlich begrenzten Ca^{2+} Signale beeinflussen nachgeschaltete Effekte wie die Translokation des Transkriptionsfaktors „nuclear factor of activated T cells“ (NFAT), der wiederum die Produktion von Zytokinen und die Zellproliferation stimuliert.

Die Visualisierung der hochdynamischen Ca^{2+} Mikrodomänen ist aufgrund des geringen Signal-Rausch-Verhältnisses (SNR) eine Herausforderung. Computergestützte Bildwiederherstellung ist ein Ansatz zur Verbesserung der Qualität von Bildern mit niedrigem SNR. Daher wurde in dieser Studie ein Dekonvolutionsalgorithmus, der die Merkmale von Fluoreszenzbildern mit niedrigem SNR berücksichtigt, für Bildsequenzen erweitert, um nicht nur die räumliche, sondern auch die zeitliche Auflösung zu verbessern (2.1; Woelk et al., 2021). Die Algorithmen, die im Allgemeinen verwendet werden, sind oft auf Einzelbilder angepasst. Allerdings werden sie auch auf Bildsequenzen Bild-für-Bild angewendet, ohne die zeitlichen Beziehungen einer Mehrbildserie zu berücksichtigen. Der erweiterte Algorithmus in dieser Doktorarbeit geht nun sowohl auf die räumlichen als auch die zeitlichen Merkmale einer Bildsequenz ein. Darüber hinaus wurde er an Aufnahmen von Ca^{2+} Mikrodomänen getestet, die unter verschiedenen Bedingungen aufgenommen wurden, und mit herkömmlichen Algorithmen verglichen. Die Vergleiche zeigen eine deutliche Verbesserung, die unser erweiterter Algorithmus bei der Visualisierung von Ca^{2+} Mikrodomänen mit sich bringt.

Darüber hinaus wurde in dieser Arbeit zum ersten Mal gezeigt, dass die purinergen ligandengesteuerten Kationenkanäle (P2X) P2X4 und P2X7 die Bildung der lokalen, hochdynamischen Ca^{2+} Mikrodomänen vor und nach der Stimulation von T Zellen beeinflussen (2.2; Brock et al., 2022). So konnte mit Hilfe eines hochauflösenden „Live-Cell-Imaging“-

Zusammenfassung

Verfahrens gezeigt werden, dass Ca^{2+} Mikrodomänen in *P2rx4^{-/-}* und *P2rx7^{-/-}* T Zellen sowie in Zellen, die mit pharmakologischen Inhibitoren oder hemmenden Nanokörpern für diese Kanäle inkubiert wurden, nach einer TCR/CD3-Stimulation signifikant reduziert sind. Die Entfernung des extrazellulären Adenosintriphosphats (ATP), das die P2X-Kanäle aktiviert, oder die Hemmung des ATP-freisetzenden Kanals Pannexin-1 (PANX1) verringerte die Anzahl der Ca^{2+} Mikrodomänen nach der T Zell Aktivierung signifikant. Interessanterweise beeinflussen P2X4 und PANX1, nicht aber P2X7, die Bildung von TCR/CD3-unabhängigen Ca^{2+} Mikrodomänen, was auf unterschiedliche Zeitpunkte der P2X-Kanalaktivität hinweist. Diese Ergebnisse sowie Ko-Lokalisationsanalysen, globale Ca^{2+} Messungen und Expressions- bzw. Proliferationsanalysen weisen auf funktionelle Unterschiede zwischen P2X4 und P2X7 hin. Zusammenfassend zeigt diese Doktorarbeit einen computergestützten Ansatz auf, um die Auflösung von dynamischen Ca^{2+} Bewegungen in Fluoreszenzbildsequenzen mit sehr geringen SNRs deutlich zu verbessern. Darüber hinaus hebt diese Arbeit den bisher unerwarteten Einfluss der purinerger Kanäle P2X4, P2X7 und des ATP-freisetzenden Kanals PANX1 auf die Bildung von Ca^{2+} Mikrodomänen hervor, deren präzise geregelten Dynamiken die adaptive Immunantwort lenken könnten.

1 Introduction

1. Introduction

1.1 Immunity

Immunity is the ability of an individual to defend and protect itself against foreign cells such as pathogens, or other external stimuli. Therefore, the immune system is essential to achieve this defensive and protective function. It consists of two major pathways, the (i) innate and the (ii) adaptive immune response (Abbas et al., 2018). Both make use of specific cells and soluble components. The (i) innate immune response, which constitutes the natural or native immunity, acts immediately through for example (e.g.), macrophages, neutrophils, or dendritic cells (DCs), after the infiltration of a pathogen. The (ii) adaptive immune system is more specific and effective against many microbial antigens and can develop an immunological memory (Murphy et al., 2009). Within an adaptive immune response, lymphocytes can recognize antigens via specific antibodies to differentiate and mature.

There are two groups of lymphocytes, the B and T cells with diverse functions and antibody specificities and structures. While B cells recognize an antigen via the B cell receptor (BCR) and differentiate into memory cells or plasma cells afterwards (Harwood & Batista, 2010), naive T cells differentiate to effector or memory T cells after activation (Masopust & Schenkel, 2013). Effector T cells can be divided into different subtypes: the more prominent CD4⁺ helper T cell and CD8⁺ cytotoxic T cell subsets and into the CD4⁺ regulatory T cells, natural killer T (NKT) cells, $\gamma\delta$ T cells, as well as the Mucosa-associated invariant T (MAIT) cells (Abbas et al., 2018). The T cell subsets exhibit many functions, e.g. CD4⁺ T cells produce several cytokines to activate and recruit other effector cells, whereas CD8⁺ T cells kill infected cells (Abbas et al., 2018; Murphy et al., 2009).

1.1.1 TCR stimulation

T cells are key players of the adaptive immune response, and their activation and differentiation are highly regulated. The T cell receptor (TCR) is the starting point of a signaling cascade for translating extracellular signals into intracellular responses for cell-to-cell communication and protection against pathogens and toxins (Mariuzza et al., 2020).

The receptor signals in association with a multi-subunit signaling machinery, the CD3 coreceptor (Birnbaum et al., 2014). The TCR/CD3 complex consists of an $\alpha\beta$ or a $\gamma\delta$ TCR heterodimer noncovalently associated with invariant CD3 dimers, the CD3 $\gamma/\delta/\epsilon/\zeta$ subunits (Borst et al., 1984; Hwang et al., 2020; Mariuzza et al., 2020; Wucherpfennig et al., 2010). Initially, an antigen-presenting cell (APC) presents a peptide-loaded major histocompatibility complex (pMHC) class I or class II to the TCR and initializes signaling cascades (Pettmann et

1 Introduction

al., 2018). In addition to pMHC binding, the signal is transmitted via the CD3 immunoreceptor tyrosine-based activation motifs (ITAMs, Fig. 1.1) (Hwang et al., 2020). Co-stimulation of CD28 on the T cell surface by the, on APCs highly expressed, ligands B7.1 (CD80) and B7.2 (CD86) enhances T cell response by regulating the transmission of the signal and the formation of second messengers like IP₃, nicotinic acid adenine dinucleotide phosphate (NAADP) and cyclic adenosine diphosphate ribose (cADPR) (Acuto & Michel, 2003; Garçon et al., 2008).

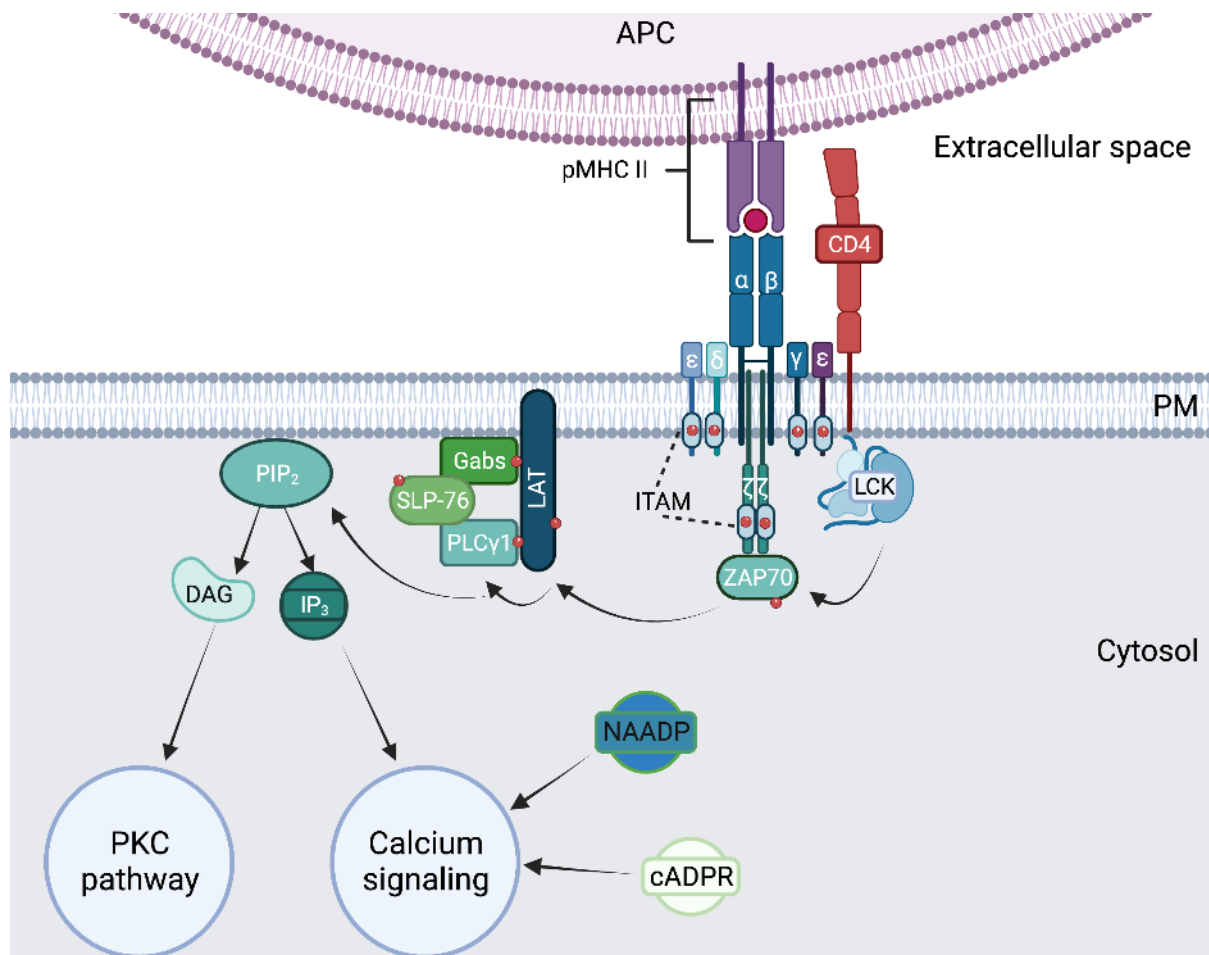


Figure 1.1: Illustration of TCR stimulation. An APC presents the pMHC to the TCR. The CD4 or CD8 coreceptors recruits Lck to the TCR. Lck phosphorylates (red dots) the ITAMS of the CD3 subunits and creates binding sites for the ZAP70 kinase. Moreover, ZAP70 phosphorylates LAT or SLP-76, which forms various signalosomes, like the clustering of LAT/Gabs/SLP-76, the activation of the Ras, mitogen activated protein (MAP) kinase/ extracellular – signal regulated kinase (ERK) pathway or the phosphorylation and activation of the phospholipase C γ 1 (PLC γ 1). Downstream signaling of Ca²⁺ is activated via the second messengers IP₃, NAADP and cADPR or PKC signaling via DAG formation. Modified from Hwang et al. 2020.

Protein tyrosine kinases (PTKs), like Lck, Fyn, and ZAP70, induce the phosphorylation of the ITAMs. Following the TCR stimulation, Lck is recruited by the colocalization of CD4 or CD8 coreceptors to pMHC molecules, which phosphorylates the ITAMs and forms binding sites for the ZAP70 kinase (Bu et al., 1995; Courtney et al., 2018). The quality and quantity of TCR stimulation can generate diverse downstream signals, like the phosphorylation of the linker of activated T cells (LAT) or SLP-76 by ZAP70 (Murphy et al., 2009). The phosphorylation of the LAT protein creates Src homology 2 (SH2) binding sites (Wange, 2000). The SH2 binding sites are essential for the formation of oligomeric signalosomes, like the clustering of

1 Introduction

LAT/Gαs/SLP-76, the activation of the Ras, mitogen-activated protein (MAP) kinase/extracellular signal-regulated kinase (ERK) pathway or the phosphorylation and activation of the phospholipase C γ 1 (PLC γ 1) (Abbas et al., 2018; Courtney et al., 2018; Wange, 2000). PLC γ 1 further hydrolyzes phosphatidylinositol 4,5-bisphosphate (PIP₂) generating D-myoinositol 1,4,5-trisphosphate (IP₃) and diacylglycerol (DAG), which induce calcium (Ca²⁺) signaling and the protein kinase C (PKC) pathway, respectively (Zeng et al., 2021). LAT and PLC γ 1 interact within a positive feedback loop: LAT not only activates PLC γ 1, but PLC γ 1 can also promote LAT cluster formation to protect its dephosphorylation by CD45 (Zeng et al., 2021).

1.2 Calcium: Universal signaling ion

Ca²⁺ is a universal signaling ion in eukaryotes (M. S. Islam, 2020). In cells, Ca²⁺ ions convert signals induced by external stimuli – like hormones, neurotransmitters, growth factors, antibodies, mechanical-, electrical-, temperature- and pH changes, microbial invasion or cytotoxic reagents – to internal responses by increasing the concentration of free cytosolic Ca²⁺ ([Ca²⁺]_i) from a basal level of approximate (approx.) 100 nM to approx. 1000 nM after stimulation (Bootman & Bultynck, 2020; Cahalan & Chandy, 2009). Ca²⁺ signals are highly controlled. On the one hand, Ca²⁺ signals are regulated precisely by several Ca²⁺ “buffering” or modulating systems – like plasma membrane Ca²⁺ transporters including ATPase (PMCA), Na⁺/Ca²⁺ exchanger and sarco/endoplasmic reticulum (SR/ER) Ca²⁺-ATPase (SERCA) or Ca²⁺ binding proteins including calmodulin (CaM) or calretinin (CR) (Bootman & Bultynck, 2020; Schwaller, 2020). On the other hand, Ca²⁺ releasing and entry mechanism – due to channel activities of the ryanodine receptor (RyR) and the IP₃ receptor (IP₃R) or the Ca²⁺ release activated channel (CRAC) ORA1 – increase [Ca²⁺]_i. These signaling machineries mediate many cellular processes, like apoptosis, aging, early embryonic development, synaptic transmission or gene expression (Bootman & Bultynck, 2020; M. S. Islam, 2020). The tremendous contrasts in Ca²⁺ concentration between the different cell compartments (cytosol: ~100 nM, ER: ~500 μ M, lysosomes: ~500 μ M) and the extracellular space (of approx. 1 to 2.5 mM) in resting cells allow for the rapid increase in [Ca²⁺]_i after stimulation (Bootman & Bultynck, 2020; Guse et al., 2021).

1.2.1 Ca²⁺ signaling in T cells

An accurate immune response requires a precisely coordinated signaling mechanism. Ca²⁺ serves as a very fast and highly controlled signaling ion acting intracellularly via Ca²⁺ receptors, channels, and sensing proteins.

1 Introduction

After TCR/CD3 stimulation, Ca^{2+} mobilizing second messenger molecules are formed, like NAADP, IP_3 or cADPR (Trebak & Kinet, 2019). NAADP is orchestrated by the hematological and neurological expressed 1-like protein (HN1L)/Jupiter microtubule-associated homolog 2 (JPT2) to activate RYR1s in the ER membrane or two-pore channels (TPCs) on lysosomes to release Ca^{2+} (Gunaratne et al., 2021; Roggenkamp et al., 2021). Moreover, IP_3 activates the IP_3R and cADPR the RYR2, both located at the ER membrane, to release Ca^{2+} (Trebak & Kinet, 2019). The decreasing luminal Ca^{2+} concentration inside the ER is sensed by the Ca^{2+} sensors stromal interaction molecules 1 (STIM1) and 2 (STIM2) located in the ER membrane, too (Brandman et al., 2007; Liou et al., 2005).

In resting cells, the paired EF-hands and sterile α motif (EF-SAM) domain of STIM binds Ca^{2+} and thereby represent an autoinhibitory mechanism of STIM (Zheng et al., 2011). STIM1 and 2 show structural differences within the EF-SAM domain. The STIM1 EF-SAM domain has a higher Ca^{2+} affinity and a lower SAM stability compared to STIM2, making STIM1 less responsive to small changes in ER Ca^{2+} (Brandman et al., 2007; Zheng et al., 2011). ER depletion results in a conformational change of the coiled-coil 1 region (CC1) and STIM1 ORAI activating region or CRAC activation domain (SOAR/CAD) of STIM protein. Thereby, STIM extends via the CC1 the SOAR/CAD from the ER membrane to the plasma membrane (PM) to interact with ORAI1 to activate this Ca^{2+} channel and mediate store-operated Ca^{2+} entry (SOCE) (Gudlur et al., 2020; Hirve et al., 2018).

Following TCR/CD3 stimulation, Ca^{2+} modulating systems, like mitochondrial Ca^{2+} uptake via the mitochondrial Ca^{2+} uniporters (MCUs) or the SERCA pump, maintain SOCE activity and T cell activation (Trebak & Kinet, 2019). Likewise, mitochondria form membrane contact sites to the ER membrane, called mitochondria-associated membranes (MAMs). Such contact sites consist of IP_3Rs releasing Ca^{2+} from the ER and MCUs promoting the Ca^{2+} uptake inside the mitochondria (Gil-Hernández et al., 2021; Trebak & Kinet, 2019). The increasing Ca^{2+} concentration inside the mitochondria triggers adenosine 5'-triphosphate (ATP) production (Brookes et al., 2004; Sparagna et al., 1995). Accordingly, MAMs directly connect TCR/CD3 stimulation and Ca^{2+} signaling with the cell's energy metabolism (Brookes et al., 2004).

Moreover, the ATP produced in the mitochondria can be released from the T cell itself and activate another group of channels at the PM, the purinergic ligand-gated cation (P2X) channels or the purinergic heterotrimeric guanine nucleotide-binding protein (G protein)-coupled receptors (GPCRs) P2Y (Blanchard et al., 1995; Yip et al., 2009). The P2X channels are known to be implicated in the amplification of Ca^{2+} signals (Woehrle et al., 2010; Yip et al., 2009). Two other groups of PM channels mediate Ca^{2+} signals after TCR/CD3 stimulation, the non-selective transient receptor potential (TRP) channels and the voltage-activated Ca^{2+} (CaV)

1 Introduction

channels (Trebak & Kinet, 2019). The accumulation of Ca^{2+} signals, due to the activity of all these Ca^{2+} release and entry channels, results in a global Ca^{2+} response (Fig. 1.2).

The increase in $[\text{Ca}^{2+}]_i$ activates calmodulin, which stimulates the phosphatase calcineurin to dephosphorylate nuclear factor of activated T cells (NFAT). NFAT translocates into the nucleus, mediates NFAT-dependent gene transcription, and thus initiates downstream effects for T cell differentiation and cytokine production (Macian, 2005).

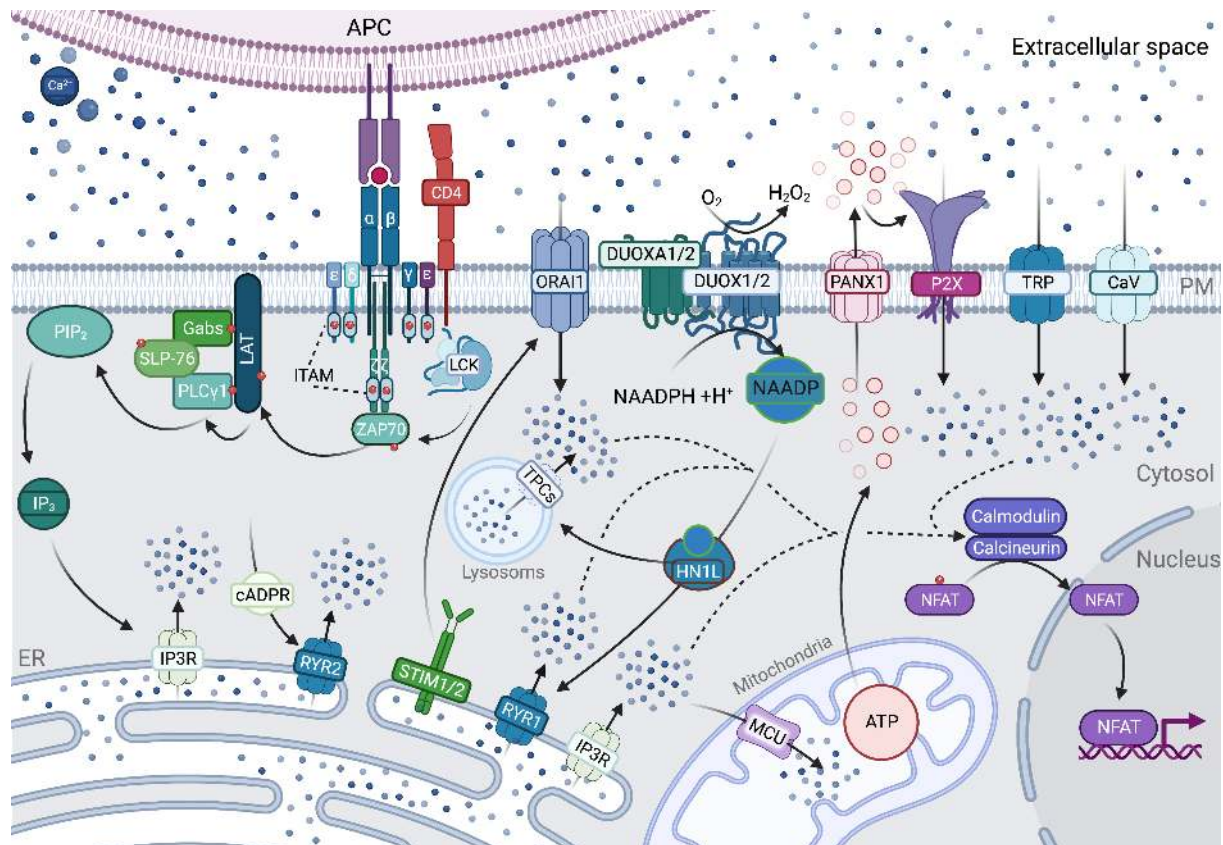


Figure 1.2: Ca^{2+} signaling in T cells. After TCR/CD3 stimulation second messengers like IP_3 via the cleavage of PIP_2 , cADPR or NAADP via the NAADPH oxidation by DUOX1/2 are produced. They stimulate Ca^{2+} channels located in the ER membrane. ER Ca^{2+} depletion is sensed by STIM1/2 , activating the store-operated Ca^{2+} channels ORAI1 . Ca^{2+} is transported inside the mitochondria to increase ATP synthesis. The ATP is transported outside the cell via the PANX1 hemichannel and activates the purinergic channels P2X1 , P2X4 and P2X7 . Together with the PM channels TRP and CaV a global Ca^{2+} response is generated. Increasing $[\text{Ca}^{2+}]_i$ activates calmodulin to stimulate calcineurin for the dephosphorylation of NFAT, which translocates into the nucleus to initiate NFAT-dependent transcription.

Global Ca^{2+} signaling describes the increase of whole $[\text{Ca}^{2+}]_i$ in the T cell cytosol and demonstrates the activation of a T cell for differentiation, secretion, energy production, and other downstream effects (Cahalan & Chandy, 2009; Vig & Kinet, 2009). Further, advanced Ca^{2+} imaging techniques uncovered a subdivision of this global Ca^{2+} response into spatiotemporally restricted signals that regulate T cell activation (Guse et al., 2021). These spatiotemporally restricted signals were named differently due to their Ca^{2+} concentration, their size, and the cell type in which they occur, like Ca^{2+} sparks, blips, quarks, and microdomains (Guse et al., 2021).

1 Introduction

The so-called Ca^{2+} microdomains are the initial signals in T cells occurring in hundreds of milliseconds after TCR/CD3 stimulation (Wolf et al., 2015). Ca^{2+} microdomains showed a diameter of approx. $0.4 \mu\text{m}$ and Ca^{2+} concentrations of approx. 200-400 nM (Diercks et al., 2018; Guse et al., 2021; Wolf et al., 2015).

T cells occur in different activation states, in (i) a quiescent state during the circulation in the blood, (ii) a pre-activated state upon the adhesion to, e.g. endothelial cells and (iii) a full activation state after TCR/CD3 stimulation (Guse et al., 2021). High resolution Ca^{2+} imaging methods were used to visualize the different activation states. Diercks and colleagues (2018) demonstrated a pre-clustering of STIM1/2 with ORAI1 and the formation of non-TCR/CD3 dependent Ca^{2+} microdomains. A similar SOCE implication in invading cancer cells on spontaneous Ca^{2+} glows was visualized using a genetically encoded Ca^{2+} indicator (GECI) called GCaMP6f (Lu et al., 2019). It has been shown, that non-TCR/CD3 dependent Ca^{2+} microdomains in T cells are infrequent and show a lower amplitude than those after TCR/CD3 stimulation (Diercks et al., 2018). Newest findings of our group suggest such infrequent Ca^{2+} microdomains to be adhesion-dependent in T cells (Mariella Weiß, Lola Hernandez and Björn Diercks, unpublished results). Recently, the involvement of the IP_3Rs in the formation of the non-TCR/CD3 dependent Ca^{2+} microdomains was uncovered (Gil et al., 2021), highlighting the complex network of Ca^{2+} signaling already during the (ii) state.

1.3 Purinergic signaling in immunity

The purinergic signaling cascade involves the release of nucleotides like ATP and uridine 5'-triphosphate (UTP), their activity sites and their degradation (Fig. 1.3).

ATP acts as an energy carrier that is mandatory for cell functions and metabolism (Bonora et al., 2012; Corriden & Insel, 2010). However, it also promotes apoptosis as well as cell death (Blanchard et al., 1995; Zamaraeva et al., 2005), and serves as a danger signal (Gazzerro et al., 2019; Linden et al., 2019). Released ATP influences cell functions in an autocrine or paracrine manner and the release itself is not only due to tissue damage or cell death, but a controlled mechanism in intact cells to alter physiological processes, like neutrophile chemotaxis or T cell activation (Bours et al., 2006; Junger, 2011; Trabanelli et al., 2012).

The intra- and extracellular concentrations of ATP differ a lot: the cytosolic ATP concentration is between 3 and 10 mM, but the assumed extracellular ATP concentration is about 10 nM, demonstrating a huge efflux gradient up to approx. 10^6 -fold (Schwiebert & Zsembery, 2003). Schwiebert and Zsembery (2003) claim that only 1 % or less of the intracellular ATP pool needs to be released to activate the ATP receptors. Thus, extracellular signaling can occur without compromising cellular metabolism or essential enzymatic reactions (Schwiebert & Zsembery, 2003).

1 Introduction

Extracellular ATP activates the purinergic receptors (P2) at the PM of cells (Burnstock & Boeynaems, 2014; Linden et al., 2019). P2 receptors are divided into the ligand-gated cation channels, P2X, and the purinergic heterotrimeric GPCRs P2Y (Schenk et al., 2011).

After TCR/CD3 stimulation $[Ca^{2+}]_i$ rises and is buffered by mitochondria to increase ATP synthesis (Schenk et al., 2008). For signal amplification, ATP is released from the stimulated T cell several minutes after stimulation via the ATP releasing pannexin-1 (PANX1) hemichannels and activates in an autocrine manner the P2X channels. Activation of the P2X channels promote immune cell activation and pro-inflammatory responses, like the initiation of the MAP kinase signaling and the production of pro-inflammatory cytokines like IL-2 (Frascoli et al., 2012; Junger, 2011; Schenk et al., 2008; Yip et al., 2009).

Several ectoenzymes are involved in the extracellular metabolism of nucleotides, like ecto-nucleoside triphosphate diphosphohydrolase 1 (eNTPDase1) CD39 (He et al., 2005; Horenstein et al., 2013; Linden et al., 2019). CD39 is expressed in many immune cells: about 90 % of B cells and monocytes, whereas only 6 % of T cells and NK cells express CD39. Moreover, the expression of CD39 is upregulated after T cell activation (Pulte et al., 2007).

CD39 hydrolyzes ATP to adenosine diphosphate (ADP) and further to adenosine monophosphate (AMP). P2X receptors can primarily be activated by ATP, whereas ADP, UTP, and ATP can activate P2Y receptors. P2Y receptors are important key regulators during the immune response and implicated for example in chemotaxis, phagocytosis, and granule release and especially in PLC β activation and cyclic AMP (cAMP) inhibition (Junger, 2011; Le Duc et al., 2017).

AMP is dephosphorylated by the ecto-5'-nucleotidase CD73 to adenosine and initializes an anti-inflammatory response via the activation of adenosine receptors P1 (Antonioli et al., 2013). P1 receptors are G-protein-coupled receptors, comparable with P2Y receptors, but use adenosine as a substrate (Borea et al., 2018). Increasing adenosine levels stimulate the P1 receptors, like A1, A2_A, A2_B, and A3. The receptors differ in their adenosine affinities (between 1-1000 nM) and have a wide range of effects on immune cells, for example, the inhibition of reactive oxygen species, immunosuppression, or the inhibition of pro-inflammatory cytokines, making P1 receptors an attractive therapeutic target (Borea et al., 2018; Flögel et al., 2012; Müller & Jacobson, 2011).

1 Introduction

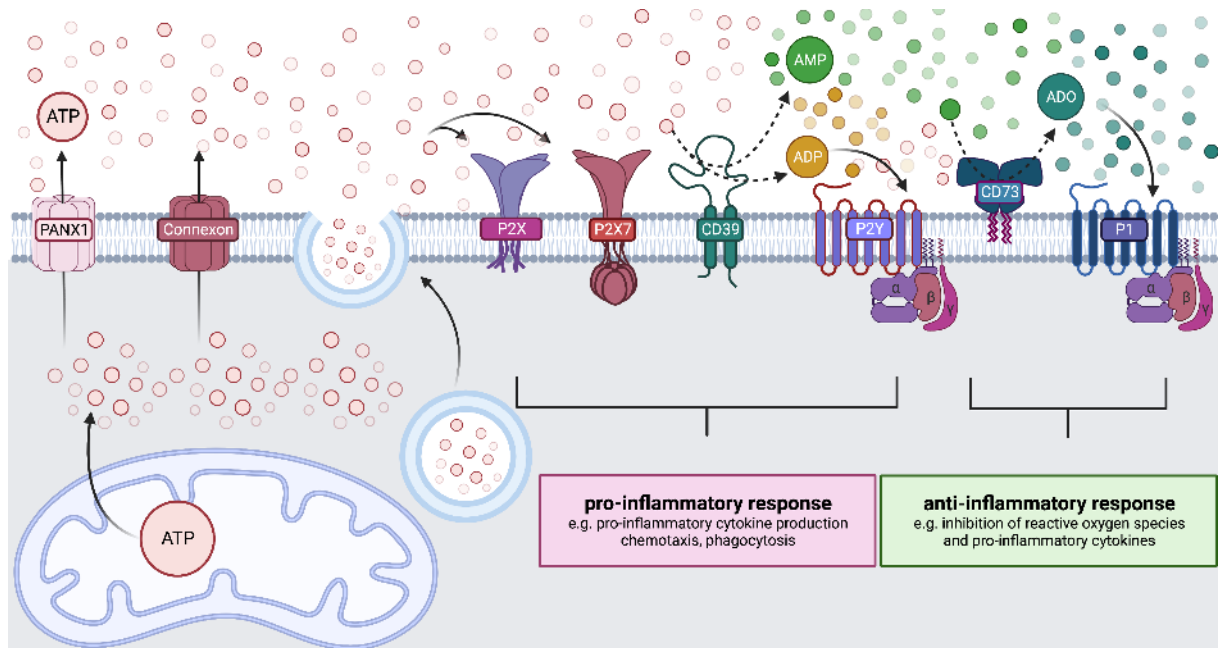


Figure 1.3: Purinergic signaling cascade. ATP is released via PANX1 and other ATP releasing channels or via exocytosis. The released ATP activates the P2X channels. The ectoenzyme CD39 hydrolyzes ATP to ADP and further to AMP. ATP and ADP stimulate the P2Y channels. P2X and P2Y activation initiates pro-inflammatory responses. AMP, moreover, is hydrolyzed to adenosine by the most prominent ecto-5'-nucleotidase CD73. Anti-inflammatory responses are induced by the activation of P1 receptors by the adenosine.

1.3.1 ATP release

Since ATP molecules cannot simply diffuse across the PM and there is a huge gradient between intra- and extracellular ATP levels, there are several mechanisms of cellular ATP release (Fig. 1.3) (Schwiebert & Zsemberly, 2003; Taruno, 2018). ATP can be released uncontrolled from damaged cells (Cook & McCleskey, 2002) or controlled via exocytosis or ATP releasing channels (Pankratov et al., 2007; Taruno, 2018; Y. Wang et al., 2013).

In T cells and microglia, a vesicular nucleotide transporter (VNUT) was identified to be responsible for ATP storage and vesicular exocytosis (Imura et al., 2013; Tokunaga et al., 2010). Tokunaga and colleagues (2010) showed that TCR/CD3-dependent ATP release was not only due to ATP releasing channels but also due to vesicular exocytosis by VNUT. Moreover, the vesicular ATP release in microglia and T cells depends on increasing $[Ca^{2+}]_i$.

Five ATP releasing channels are recently confirmed: the connexin (CNX) hemichannels, PANX1, Ca^{2+} homeostasis modulator 1 (CALHM1), volume-regulated anion channels (VRACs), and the maxi-anion channels (MACs) (Taruno, 2018).

VRACs and MACs can be activated by osmotic stress and cell swelling, and hence, regulate cell volume. Furthermore, MACs are sensitive to gadolinium (Gd^{3+}) (M. R. Islam et al., 2012; Jentsch, 2016). In macrophages and microglia, it was shown that the second messenger sphingosine-1-phosphate (S1P), produced after the activation of toll-like receptors (TLR2 and TLR4), stimulates VRAC-dependent ATP release, activation of P2X channels, and cell migration (Burow et al., 2015; Zahiri et al., 2021). Details of the physiological role of VRAC-

1 Introduction

and MAC-dependent ATP release still remain unclear as their molecular identity is not confirmed until now (Burow et al., 2015; Taruno, 2018).

CNX hemichannels, CALHM1, and PANX1 show structural and functional similarities. A single subunit of these channels consists of four transmembrane helices. CNX hemichannels and CALHM1 are formed by hexamers, whereas PANX1 is formed by heptamers (Ma et al., 2016; Oshima, 2014; Ruan et al., 2020; Siebert et al., 2013). CNX form gap junctions for direct cell-to-cell communication between neighboring cells, while PANX1 preferably acts as a hemichannel to release small molecules from the cytoplasm (Vultaggio-Poma et al., 2020). Altered extracellular Ca^{2+} concentrations activated CALHM1 and CNX hemichannels, and all three channels, CALHM1, CNX, and PANX1 hemichannels, were triggered by membrane depolarization (Siebert et al., 2013).

For the opening of PANX1, more mechanisms were postulated. PANX1 is activated not only by membrane depolarization but also by caspase cleavage, mechanical stress, increasing $[Ca^{2+}]_i$ levels, or increasing extracellular potassium (K^+) levels, and a few more mechanisms are reviewed by Taylor and colleagues in detail (Dosch et al., 2018; Taylor et al., 2015).

1.3.2 P2X channels

In mammals, seven subtypes of the P2X family were described, P2X1-P2X7. Evolutionary relationships within the seven subtypes were discovered: e.g. it is likely that *P2rx4* and *P2rx7* shared the same ancestral gene and emerged after gene duplication (Hou & Cao, 2016). Moreover, *P2rx4* and *P2rx7* are located next to each other on the same chromosome and functional interactions were proposed while a heteromerization of the two channels was not confirmed (Boumechache et al., 2009; Hou & Cao, 2016; Kopp et al., 2019).

The P2X receptors form trimeric channels and each dolphin-like subunit consists of a C- and N-terminus located intracellularly, two transmembrane domains (TM1 and TM2) and a large extracellular domain (ectodomain) including the ATP binding site (Browne, 2012; Habermacher et al., 2016). The dolphin-like shape of the P2X subunit is comparable for all subtypes, whereas the P2X7 channel exhibit a unique cytoplasmic ballast (Fig. 1.4). This part contains three β strands forming an antiparallel β sheet tailed by eight α helices, separated by loops forming a helical bundle (McCarthy et al., 2019). ATP binding to the trimeric P2X channels leads to an opening of the channels permeable for small mono- and bivalent cations, like Ca^{2+} , Na^+ , and K^+ .

After persistent ATP binding, the P2X channels are desensitized and, to this end, get inactive again. Different desensitization kinetics are mentioned for the P2X subtypes. While P2X1 and P2X3 channels desensitize fast, P2X2, P2X4, and P2X5 show slower desensitization, and for

1 Introduction

P2X7, no desensitization is described (Habermacher et al., 2016; McCarthy et al., 2019; North, 2002).

Under physiological conditions, ATP is found in complexes with bivalent cations, like magnesium (Mg^{2+}) (Di Virgilio et al., 2001). $MgATP^{2-}$ complexes show different actions on the P2X subtypes. P2X2, P2X4, and P2X7 receptors are assumed to need free ATP for their activation, whereas P2X1 and P2X3 receptors are also sensitive to $MgATP^{2-}$ (Li et al., 2013; Markwardt, 2021). Mg^{2+} ions themselves inhibit P2X channel activation (McCarthy et al., 2019), for P2X2 by binding to the ATP inside the agonist binding pocket and for P2X3, most likely by binding to the central chamber at the threefold axis (Li et al., 2013). Such results indicate a modulating role of bivalent cations on the activation of P2X channels.

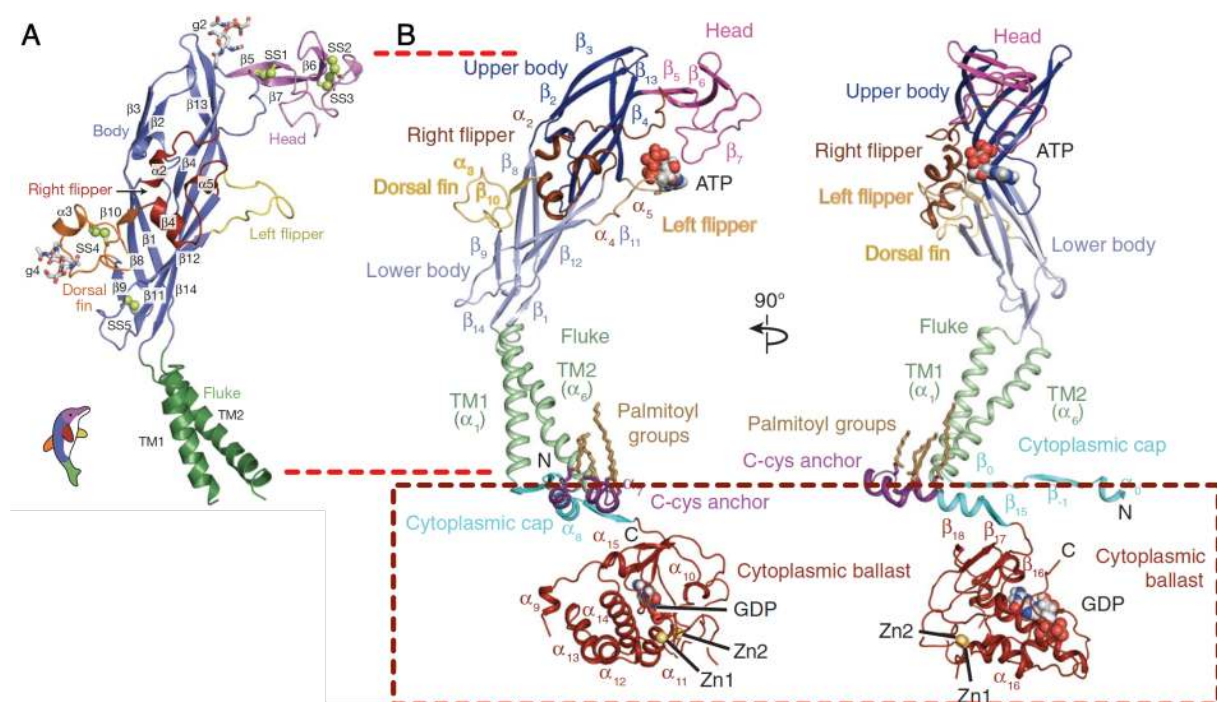


Figure 1.4: P2X monomer structure. A) P2X4 monomer has a dolphin like structure. α helices (TM1–2 and α 2–5), β strands (β 1–14), disulphide bonds (SS1–5), and attached glycans (g2 and g4) are indicated. The structure of the P2X4 subunit is comparable for all P2X channel subtypes. B) The P2X7 monomer exhibits a unique cytoplasmic ballast (as indicated in the dark red square). It contains three β strands forming an antiparallel β sheet that is tailed by eight α helices, separated by loops forming a helical bundle. Modified from A) Kawate et al., 2009 and B) McCarthy et al., 2019.

Furthermore, the subtypes show not only different desensitization properties and sensitivities to bivalent cations but also get activated by different concentrations of ATP. P2X1, P2X3, and P2X5 are sensitive to ATP in the nanomolar range, whereas P2X2 and P2X4 get activated in the low micromolar range. P2X7 can be activated by ATP concentrations higher than $100 \mu M$ (Kaczmarek-Hájek et al., 2012). ATP concentrations in the micromolar range trigger P2X7 functioning as an ion channel, whereas high concentrations in the millimolar range trigger P2X7-mediated cell death (Junger, 2011).

1 Introduction

P2X7 is the most studied P2X channel because it regulates many inflammatory responses and its ability to form a non-selective macropore (Grassi, 2020; Linden et al., 2019). Different mechanisms of pore formation are discussed. One described mechanism is the so-called “pore dilation” hypothesis. It proposes that the pore formation is a function of the P2X7 channel itself and the ability of the channel to increase its permeability on its own. Another described mechanism for the pore formation is the interaction of the P2X7 channel with other channel proteins to generate a macropore, like the PANX1 hemichannel (Kopp et al., 2019).

Furthermore, a P2X7-unique ATP-independent activation pathway is postulated in murine cells. In the presence of NAD⁺, the ecto-ADP-ribosyltransferase ARTC2.2 catalyzes the ADP-ribosylation of the P2X7 receptor resulting in channel opening and induction of cell death (Er-Lukowiak et al., 2020; Rivas-Yáñez et al., 2020).

P2X1, P2X4, and P2X7 channels are described to be implicated in Ca²⁺ signaling in T cells and to influence the activation of the NFAT and cytokine production (Woehrle et al., 2010; Yip et al., 2009).

1.3.3 P2Y receptors

P2Y receptors belong to the rhodopsin-like GPCR family, the largest group of GPCRs in vertebrates and eight subtypes (P2Y1, P2Y2, P2Y4, P2Y6, and P2Y11-14) are described (Le Duc et al., 2017). The GPCRs bind G proteins at the inner surface of the cell that form heterotrimeric complexes consisting of G α subunit that is closely associated with G $\beta\gamma$ subunits. G proteins are divided into four subtypes G_s, G_{i/o}, G_{q/11}, and G_{12/13} (Neves et al., 2002). Activation of the P2Y receptor leads to a dissociation of the G protein from the receptor and dissociation of the G protein subunits from each other to activate or deactivate other effector proteins (Erb & Weisman, 2012). Due to their G protein coupling, P2Y receptors are also divided into two subfamilies. The G_{q/11} coupled subfamily includes P2Y1, P2Y2, P2Y4, and P2Y11 receptors stimulating PLC, whereas the G_{i/q} coupled subfamily consists of the P2Y12-14 subtypes inhibiting adenylate cyclase (AC) (Jacobson et al., 2012; Von Kügelgen & Hoffmann, 2016).

P2Y1, P2Y11, P2Y12, and P2Y13 are activated by adenine nucleotides, whereas P2Y4 and P2Y6 are activated via pyrimidine nucleotides. P2Y2 is sensitive to ATP and UTP and P2Y14 to uridine diphosphate (UDP)-sugars (Chambers et al., 2000; Kolen & Slegers, 2006; Le Duc et al., 2017). Previous studies show the influence of the P2Y receptors on immune responses, like modulation of Ca²⁺ fluxes, chemotaxis, phagocytosis, or cell migration (Le Duc et al., 2017). Accordingly, one example is the P2Y1 receptor in macrophages. This receptor is proposed to be implicated in neutrophil migration in inflammatory tissues by increasing the secretion of the chemokine CXCL2 (Zhang et al., 2021).

1 Introduction

Another pro-inflammatory pathway is influenced by P2Y₁₁. The receptor is assumed to be sensitive to nicotinamide adenine dinucleotide (NAD⁺) and NAADP. Once P2Y₁₁ is activated, it stimulates PLC to increase the intracellular production of IP₃ and, consequently, [Ca²⁺]_i. Additionally, P2Y₁₁ activity is coupled to activation of the AC increasing cAMP concentrations (Moreschi et al., 2008).

Furthermore, P2Y receptors like P2Y₁, P2Y₂, or P2Y₁₁ are co-expressed with P2X receptors, like P2X₁ or P2X₇, to potentiate and fine-tune their activity (Dreisig et al., 2018; Vial et al., 2004), indicating a regulatory function of P2Y receptors on P2X receptor activity.

1.3.4 Purinergic Ca²⁺ signaling in T cells

As previously described in 1.2.1, activation of T cells leads to increasing Ca²⁺ concentrations inside the cytosol. Rapid Ca²⁺ buffering occurs through the activity of MCUs, raising Ca²⁺ levels inside the mitochondria. It is postulated that the Ca²⁺ uptake into the mitochondria elevates ATP production and that TCR/CD3 stimulation triggers the mitochondria to accumulate at the immune synapse (Ledderose et al., 2014).

ATP is mentioned to be released from the T cell after TCR/CD3 stimulation via the PANX1 that translocates to the immune synapse within 5 min after TCR/CD3 stimulation (Woehrle et al., 2010). Another study suggests, that TCR/CD3-dependent ATP release is not only due to PANX1 channel activity, but also due to the channel activity of gap junction hemichannels, MACs and interestingly also due to exocytosis (Tokunaga et al., 2010).

Extracellular ATP stimulates the P2X channels (Fig. 1.5). The P2X₁, P2X₄, and P2X₇ channels are assumed to be implicated in Ca²⁺ influx after TCR/CD3 stimulation (Woehrle et al., 2010; Yip et al., 2009). P2X₁ and P2X₄ moreover co-localize with STIM1 and ORA1 in activated T cells (Woehrle et al., 2010), suggesting an amplifying effect of P2X channels on Ca²⁺ signaling. The purinergic activation of T cells leads to downstream effects, like NFAT activation and cytokine production (Manohar et al., 2012; Yip et al., 2009).

Stimulation of chemokine receptors promotes the clustering of P2X₄ channels and mitochondria at the front of cells for local Ca²⁺ and ATP raises to induce T cell migration (Ledderose et al., 2018). Furthermore, paracrine ATP is sensed by P2X₄ and P2X₇ in unstimulated T cells resulting in Ca²⁺ waves and a reduced T cell motility. This might be a specific mechanism of T cells for advanced DC scanning (C. M. Wang et al., 2014).

1 Introduction

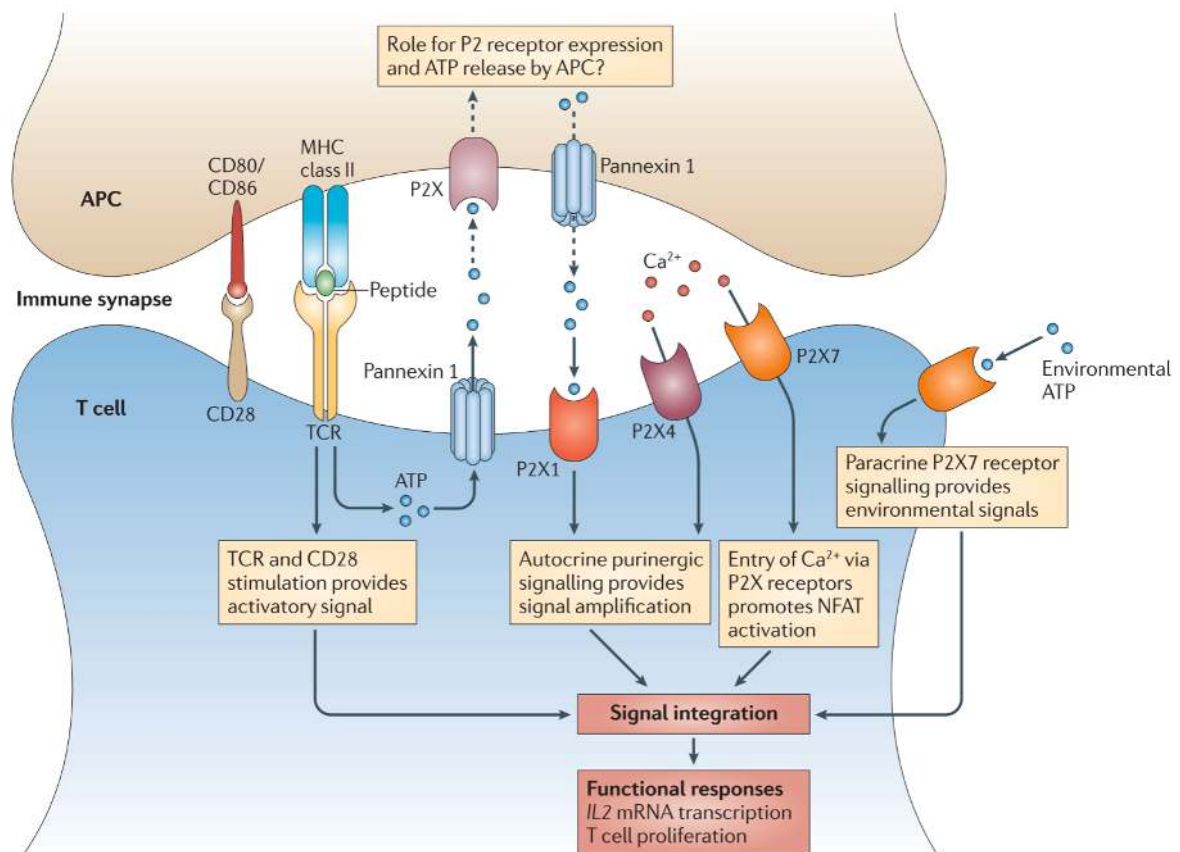


Figure 1.5: Purinergic signaling after TCR/CD3 stimulation. The TCR/CD3 stimulation of a T cell triggers the production of ATP, which is released from the cell via PANX1. Autocrine and paracrine released ATP activates P2X1, P2X4 and P2X7. Ca²⁺ signals were amplified by the activity of P2X4 and P2X7. From Junger, 2011.

1.4 Ca²⁺ imaging: Ca²⁺ indicators

Ca²⁺ signals promote the conversion of external stimuli into internal responses in cells, like the activation of T cells (Guse et al., 2021; Trebak & Kinet, 2019).

To study [Ca²⁺]_i, intracellular Ca²⁺ indicators are needed. The first chemical Ca²⁺ indicators, which were membrane permeable, were introduced in 1981 by R. Tsien. He masked the indicators by acetoxymethyl (AM) groups orchestrating the indicators through the PM into the cytosol, where the AM groups were cleaved by unspecific esterases making the indicators polar and unable to diffuse through the PM and hence accumulate in the cytosol (Meldolesi, 2004; Tsien, 1981). In 1985, the nowadays very commonly used chemical indicators Fura-2 and Indo-1 were developed. Compared to older indicators, the advantages of these indicators are that they exhibited lower Ca²⁺ affinities, higher fluorescence intensity and ratiometric properties. The binding of Ca²⁺ to Fura-2 shifts the excitation from the Ca²⁺ free form at 380 nm to 340 nm, whereas the emission stays the same (Fig. 1.6). The shift in the excitation can be used for calculating the ratio.

1 Introduction

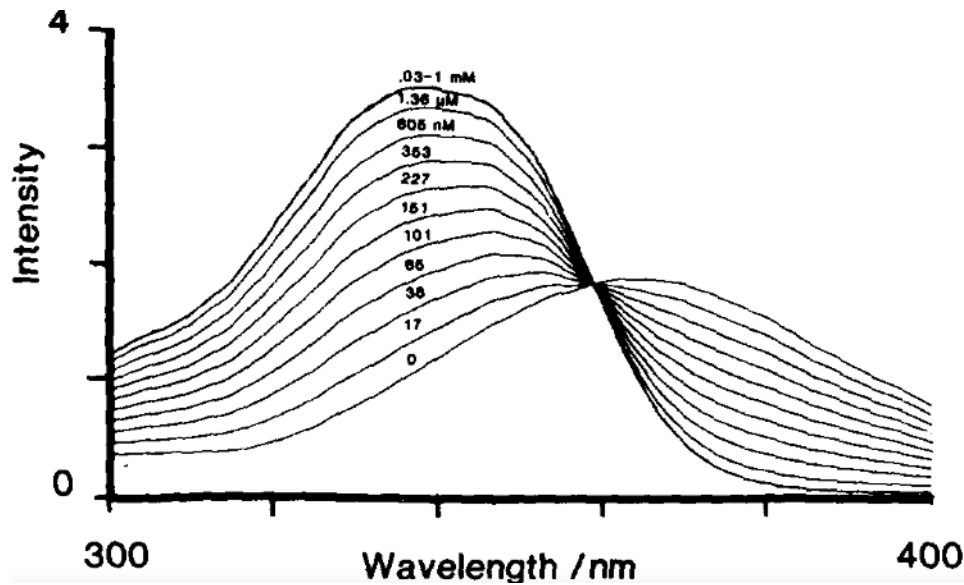


Figure 1.6: Excitation spectra for 1 μ M Fura-2. Upon Ca^{2+} binding the excitation is shifted from 380 nm to 340 nm. This shift enables the use of the indicator for ratiometric calculations. Ratiometric Ca^{2+} measurements have many advantages compared to single-wavelength measurements, e.g. movements of a cell or its' plasticity influencing the fluorescence intensity will be negligible due to the calculation of the ratio. From Grynkiewicz et al., 1985.

In contrast to Fura-2, Indo-1 shows dual emission spectra upon Ca^{2+} binding at the same excitation wavelength (Grynkiewicz et al., 1985). Today a long list of chemical Ca^{2+} indicators is available including single-, dual-excitation and dual-emission-wavelength fluorescent dyes, ranging from a maximum effective dissociation constant K_d of 110 nM (quin2) to a minimum K_d of 90 000 nM (Fluo-5N) (Meldolesi, 2004).

Another group of Ca^{2+} indicators are the GECIs. They are based on the Green Fluorescence Protein (GFP) and other fluorescence protein family members. A Ca^{2+} binding moiety is fused to the fluorescence protein to create a chimeric construct sensing Ca^{2+} alteration that can be expressed in different cell types or fused to single channels of interest, like the SOCE channel Orai1 (Demuro & Parker, 2006; Dynes et al., 2016; Mank & Griesbeck, 2008).

Comparison of chemical and genetically encoded Ca^{2+} indicators showed an advantage of chemical Ca^{2+} dyes. They combine high Ca^{2+} sensitivities with fast binding kinetics (Mank & Griesbeck, 2008), making chemical Ca^{2+} dyes good tools for measuring rapid Ca^{2+} alterations in cells, whereas GECIs are more suitable for single-channel recordings.

Analysis of local and spatiotemporally restricted signals, like the Ca^{2+} microdomains, using the common techniques was challenging for a long time due to their rapid and dynamic formation. A ratiometric technique was developed based on the combination of two existing dyes, Fluo-4 and FuraRed. Loading of T cells with the two dyes show similar Ca^{2+} binding and photobleaching properties and a similar subcellular distribution. This technique improves spatial and temporal resolution (approx. 0.368 μ m and 40 fps) for subcellular Ca^{2+} imaging (C. M. Wang et al., 2014; Wolf et al., 2015).

1 Introduction

1.4.1 Ca²⁺ imaging: image restoration

The output of high-resolution life cell imaging measurements depends not only on the quality of the fluorescent indicators but also on the acquisition setups, like microscope type, objective, exposure time and the camera used. All these parameters influence the fluorescence of the dye or fluorescent protein due to photobleaching and phototoxicity. To prevent damages by phototoxicity or photobleaching, the light exposure, imaging speed or spatial resolution are adjustable key factors (Ettinger & Wittmann, 2014; Weigert et al., 2018). Especially the nature of Ca²⁺ microdomains being highly dynamic, fast fugitive signals makes them a challenging task for imaging approaches. Imaging speed and spatial resolution need to be as high as possible, resulting in the usage of a low exposure time and, to this end, in low signal-to-noise ratios (SNRs) and image degradation.

Noise is one cause of image degradation (Wallace et al., 2001). The source of noise in microscopy approaches is known. Noise can occur due to the signal itself (“photon shot noise”) or from the digital imaging system (Wallace et al., 2001). Since the source of noise and the mechanism through it are understood, it is possible to calculate a statistical distribution of noise; one characterizes the signal-dependent noise (“Poisson distribution”) and another one the imaging system-dependent noise (“Gaussian distribution”) (Wallace et al., 2001).

Moreover, other factors than noise cause image degradation. One of these factors is blurring (Young, 1989). The three-dimensional shape of imaged cells is responsible for emitting light from different planes. A microscope detector senses light from the cell section, which the microscope objective focuses on. Additionally, it senses emitted light from the out-of-focus cell sections. Out-of-focus light is one reason for image degradation and define the blurring of an image. It can be characterized by the so-called “point spread function” (PSF, Fig. 1.7) (Sarder & Nehorai, 2006).

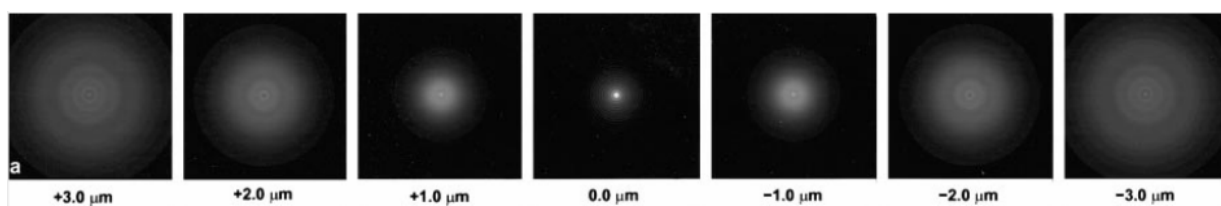


Figure 1.7: Point-spread-function. Theoretically predicted PSF for a 100X, 1.35 NA Olympus UplanApo objective. Distances above and below focus are shown from +3.0 μm to -3.0 μm . Modified from McNally et al. 1999.

The PSF is a spatiotemporally independent parameter depending on the microscope setup (Anastasopoulou et al., 2019). On the one hand, a point of light source from one plane spreads light to another plane of an object (McNally et al., 1999). On the other hand, the light intensity of one plane is spread due to diffraction and variations inside the system (Sage et al., 2017). The sum of these “point-spread-functions” of each plane composes an image and can be used

1 Introduction

to deconvolve an image. The PSF is obtained experimentally or mathematically (Markham, 1999).

Computational restoration techniques utilize the knowledge about degradation causes like noise distribution or blurring and the PSF to reconstruct an image with the closest possible conformance with the original object (Arigovindan et al., 2013; Sarder & Nehorai, 2006; Schaefer et al., 2001; Weigert et al., 2018).

There are many different conventional deconvolution techniques, most of which can be broadly categorized into “deblurring” and “image restoration” algorithms. Deblurring algorithms operate in a 2-D fashion plane-by-plane, whereas image restoration algorithms are 3-D and work simultaneously on every pixel in an image stack (Wallace et al., 2001). Deblurring algorithm includes algorithms like the “no-neighbors methods” or “neighboring methods”. In contrast, image restoration algorithms are methods like “linear methods” (e.g., inverse filtering or Wiener filtering), nonlinear iterative methods (e.g., Janson Van Cittert or Tikhonov-Miller), statistical methods, and blind deconvolution (BD) (Sage et al., 2017; Sarder & Nehorai, 2006; Wallace et al., 2001). Additionally, for iterative methods, mathematical assumptions of the original object can also be used to improve the deconvolved result: e.g. when we assume that an object is relatively smooth, noisy results with rough edges can be eliminated (Wallace et al., 2001). This technique is called regularization, narrowing possible estimations produced by an iterative algorithm concerning to some assumptions about the original object (Poggio et al., 1988; Wallace et al., 2001).

Many deconvolution algorithms perform poorly on measurable subcellular details in the presence of noise. Arigovindan and co-workers (2013) introduced a unique logarithmic (entropy-like) regularization term that emphasizes the stabilization of the noise, known as noise regularization. The regularization is adapted to the spatial features of the fluorescence signal to increase spatial smoothness and image resolution for low SNR images (Arigovindan et al., 2013).

1.5 Study objective

The activation of T cells initiates the adaptive immune response. Following TCR/CD3 stimulation, Ca^{2+} signals translate the external stimulus into intracellular responses. Uncovering the dynamic mechanism of Ca^{2+} signaling is essential for comprehending T cell activation and downstream events.

Analysis of Ca^{2+} microdomains in different mouse models identified several key players of Ca^{2+} release and entry involved in the formation of these signals: Milliseconds after TCR/CD3 stimulation, the second messenger NAADP was shown to activate RYR1 via HN1L/JPT2, resulting in a Ca^{2+} release from the ER. Furthermore, it was demonstrated that ER depletion

1 Introduction

is sensed by STIM1/2 stimulating the SOCE channel ORAI1. The ATP-gated channels P2X4 and P2X7 were demonstrated to foster Ca^{2+} signals during later steps of T cell activation; however, their impact on the formation of Ca^{2+} microdomains was unknown. While ATP acts as an extracellular signaling molecule and Ca^{2+} as an intracellular signaling ion, the P2X channels directly connect extracellular and intracellular signaling cascades.

The main objective of this thesis was to uncover the role of P2X4 and P2X7 on the formation of Ca^{2+} microdomains. Therefore, Ca^{2+} live-cell-imaging was performed using *P2rx4^{-/-}* and *P2rx7^{-/-}* CD4⁺ T cells, antagonists or inhibiting nanobodies. Additionally, apyrase, an ATP degrading enzyme, and an antagonist for the ATP releasing channel PANX1 were used to analyze the role of extracellular ATP on the formation of Ca^{2+} microdomains. Downstream events, like the expression of CD69 or Nur77, were analyzed to elucidate and differentiate the channel functions of P2X4 and P2X7 and their impact on the immune response.

Although, the Ca^{2+} imaging approach enabled the discovery of short-lived Ca^{2+} microdomains, the approach is technically limited by its spatial and temporal resolution. Computational restoration of low SNR images can further increase their quality afterwards. Thus, advanced computational solutions for image sequences were tested to improve temporal resolution and visualization of Ca^{2+} microdomains.

2. Publications

2.1. Publication I

Published in October 2021 in Int. J. Mol. Sci., International Journal of Molecular Science, 22(21), 11792, DOI: 10.3390/ijms222111792, <https://www.mdpi.com/1422-0067/22/21/11792>

Time-Dependent Image Restoration of Low-SNR Live-Cell Ca²⁺ Fluorescence Microscopy Data

Lena-Marie Woelk 1*, Sukanya A. Kannabiran 2, **Valerie J. Brock** 2, Christine E. Gee 3, Christian Lohr 4, Andreas H. Guse 2, Björn-Philipp Diercks 2 and René Werner 1

1 Department of Computational Neuroscience, University Medical Center Hamburg-Eppendorf, 20246 Hamburg, Germany

2 Department of Biochemistry and Molecular Cell Biology, University Medical Center Hamburg-Eppendorf, 20246 Hamburg, Germany

3 Institute of Synaptic Physiology, University Medical Center Hamburg-Eppendorf, 20246 Hamburg, Germany


4 Division of Neurophysiology, Institute of Zoology, University of Hamburg, 20146 Hamburg, Germany

* Correspondence: le.woelk@uke.de



Communication

Time-Dependent Image Restoration of Low-SNR Live-Cell Ca²⁺ Fluorescence Microscopy Data

Lena-Marie Woelk ^{1,*}, Sukanya A. Kannabiran ², Valerie Brock ², Christine E. Gee ³, Christian Lohr ⁴,
Andreas H. Guse ², Björn-Philipp Diercks ² and René Werner ¹ 

¹ Department of Computational Neuroscience, University Medical Center Hamburg-Eppendorf, 20246 Hamburg, Germany; r.werner@uke.de

² Department of Biochemistry and Molecular Cell Biology, University Medical Center Hamburg-Eppendorf, 20246 Hamburg, Germany; s.arcotkannabiran@uke.de (S.A.K.); v.brock@uke.de (V.B.); guse@uke.de (A.H.G.); b.diercks@uke.de (B.-P.D.)

³ Institute of Synaptic Physiology, University Medical Center Hamburg-Eppendorf, 20246 Hamburg, Germany; christine.gee@zmnh.uni-hamburg.de

⁴ Division of Neurophysiology, Institute of Zoology, University of Hamburg, 20146 Hamburg, Germany; christian.lohr@uni-hamburg.de

* Correspondence: le.woelk@uke.de



Citation: Woelk, L.-M.; Kannabiran, S.A.; Brock, V.; Gee, C.E.; Lohr, C.; Guse, A.H.; Diercks, B.-P.; Werner, R. Time-Dependent Deconvolution of Low-SNR Live-Cell Ca²⁺ Fluorescence Microscopy Data. *Int. J. Mol. Sci.* **2021**, *1*, 0. <https://doi.org/>

Academic Editor: Demetrios A. Arvanitis

Received: 30 September 2021

Accepted: 26 October 2021

Published:

Publisher's Note: MDPI stays neutral with regard to jurisdictional claims in published maps and institutional affiliations.



Copyright: © 2021 by the authors. Licensee MDPI, Basel, Switzerland. This article is an open access article distributed under the terms and conditions of the Creative Commons Attribution (CC BY) license (<https://creativecommons.org/licenses/by/4.0/>).

Abstract: Live-cell Ca²⁺ fluorescence microscopy is a cornerstone of cellular signaling analysis and imaging. The demand for high spatial and temporal imaging resolution is, however, intrinsically linked to a low signal-to-noise ratio (SNR) of the acquired spatio-temporal image data, which impedes on the subsequent image analysis. Advanced deconvolution and image restoration algorithms can partly mitigate the corresponding problems but are usually defined only for static images. Frame-by-frame application to spatio-temporal image data neglects inter-frame contextual relationships and temporal consistency of the imaged biological processes. Here, we propose a variational approach to time-dependent image restoration built on entropy-based regularization specifically suited to process low- and lowest-SNR fluorescence microscopy data. The advantage of the presented approach is demonstrated by means of four datasets: synthetic data for in-depth evaluation of the algorithm behavior; two datasets acquired for analysis of initial Ca²⁺ microdomains in T-cells; finally, to illustrate the transferability of the methodical concept to different applications, one dataset depicting spontaneous Ca²⁺ signaling in jRCaMP7b-expressing astrocytes. To foster re-use and reproducibility, the source code is made publicly available.

Keywords: Ca²⁺ imaging; fluorescence microscopy; live-cell imaging; low signal-to-noise ratio; deconvolution; image restoration

1. Introduction

T-cell activation represents the on-switch of the adaptive immune system [1]. Within tens of milliseconds after activation, highly dynamic, spatio-temporally restricted Ca²⁺ signals, termed Ca²⁺ microdomains, start occurring [1,2], but the molecular machinery underlying this process still remains elusive. To better understand the principles of the formation and the temporal propagation of these signals as well as the contributions and roles of different components, high-resolution live-cell fluorescence microscopy is required, ideally implemented with both the spatial and the temporal resolution as high as possible. However, high-resolution Ca²⁺ imaging has severe limitations: Low photon doses due to phototoxicity and photobleaching as well as the fugitive nature of Ca²⁺ signals in combination with out-of-focus light lead to an intrinsically low signal-to-noise ratio (SNR) [3]. This, in turn, significantly impedes the identification and detailed analysis of Ca²⁺ microdomains and their spatio-temporal architecture.

The analysis of initial Ca²⁺ microdomains in T-cells and the corresponding need to reliably identify related signaling events in live-cell imaging data with poor SNR forms

the basis and motivation of the present work, but it is only one example application; a related prominent Ca^{2+} imaging application is, e.g., capturing Ca^{2+} waves with a high imaging speed (often $>80\text{ Hz}$) and corresponding short exposure times [4]. However, the general challenge to extract meaningful information from low-SNR image time series data is applicable to many applications in the context of spatio-temporal fluorescence microscopy. Techniques to increase the quality of captured images are typically referred to as image restoration or deconvolution.

In recent years, microscopy image restoration has been increasingly tackled using deep learning methods [5,6], but a systematic problem with these approaches remains the risk of hallucinations, i.e., the generation of structures not present in the acquired imaging data [7]. In addition, extensive amounts of suitable training data are usually required, limiting their applicability.

Conventional approaches, in contrast, work purely on the image data to be processed. They include classic, straight-forward methods, such as nearest neighbor deconvolution or naive inverse filtering, which are computationally inexpensive but have drawbacks such as poor noise reduction and the introduction of ringing artifacts. More sophisticated methods are often formulated as iterative algorithms and variational models, with a variety of data fidelity and regularization terms being proposed in literature. The most common approaches are (regularized) inverse filtering, including, e.g., Wiener filtering [8,9] and (regularized) Lucy-Richardson (LR) deconvolution [10,11]. For an overview, please refer to, e.g., [12,13].

Most functional formulations are, however, rather general, and the resulting algorithms perform poorly in low-SNR scenarios [14]. In 2013, Arigovindan et al. introduced a functional formulation that was tailored to the specific characteristics of fluorescence microscopy [14]. In particular, they proposed an entropy-like formalism in combination with a second order derivatives-based regularization functional that suppresses noise but still preserves object details. A central rationale behind their formulation was, e.g., that, in contrast to general imaging data, in fluorescence microscopy data, "high intensity points are more sparsely distributed and are co-localized with high-magnitude derivative points" [14]. The presented results were impressive especially for low-SNR conditions. However, although motivated by demands of spatio-temporal imaging, the proposed formulation addressed only frame-by-frame deconvolution, i.e., the resulting algorithm was to be applied independently to each frame. While this is common to most image restoration methods (both deep learning and conventional approaches), recent work illustrated the benefits of taking the spatio-temporal nature of the acquired data into account [15,16].

In the present work, we extend the principle of entropy-like deconvolution proposed by [14] and suggest a novel variational approach tailored to image restoration of spatio-temporal fluorescence microscopy. The proposed approach utilizes the temporal information available in the imaging data to further improve image quality and SNR at low exposure times, thus enabling imaging with a higher temporal resolution. To foster re-using the developed methods, the source code is freely available at <https://github.com/IPMI-ICNS-UKE/TDEntropyDeconvolution>, accessed on 26 October 2021. The repository also covers an implementation of the approach described in [14] to be applied to static microscopy data (no publicly available source code provided with the original publication). The corresponding practical notes are given in Appendix A.2; further documentation and example scripts are provided as a part of the repository.

The advantage of the proposed approach is illustrated for four datasets. The first three datasets are related to the analysis of Ca^{2+} microdomains in T-cells: (1) a synthetic dataset with simulated Ca^{2+} signals and noise patterns to systematically evaluate the algorithm performance; two super-resolution spinning disc microscope datasets, one acquired with a genetically encoded Ca^{2+} indicator tagged to a lysosomal channel (2) and the other one to study the free cytosolic Ca^{2+} concentration ($[\text{Ca}^{2+}]_i$) (3) in Jurkat T-cells. The fourth dataset illustrates the use in different application contexts. Here, confocal data of spontaneous Ca^{2+} signals in branches of an astrocyte in a mouse brain slice.

2. Results

2.1. Synthetic Data

A comparison of the effects of the different deconvolution approaches for an example of the generated synthetic data with different noise levels is given in Figure 1. The simulated ground truth data are shown in Figure 1a.

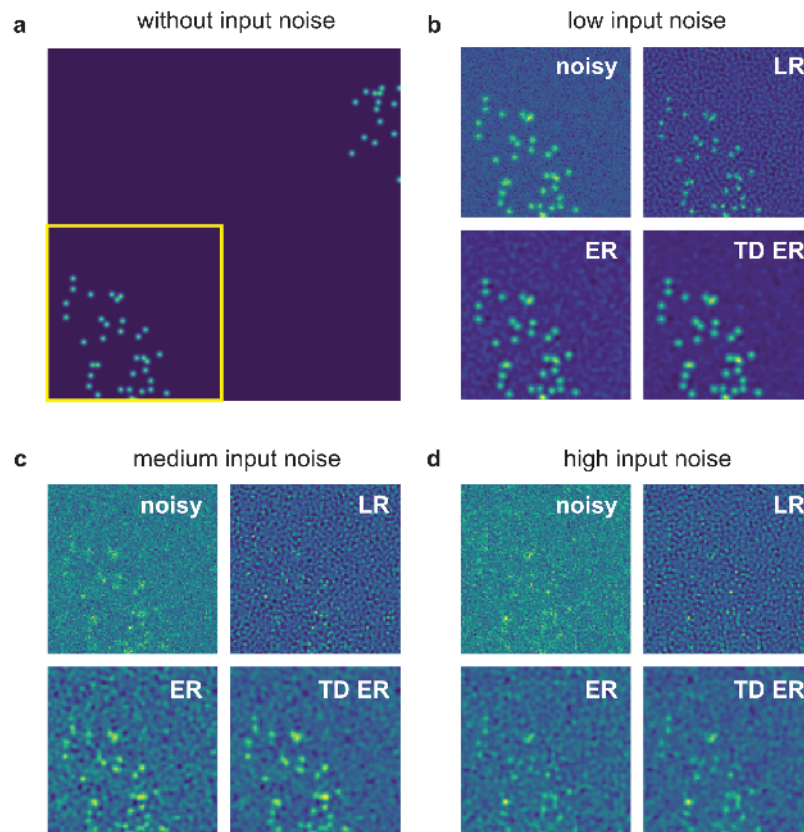


Figure 1. Example of synthetic data processed with the different deconvolution methods. (a) Sample frame of synthetic data without any added noise and before applying the PSF. The yellow box indicates the region of interest pictured in panels (b–d), which show input noisy images for various noise levels as well as image restoration results. The parameters for the entropy deconvolution are $\lambda = 0.1$ and (TD ER: $\lambda = 0.1, \lambda_T = 0.1$) and $\varepsilon = 0.001$. LR: Lucy-Richardson deconvolution; ER: entropy regularization-based deconvolution (static); TD ER: time-dependent entropy regularization-based deconvolution.

The region of interest (ROI) indicated by the yellow box is then focused on in the panels (b–d), which are all structured in the same way: The left upper image represents the noisy ROI of the image that is input into the deconvolution algorithms. The other images are the corresponding restored image ROI for LR deconvolution (right upper image), static entropy-based deconvolution (ER, left lower image) and the proposed temporal entropy-based deconvolution (TD ER, right lower image). The input noise levels are as follows: (b) low noise, (c) medium noise and (d) high noise.

For all noise levels, the proposed time-dependent algorithm presents the smallest amount of background noise and highest SNR after image restoration, with the discrepancy between time-dependent and static deconvolution becoming most evident for the high

noise level (i.e., low-SNR) input data as in panel (d). In contrast to the entropy-based approaches, LR deconvolution tends to introduce ringing artifacts to the result, which amplify the background noise for low-SNR input data. Merely for the lowest noise level shown in panel (b), the LR algorithm performs best, as it sharpens the signal, whereas the entropy algorithms tend to blur it instead.

The corresponding quantitative analysis is presented in Figure 2, showing the mean normalized SSIM as well as the estimated background noise for the image restoration approaches as a function of the input Gaussian noise level and averaged over different Poisson noise levels.

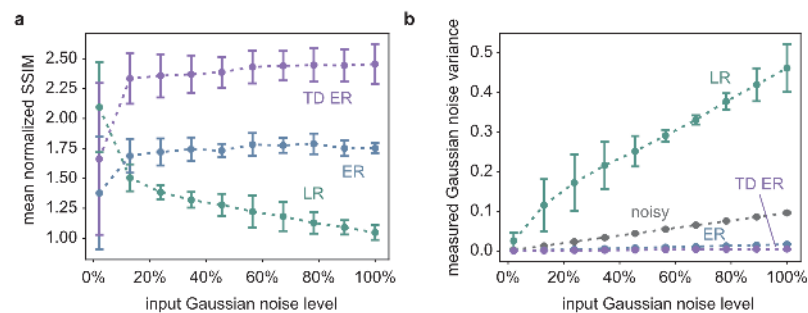


Figure 2. (a) The SSIM of the different image restoration methods, averaged over all time frames of 25 different, randomly generated synthetic datasets, such as the one in Figure 1a, normalized with respect to the SSIM between the noisy and the original image as a function of the input Gaussian noise. Thus, a value larger than one indicates image quality improvement compared to the noisy input image. The measurement points correspond to the average values obtained for three different Poisson noise levels, and the error bars indicate the influence of varying the Poisson noise levels in terms of the standard deviation of the respective different simulations. TD ER SSIM values are significantly higher than ER values and ER SSIM values significantly higher than LR values, except for the smallest Gaussian noise level ($p < 0.05$; paired, one-sided Wilcoxon signed-rank test with Bonferroni correction; based on the SSIM values of the random synthetic time series, with the values averaged over Poisson noise levels). (b) The results of the Gaussian noise estimation as a function of the input Gaussian noise for the different deconvolution methods as well as for the original noisy image, where the latter is pictured in greys and represents a plausibility check of the applied noise estimation approach. TD ER values are significantly lower than ER values and ER values significantly lower than LR values for all Gaussian noise levels.

The SSIM is calculated according to Equation (2) for the individual frames of the restored images and the original input data and averaged over all time frames. In the diagram, the respective SSIM values are normalized by dividing the SSIM obtained for an image restoration approach by the SSIM for comparison of the noisy input data and the underlying original data. Thus, SSIM values larger than one indicate an image improvement in terms of SSIM.

The quantitative data support the visual impression. The TD ER algorithm performs best, except for very low noise values, where the LR deconvolution reveals higher SSIM values. With increasing noise, image quality improvement by LR deconvolution drastically decreases in terms of SSIM (normalized SSIM values ≈ 1 ; a value of 1 indicates similar SSIM of the noisy input image and the restored image). Better results are obtained using the entropy approaches (ER: normalized SSIM of approximately 1.7; TD ER: normalized SSIM of approximately 2.4), which are optimized for processing low-SNR fluorescence microscopy data. The amount of Poisson noise has a comparatively small influence on the result, as can be seen by the error bars in Figure 2a, which show the standard deviation for processing similar image series with different Poisson noise levels.

The estimated Gaussian noise variance of the image background depicted in Figure 2b is in line with the SSIM results and the visual impression. The grey line represents a consistency check of the automated background noise estimation method, as it shows the estimated Gaussian noise variance of the noisy input image as a function of the input Gaussian noise variance. The linear relationship indicates the reliability of the respective results.

Both the ER and the TD ER algorithms considerably decrease the measured background noise, while the LR algorithm appears to magnify it with an increasing input noise level, in agreement with the visual impression of Figure 1b,c. The LR results are also the only ones that depended on the input Poisson noise level, with the standard deviation indicating this influence as explained and visualized in Figure 2a. The remaining background noise of the images obtained by both entropy algorithms as well as the background noise of the original noisy images differ only a little for different Poisson levels, and the respective error bars are too small to be pictured in Figure 2a. Overall, the smallest amount of background noise is present in the images generated using the TD ER algorithm.

2.2. Live-Cell Fluorescence Microscopy

In Figure 3, representative frames of the acquired image sequences of dataset 2 and the corresponding outputs of the deconvolution approaches are shown.

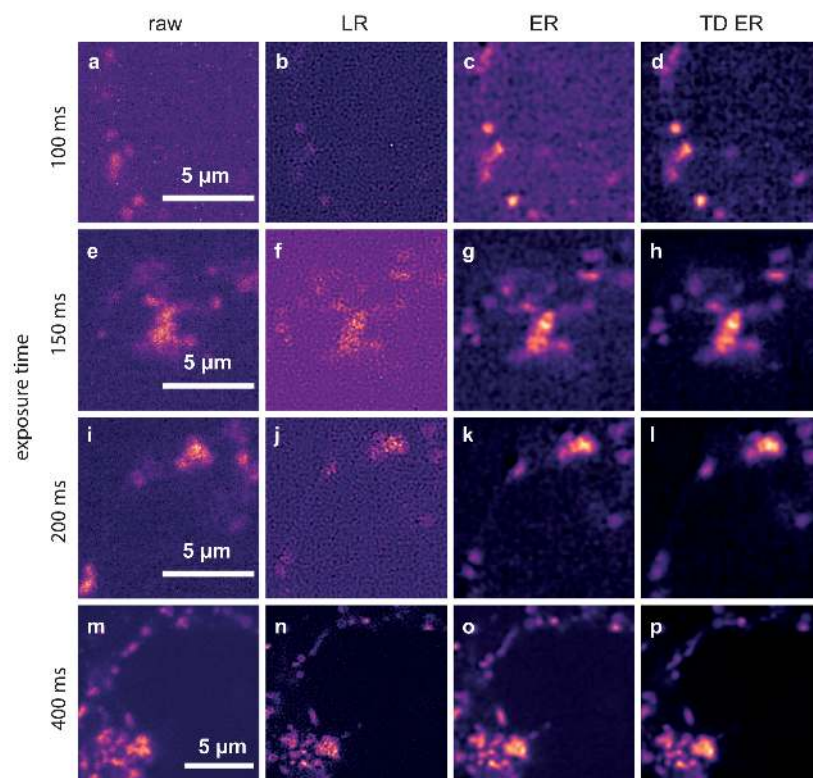


Figure 3. Comparison of the different deconvolution methods for TPC2-R.GECO.1.2 images captured with different exposure times. (a,e,i,m): raw data, captured at 100ms, 150ms, 200ms and 400ms; (b,f,j,n): images deconvolved using MATLAB's Lucy-Richardson (LR) algorithm; (c,g,k,o): images deconvolved using the static entropy algorithm (ER); (d,h,l,p): images deconvolved with the time-dependent entropy algorithm (TD ER). Parameters for the entropy algorithms are $\lambda = 2.0$ and (TD ER: $\lambda = 2.0, \lambda_T = 2.0$) and $\epsilon = 0.001$.

Movies corresponding to the results at 100ms exposure are provided as Supplementary Videos S1–S4, see Supplementary Materials.

The data represent Ca^{2+} released through the two pore channel 2 (TPC2) on lysosomes in Jurkat T-cells using TPC2-R.GECO.1.2. With this low affinity genetically encoded Ca^{2+} indicator, only Ca^{2+} at the mouth of the TPC pore can be visualized.

The first column shows raw images captured with exposure times of 100ms (a), 150ms (e), 200ms (i) and 400ms (m). The second column depicts the corresponding deconvolution results obtained with the MATLAB implementation of the LR algorithm for these exposure times. Images restored by the ER deconvolution ($\lambda = 2.0$) are shown in the third column, and the corresponding results for the proposed TD ER approach ($\lambda = 2.0, \lambda_T = 2.0$) are given in the fourth column. In both the static and time-dependent entropy algorithms, $\epsilon = 0.001$.

It can be clearly seen that the noise level in the raw images increases significantly when reducing the exposure time from 400ms to 100ms. The Lucy–Richardson deconvolution increases the noise level even further for lower exposure times, while the entropy-based algorithms perform much better (third and fourth column). The time-dependent algorithm (rightmost column) shows the least amount of noise while recovering much of the original signal. This effect is especially pronounced for the lower exposure times, where in the raw image, hardly any signal can be discerned, while our algorithm manages to recover a relatively clear signal. For very high exposure times, such as 400ms shown in the last row of Figure 3, the improvement is, however, minimal at best. While, even here, background noise is reduced, the signal also appears slightly blurred.

A more detailed look at the signal recovery is given in Figure 4.

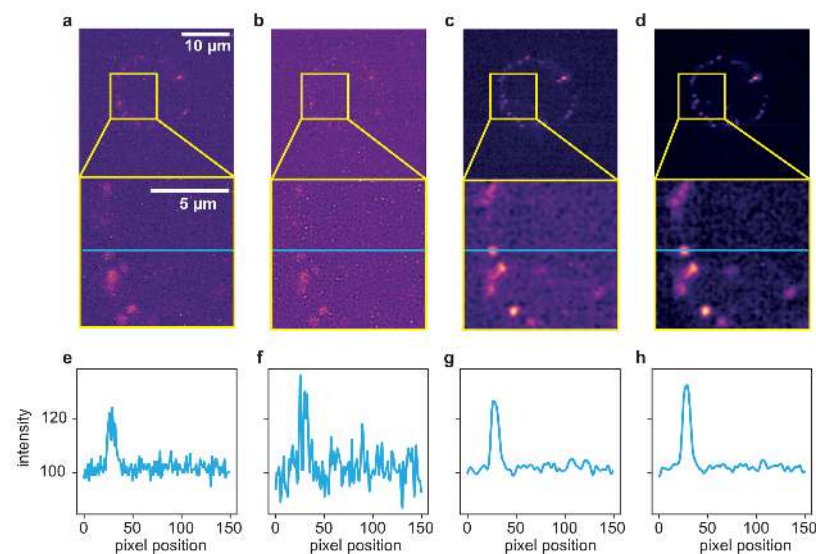


Figure 4. Comparison of the different deconvolution methods for a time series of dataset 2, captured at 100ms exposure time. (a) Raw image. (b) Deconvolved with the MATLAB Lucy–Richardson algorithm. (c) Deconvolved by ER with $\lambda = 2.0$. (d) Deconvolved with the proposed TD ER with ($\lambda = 2.0, \lambda_T = 2.0$). Each panel includes a zoomed-in region of interest indicated in yellow. (e–h) The intensity profile plotted along the blue line in the frames above. All entropy-based algorithms here use $\epsilon = 0.001$.

Here, the results for the different deconvolution methods are shown for a ROI of a time series captured with 100ms exposure time. The first column, Figure 4a, shows the raw image of a single time frame in total (first row) with a zoomed-in ROI below. Panel

(e) represents an intensity profile along the blue line in the zoom plot. The same structure applies to the other columns, with (b–d) showing the deconvolution results of the LR, ER and TD ER algorithms, respectively, and (f–h) showing the corresponding intensity profiles along the pictured blue lines. The intensity plots illustrate that the LR deconvolution seems to sharpen the signal but also amplifies the noise; based on the intensity profile, it is difficult to distinguish the signal from noise. The ER algorithm clearly recovers the signal while reducing the noise, and the TD ER further enhances the SNR.

To further illustrate the potential of the proposed approach, two additional live-cell imaging datasets were processed and analyzed.

The results obtained on dataset 3 are illustrated in Figures 5 and 6. Shown in Figure 5a is an image frame captured using Fluo-4 (upper row) and Fura Red (lower row) as indicator dyes. The frame corresponds to a time point shortly after T-cell activation. The panels show, from left to right, the original raw data and the deconvolution results obtained with the LR, the ER and the TD ER algorithms. Similar to the above experiments and datasets, the least amount of background noise is present both visually in (a) and, in terms of estimated Gaussian background noise, quantitatively in (b) and (c) in the output images of the TD ER algorithm. In fact, entropy deconvolution eliminates the background noise almost entirely. The numbers given in (b) and (c) are shown as a ratio, i.e., the noise level after image restoration divided by the estimated noise level of the raw data. Thus, values < 1 represent a decrease of background noise.

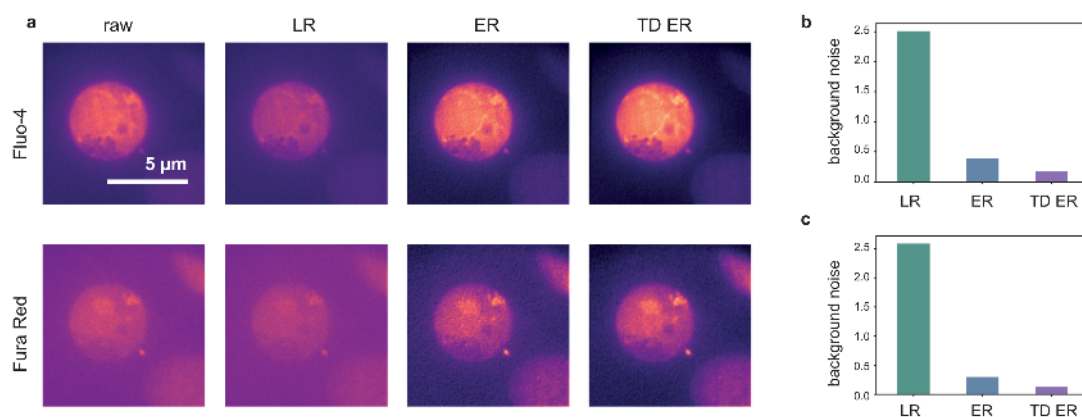


Figure 5. Panel (a): Deconvolution results for $[Ca^{2+}]_i$ imaging and frames using Fluo-4 (upper row) and Fura Red (lower row) as the indicator dye. From left to right: raw image, LR, ER and TD ER result. Entropy-based deconvolution parameters were $\lambda = 0.4$ (TD ER: $\lambda = 0.4, \lambda_T = 0.4$) and $\epsilon = 0.001$. Panels (b,c) show the estimated background noise remaining in the deconvolved images, normalized to the background noise of the raw image for the different deconvolution methods.

Performing the postprocessing process as described in [2] (rigid registration of the two channel time series data, bleaching correction, cell segmentation), the two-channel image data were then combined to ratio images representing the free cytosolic Ca^{2+} concentration, $[Ca^{2+}]_i$. One exemplary cell is shown in Figure 6, where (a–d) show the ratio images computed based on the aligned and processed raw images, the images after LR deconvolution, and after ER and TD ER image restoration. Panels (e–h) show the intensity profile along the blue line in the images above. While the ratio of the raw channels appears to be very grainy, the Ca^{2+} microdomains in the deconvolved images, in particular for ER and TD ER, can be much more easily distinguished from noise.

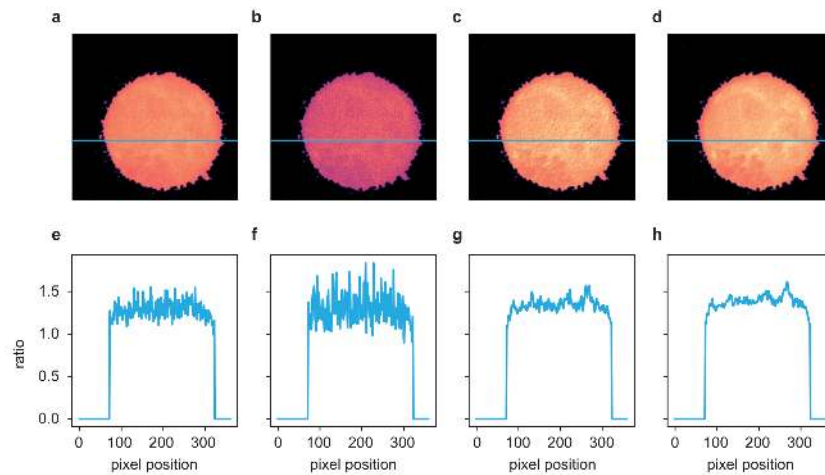


Figure 6. The ratio of the deconvolution results of the two channels from Figure 5 after postprocessing according to [2]. (a) Fluo-4/FuraRed ratio of raw images, (b) ratio of LR results, (c) ratio of ER results and (d) ratio of TD ER results. Panels (e–h) show the intensity profile plotted along the blue line in the frames above.

The results for dataset 4, a jGCaMP7b-expressing astrocyte in a mouse brain slice, are shown in Figure 7, illustrating the transferability of the developed approach to different application contexts than Ca^{2+} microdomain analysis.

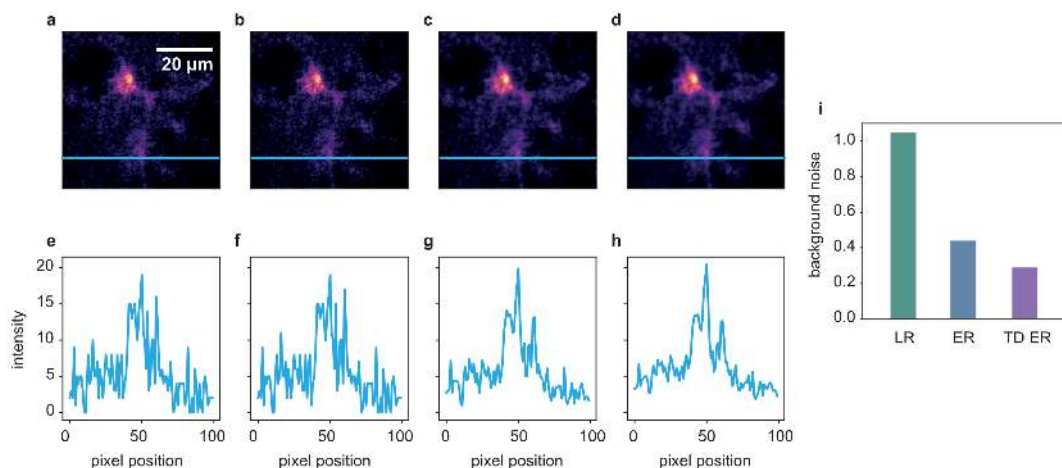


Figure 7. Deconvolution results for a jGCaMP7b-expressing astrocyte in a mouse brain slice. (a) Raw image, (b) LR result, (c) ER result and (d) TD ER result. Entropy parameters here are $\lambda = 0.05$ and $(\lambda = 0.05, \lambda_T = 0.05)$ and $\epsilon = 0.001$. Panels (e–h) show the intensity profile plotted along the blue line in the frames above. Panel (i) shows the amount of background noise remaining in the image after the application of the different deconvolution algorithms, normalized to the noise level of the original data.

While the original SNR for the input data appears to be already quite good for the large and brightly labeled cell body, the fine cell branches barely stand out against the background. Here, the entropy algorithms both considerably decrease the amount of background noise, making it easier to separate the delicate structures of the astrocyte branches from the background. For a visual impression, see Figure 7a–d and Supplementary videos

S5–S8. Quantitatively, the background noise reduction is shown in Figure 7i in the measurement of the background noise variance of the deconvolved images, again normalized onto the original noise level. The intensity profile plotted in panels (e) and (f) further confirms that the SNR, while already acceptable in the raw image, is further improved by the entropy algorithms, as shown in (g) and (h).

The computation time for a 500×500 pixel time series with 100 frames using the two entropy algorithms ranges between a few seconds and a few minutes on a standard desktop PC depending on the convergence of the algorithm, which, in turn, depends on the input data.

3. Discussion

Motivated by the intrinsically low-SNR for live-cell Ca^{2+} image sequences acquired by fluorescence microscopy at both high spatial resolution and high temporal resolution, we proposed the integration of the temporal dimension of the respective image data into variational image restoration. Method development built on an image restoration specifically tailored to particularities of fluorescence microscopy [14]. Here, (1) we extended the underlying entropy-based regularization and the dedicated numerical solving scheme to spatio-temporal image sequences, (2) demonstrated the superiority of the proposed time-dependent image restoration approach compared to static entropy-based image restoration and common LR deconvolution and (3) made the source code publicly available.

Demonstration of the advantages of the proposed image restoration approach was based on synthetic as well as real live-cell Ca^{2+} imaging data, with two of the latter being acquired in the context of Ca^{2+} microdomain formation analysis after T-cell activation and one additional dataset showing a jRCaMP7b-expressing astrocyte in a mouse brain slice. For all datasets, the observed effects were consistent: The time-dependent deconvolution considerably reduced the level of noise, in particular for low-SNR input image sequences. Therefore, we expect the approach to be promising for live-cell imaging data acquired in different application contexts.

For high(er) SNR input image sequences, the quantitative evaluation has, however, shown that the performance of the common LR deconvolution is on par with both entropy-based image restoration approaches. Moreover, visually, the entropy approaches tend to blur spots of high Ca^{2+} concentration (also particularly visible for high-SNR input data). We hypothesize that this is due to the present data fidelity term of the functional in Equation 1 and will, in the future, adjust the functional by changing the term from least squares to a Poisson noise-specific term, as low photon rates typical for fluorescence microscopy tend to obey Poisson statistics. This, however, requires a different numerical scheme and algorithm for the minimization of the overall functional and is beyond the scope of the present paper.

Moreover, at the moment, it is also not clear whether there exists theoretically and/or practically a lower SNR threshold below which the entropy-based image restoration will fail. Similarly, we tested the TD ER algorithm on imaging data acquired with a frame rate up to 40 Hz. It remains to be shown that it also performs as expected for faster image acquisition as well as for different magnification Ca^{2+} imaging data. We expect that faster and higher spatial resolution imaging leads to more continuous representation of the biological processes and structures as well as less discontinuous between-frame sample movement and motion of intracellular structures. Thus, in principle, the TD ER model should benefit from it when compared to static image restoration approaches. However, this is currently a hypothesis to be tested in future work, including in-depth comparison to the performance of other methodical approaches than LR deconvolution when applied to corresponding data. We therefore encourage other researchers to test the proposed algorithm on their data and to contact us—both in the case of problems and to share their experience and positive examples—to further optimize the proposed image restoration.

4. Materials and Methods

4.1. Mathematical Formulation

Following the concept of variational image deconvolution, the proposed approach builds on a common quadratic data fidelity term [13,14] but extended to spatio-temporal image data, i.e. $\|\mathbf{H}\mathbf{v}_t - \mathbf{w}_t\|^2$, where \mathbf{w}_t is the measured image at time or frame t , \mathbf{H} is the distortion matrix, and \mathbf{v}_t the sought solution. The direct minimization of the data fidelity term would, in practice, suppress high-frequency components of the solution and poses, mathematically, an ill-posed problem.

Thus, additional regularizing terms need to be included in the functional to be minimized. As described in the introduction, in [14], an algorithm specifically tailored to fluorescence microscopy was introduced. The main innovation was using second derivatives for a spatial smoothness-enforcing regularization functional in an entropy-like term. Here, we expanded this approach to also include a functional term that enforces smoothness in the time domain. Similar to the motivation formulated for the spatial domain in [14]—sparsity of high-intensity signals and high-magnitude derivatives—which we consider also applicable to the temporal characteristics of, e.g., Ca^{2+} microdomains, we also chose an entropy-like structure for the temporal regularization functional.

$$\mathbf{v}_{\text{opt}} = \underset{\mathbf{v} \in \mathbb{R}^K}{\text{argmin}} \left(\underbrace{\sum_{t=1}^T \|\mathbf{H}\mathbf{v}_t - \mathbf{w}_t\|^2}_{\text{data fidelity}} + \lambda \underbrace{\sum_{t=1}^T \sum_{m=1}^M \log \left[\mathbf{v}_t \circ \mathbf{v}_t + \sum_i (\mathbf{L}_i \mathbf{v}_t \circ \mathbf{L}_i \mathbf{v}_t) + \varepsilon \right]}_{\text{spatial regularization}} \right)_m + \lambda_T \underbrace{\sum_{\sigma=1}^K \log \left[\mathbf{v} \circ \mathbf{v} + \sum_i (\mathbf{D}_i \mathbf{v} \circ \mathbf{D}_i \mathbf{v}) + \varepsilon \right]}_{\text{temporal regularization}} + \lambda_N \underbrace{\mathbf{n} \cdot \mathbf{v}}_{\text{non-negativity}}, \quad (1)$$

where $\mathbf{v} \in \mathbb{R}^K$ is a vectorized processed time series comprised of T frames, each a $N_x \times N_y$ dimensional image, $M = N_x \cdot N_y$ and $K = M \cdot T$. Each individual frame is denoted by the subscript $t \in \{1, \dots, T\}$, i.e., $\mathbf{v}_t \in \mathbb{R}^M$. The measured image time series is vectorized in the variable $\mathbf{w} \in \mathbb{R}^K$, with $\mathbf{w}_t \in \mathbb{R}^M$ being the vectorized time frame at time t , and $\mathbf{v}_{\text{opt}} \in \mathbb{R}^K$ refers to the sought solution in terms of optimality with regard to the defined functional. The operator and distortion matrix $\mathbf{H} \in \mathbb{R}^{M \times M}$ is, in our case, the point spread function (PSF) in Toeplitz form.

The operators $\mathbf{L}_i \in \mathbb{R}^{M \times M}$ in the spatial regularization term represent the discretized second derivative filters in spatial directions, where the sum over i runs over $\partial^2/\partial x^2, \partial^2/\partial y^2$ and $\partial^2/\partial x \partial y$. The operator \circ refers to the Hadamard, or element-wise, product. In the temporal regularization term, the $\mathbf{D}_i \in \mathbb{R}^{K \times K}$ refer to the discretized second derivative filters containing the derivatives with respect to time. In this case, the sum over i runs over $\partial^2/\partial t^2, \partial^2/\partial x \partial t$ and $\partial^2/\partial y \partial t$.

The sum over m runs over all pixel within one time frame, so $m \in \{1 \dots M \equiv N_x \cdot N_y\}$, while σ is a composite index referring to a pixel within a specific time frame and running over all pixels in all time frames, i.e., $\sigma \in \{1 \dots K \equiv N_x \cdot N_y \cdot T\}$. In our notation, the value of a pixel in a specific time frame can thus be addressed by either v_σ or $[\mathbf{v}]_m$.

The vector $\mathbf{n} \in \mathbb{R}^K$ ensures positivity of the result and contains the entries n_σ , where $n_\sigma = 0$ if $v_\sigma \geq 0$ and $n_\sigma = v_\sigma^2$ if $v_\sigma < 0$.

The parameters λ , λ_T and λ_N are Lagrange parameters to weigh the regularization terms. They are to be determined empirically. ε is a small positive constant to avoid the occurrence of $\log(0)$ in the regularization terms.

The first term in the cost function, i.e., the data fidelity term in Equation (1), ensures the agreement with the forward model, i.e., the image distortion $\mathbf{w}_t = \mathbf{H}\mathbf{v}_t$. The second

term, controlled with Lagrange parameter λ and denoted as spatial regularization in Equation (1), is known from [14] and denotes the regularization functional enforcing smoothness within the spatial dimensions of the image. New in our proposed method is the third term proportional to λ_T . This regularization functional enforces smoothness over time. The last term proportional to λ_N is a standard term to avoid negative pixel values in the resulting image.

The optimal solution of the problem in Equation (1) is found using an iterative minimization algorithm detailed in Appendix A.

Note that the static entropy-based image restoration algorithm described in [14] is also included as a limit for $\lambda_T \rightarrow 0$ in the above description. Whenever this algorithm is referred to in the following for comparison purposes, this means our implementation with λ_T set to zero. We choose the abbreviations ER for the static entropy deconvolution and TD ER for the time-dependent entropy deconvolution.

4.2. Experiments: Imaging Data and Evaluation

The performance of the proposed spatio-temporal deconvolution was tested and compared to static entropy-based deconvolution and standard LR deconvolution (implementation of the MATLAB Image Processing Toolbox 2019a) by means of four different datasets: a synthetic image dataset, two fluorescence microscopy image datasets acquired in the context of Ca^{2+} microdomain analysis in T-cells and a last dataset acquired by confocal fluorescence Ca^{2+} imaging of an astrocyte in an acute mouse brain slice to illustrate transferability of the proposed methodical developments to a different application context.

4.2.1. Dataset 1: Synthetic Image Data

The simulation of Ca^{2+} fluorescence microscopy time series data started on a black canvas. To generate a texture, Perlin noise was added [5]. The texture was used to place "glowing" spots (small Gaussian intensity peaks) in a randomly clustered manner. Afterwards, the Perlin noise was removed, and the spots were moved over time according to Brownian motion.

To degrade the images for deconvolution evaluation purposes, they were first convolved with a PSF. The applied PSF was the same as used for the real microscopic data of dataset 3 (see below). Then, Poisson and Gaussian noise were added. The noise levels were varied to analyze the performance of the image restoration algorithms as a function of input image data SNR. This can also be interpreted to simulate different exposure times.

Poisson noise was varied by dividing the signal by a parameter before calculating the Poisson distribution. The result was re-scaled by this same parameter to preserve the original dynamic range. The Gaussian noise was varied by adding Gaussian noise with different variances. Since the exact values of these parameters are rather arbitrary in synthetic images, we scaled them to dimensionless noise levels to better illustrate the amount of noise present in the images. The exact parameters and generation methods can be seen in the published source code.

Different to subsequent real live-cell microscopy imaging data, the synthetic imaging data allow for a quantitative comparison of sought optimal images, i.e., the original input images before degradation by the PSF and noise application. For evaluation purposes, we calculated the structural similarity index (SSIM) between patches of the original images \mathbf{v}_{orig} and the restored images \mathbf{v}_{dec} , given by

$$\text{SSIM}(\mathbf{v}_{\text{orig}}, \mathbf{v}_{\text{dec}}) = \frac{(2\mu_{\mathbf{v}_{\text{orig}}}\mu_{\mathbf{v}_{\text{dec}}} + c_1)(2\sigma_{\mathbf{v}_{\text{orig}}\mathbf{v}_{\text{dec}}} + c_2)}{(\mu_{\mathbf{v}_{\text{orig}}}^2 + \mu_{\mathbf{v}_{\text{dec}}}^2 + c_1)(\sigma_{\mathbf{v}_{\text{orig}}}^2 + \sigma_{\mathbf{v}_{\text{dec}}}^2 + c_2)}, \quad (2)$$

where μ_x denotes the average and σ_x^2 the variance of the intensity values of image patch x , while σ_{xy} denotes the covariance between two image patches x and y . c_1 and c_2 are small constants.

Moreover, as an approach that requires no ground truth reference images for a quantitative assessment of image restoration success, the Gaussian noise variance of the image background was estimated according to the patch-based approach presented in [17].

4.2.2. Dataset 2: Genetically Encoded Ca^{2+} Indicator for Optimal Imaging (GECO) Tagged to Lysosomal TPC2 in Jurkat T-cells

The second dataset was acquired in the context of the analysis of the role of Ca^{2+} release processes during the formation of initial Ca^{2+} microdomains in T-cells. Jurkat T-cells were transiently transfected with two pore channel 2 (TPC2) fused to a low affinity genetically encoded Ca^{2+} indicator for optical imaging (GECO-1.2). Previously, this GECO was tagged to ORA1 channels in the plasma membrane, and only Ca^{2+} entry through Orai1 was visualized [18]. Here, only Ca^{2+} released from the lysosomes through TPC2 should be detected.

The images were acquired with a 100-fold magnification objective (Zeiss, Jena, Germany) fitted in a super-resolution spinning disc microscope (Visitron) and a scientific complementary metal-oxide-semiconductor camera (Orca-Flash 4.0, C13440-20CU, Hamamatsu Photonics, Hamamatsu, Japan). Different times of acquisition were used for time lapse series (100 ms, 150 ms, 200 ms, 400 ms), a 561 nm laser adopted to excite TPC2-R.GECO.1.2, and the emission wavelength was detected at 606/54 nm.

4.2.3. Dataset 3: Free Cytosolic Ca^{2+} Concentration Imaging in Jurkat T-cells

The third dataset depicts the free cytosolic Ca^{2+} concentration ($[\text{Ca}^{2+}]_i$) of Jurkat T-cells immediately after T-cell activation. Imaging was performed as detailed in [1,2]. The cells were loaded with Fluo4-AM and Fura Red-AM. For T-cell stimulation, protein G beads (Merck Millipore, Burlington, MA, USA) were coated with antibodies (human anti-CD3 (OKT-3)). The images were acquired with a super-resolution spinning disc microscope (Visitron, Puchheim, Germany) with 280-fold magnification (100-fold objective and 2.8-fold super-resolution spinning disc) and a Prime 95B back-illuminated sCMOS camera (Teledyne Photometrics, Tucson, AZ, USA). A dual-view module (Optical Insights, PerkinElmer Inc., Waltham, MA, USA) was used to split the emission wavelengths (laser: excitation 488; beam splitter, 495; emission 1, 542/50; emission 2, 650/57). The exposure time was 30 ms.

4.2.4. Dataset 4: Confocal Ca^{2+} Imaging in Astrocytes In Situ

The fourth dataset was acquired in an astrocyte in an acute mouse brain slice. The genetically encoded Ca^{2+} indicator jRCaMP7b (Addgene # 171118) was subcloned into a AAV-PhP.eB vector under the control of the GFAP promoter, and viruses were systemically applied by retrobulbar injection [19]. After 14 days, jRCaMP7b-expressing astrocytes were visualized with a confocal fluorescence microscope (eC1, Nikon, Düsseldorf, Germany; equipped with a 16× objective, NA 0.8) in acute brain slices of the olfactory bulb using a 488 nm laser for excitation (emission filter 515/15) at a frame rate of 1 Hz.

Supplementary Materials: Supplementary materials are available online at <https://www.mdpi.com/article/10.3390/ijms1010000/s1>.

Author Contributions: Conceptualization, L.-M.W., A.H.G., B.-P.D. and R.W.; methodology, L.-M.W. and R.W.; software, L.-M.W.; validation, L.-M.W. and R.W.; formal analysis, L.-M.W.; investigation, L.-M.W., S.A.K., V.B., C.L. and R.W.; resources, all authors; data curation, L.-M.W.; writing—original draft preparation, L.-M.W., B.-P.D., C.L. and R.W.; writing—review and editing, all authors; visualization, L.-M.W.; supervision, R.W.; project administration, B.-P.D. and R.W.; funding acquisition, B.-P.D., R.W., A.H.G., C.E.G. and C.L. All authors have read and agreed to the published version of the manuscript.

Funding: This research was funded by Deutsche Forschungsgemeinschaft (DFG, German Research Foundation) grant number 335447717—SFB1328, projects A01 to A.H.G., A02 to B.-P.D. and R.W., and A07 to C.E.G. and C.L.

Data Availability Statement: The source code of the proposed method and the synthetic datasets are publicly available at <https://github.com/IPMI-ICNS-UKE/TDEntropyDeconvolution>, accessed on 26 October 2021.

Conflicts of Interest: The authors declare no conflict of interest. The funders had no role in the design of the study; in the collection, analyses, or interpretation of data; in the writing of the manuscript; or in the decision to publish the results.

Abbreviations

The following abbreviations are used in this manuscript:

ER	static entropy deconvolution
GECO	genetically encoded Ca ²⁺ indicator for optimal imaging
LR	Lucy–Richardson
PSF	Point spread function
ROI	Region of interest
SNR	Signal-to-noise ratio
SSIM	Structural similarity index
TD ER	time-dependent entropy deconvolution
TPC	two pore channel

Appendix A. Algorithm Details

Appendix A.1. Minimization of Cost Functional (1)

As described in the main text, our algorithm is conceptually an extension of the entropy deconvolution proposed by Arigovindan et al. [14]. There was, however, no corresponding source code available. We, therefore, developed the program completely from scratch with the ideas in [14] as a starting point. Introduced in Section 4, the cost functional to minimize is given by

$$U(\mathbf{v}) = \sum_{t=1}^T \|\mathbf{H}\mathbf{v}_t - \mathbf{w}_t\|^2 + \lambda \sum_{t=1}^T \sum_{m=1}^M \log \left[\mathbf{v}_t \circ \mathbf{v}_t + \sum_i (\mathbf{L}_i \mathbf{v}_t \circ \mathbf{L}_i \mathbf{v}_t) + \varepsilon \right]_m + \lambda_T \sum_{\sigma=1}^{K-T, M} \log \left[\mathbf{v} \circ \mathbf{v} + \sum_i (\mathbf{D}_i \mathbf{v} \circ \mathbf{D}_i \mathbf{v}) + \varepsilon \right]_{\sigma} + \lambda_N \mathbf{n} \cdot \mathbf{v} \quad (\text{A1})$$

Taking the derivative and setting it to zero leads to the following minimality condition

$$\mathbf{H}^T \mathbf{H} \mathbf{v}_t + \lambda \mathbf{c} \circ \mathbf{v}_t + \lambda \sum_i \mathbf{L}_i^T (\mathbf{c} \circ \mathbf{L}_i \mathbf{v}_t) + \left[\lambda_T \mathbf{k} \circ \mathbf{v} + \lambda_T \sum_i \mathbf{D}_i^T (\mathbf{k} \circ \mathbf{D}_i \mathbf{v}) + \lambda_N \mathbf{n}' \circ \mathbf{v} \right]_t = \mathbf{H}^T \mathbf{w}_t \quad (\text{A2})$$

for the t -th time frame. The elements of the vector \mathbf{c} are given by

$$c_{(t,m)} = \left[v_{(t,m)}^2 + \sum_i \left(\sum_{l=1}^M L_{i,kl} v_{(t,l)} \right)^2 + \varepsilon \right]^{-1} \quad (\text{A3})$$

where (t, m) denotes a composite index to reference both the time frame t and pixel location m . The elements of the vector \mathbf{k} are given by

$$k_{\sigma} = \left[v_{\sigma}^2 + \sum_i \left(\sum_{\tau=1}^K D_{i,\sigma\tau} v_{\tau} \right)^2 + \varepsilon \right]^{-1}. \quad (\text{A4})$$

Since Equation (A2) is solved iteratively, a starting condition is needed. It is useful to define an approximation that can be easily inverted. Extending the ansatz in [14], we choose the following initial condition for the t -th time frame

$$\mathbf{H}^T \mathbf{H} \mathbf{v}_i^{(0)} + \lambda \left(\mathbf{1} + \sum_i \mathbf{L}_i^T \mathbf{L}_i \right) \mathbf{v}_i^{(0)} + \lambda_T \left[\left(\mathbf{1} + \sum_i \mathbf{D}_i^T \mathbf{D}_i \right) \mathbf{v}^{(0)} \right]_i = \mathbf{H}^T \mathbf{w}_i. \quad (\text{A5})$$

Note that the matrices \mathbf{H} , \mathbf{L}_i and \mathbf{D}_i are circulant to represent the convolution. Therefore, they are diagonalized by the discrete Fourier transform. This leads to the following solution to Equation (A5):

$$\hat{\mathbf{v}}_i^{(0)} = \hat{\mathbf{P}}_i^{-1} \text{diag}(\hat{\mathbf{h}}^+) \hat{\mathbf{w}}_i \quad (\text{A6})$$

where

$$\hat{\mathbf{P}}_i = \text{diag}(\hat{\mathbf{h}}^+) \text{diag}(\hat{\mathbf{h}}) + \lambda \left(\mathbf{1} + \sum_i \text{diag}(\hat{\mathbf{L}}_i) \text{diag}(\hat{\mathbf{L}}_i^+) \right) + \lambda_T \left(\mathbf{1} + \sum_i \text{diag}(\hat{\mathbf{D}}_i) \text{diag}(\hat{\mathbf{D}}_i^+) \right)_i. \quad (\text{A7})$$

Here, $\hat{\cdot}$ denotes the Fourier transform and $\text{diag}(\mathbf{x})$ the diagonal matrix with entries \mathbf{x} along the diagonal. For circulant matrices, the eigenvalues are given by one of its rows (all other rows are permutations), and the Fourier transform is simply a diagonal matrix with these values along the diagonal.

Going back to the full problem, the left-hand side of Equation (A2) can be re-written as a single operator as

$$\mathbf{A} \mathbf{v} = \mathbf{b}, \quad (\text{A8})$$

where $\mathbf{b}_i = \mathbf{H}^T \mathbf{w}_i$, and \mathbf{v} again denotes the entire time series. The solution, i.e., \mathbf{v} , can be found iteratively following the ansatz of [14] with

$$\mathbf{v}^{(k+1)} = \mathbf{v}^{(k)} + \zeta_k (\tilde{\mathbf{A}}^{(k)})^{-1} [\mathbf{b} - \mathbf{A}^{(k)} \mathbf{v}^{(k)}], \quad (\text{A9})$$

where k is the iteration index, ζ_k a damping factor and $\tilde{\mathbf{A}}^{(k)}$ an approximation of $\mathbf{A}^{(k)}$ that can be inverted easily. Here

$$\tilde{\mathbf{A}}^{(k)} = \mathbf{P}_I \text{diag}(\mathbf{m}^{(k)}) \mathbf{P}_I, \quad (\text{A10})$$

where \mathbf{P}_I is the inverse Fourier transform of $(\sqrt{\hat{\mathbf{P}}})^{-1}$, where $\hat{\mathbf{P}}$ is given by Equation (A7) and $\text{diag}(\mathbf{m}^{(k)})$ is the diagonal approximation of $\mathbf{A}^{(k)}$ with

$$\mathbf{m}_i^{(k)} = \lambda_N \mathbf{n}_i^{(k)} + \lambda \left(\mathbf{c}_i^{(k)} + \sum_i \mathbf{L}_i (\mathbf{L}_i \mathbf{c}_i^{(k)}) \right) + \lambda_T \left(\mathbf{k}^{(k)} + \sum_i \mathbf{D}_i (\mathbf{D}_i \mathbf{k}^{(k)}) \right) + \tilde{\mathbf{h}}_i, \quad (\text{A11})$$

where the vectors \mathbf{c} and \mathbf{k} are given by Equations (A3) and (A4), and the vector $\tilde{\mathbf{h}}$ is constant with elements

$$\tilde{h}_k = \sum_i \sum_j H_{ij}^2 \quad \forall k \in \{1, \dots, M\}. \quad (\text{A12})$$

To facilitate notation in the algorithm, some abbreviations are introduced as follows

$$\begin{aligned} \mathbf{R}_i^{(k)} &= \mathbf{b} - \mathbf{A}^{(k)} \mathbf{v}^{(k)} \\ &= \mathbf{H}^T \mathbf{w}_t - \mathbf{H}^T \mathbf{H} \mathbf{v}_i^{(k)} - \lambda \mathbf{c}^{(k)} \circ \mathbf{v}_i^{(k)} + \lambda \sum_i \mathbf{L}_i^T (\mathbf{c}^{(k)} \circ \mathbf{L}_i \mathbf{v}_i^{(k)}) \\ &\quad + \left[\lambda_T \mathbf{k}^{(k)} \circ \mathbf{v}^{(k)} + \lambda_T \sum_i \mathbf{D}_i^T (\mathbf{k}^{(k)} \circ \mathbf{D}_i \mathbf{v}^{(k)}) + \lambda_N \mathbf{n}^t \circ \mathbf{v}^{(k)} \right]_t \end{aligned} \quad (\text{A13})$$

with \mathbf{c} and \mathbf{k} given by Equation (??) and $\lambda_N = 100\lambda$. Another definition is

$$\mathbf{U}_i^{(k)} = (\tilde{\mathbf{A}}^{(k)})^{-1} [\mathbf{b} - \mathbf{A}^{(k)} \mathbf{v}^{(k)}] = \mathbf{P}_t (\text{diag}(\mathbf{m}^{(k)}) (\mathbf{P}_t \mathbf{R}^{(k)})). \quad (\text{A14})$$

To evaluate the “goodness” of the iteration result, the following measure is introduced

$$e^{(k)} \equiv \sum_{ij} (\tilde{R}_{ij}^{(k)})^2. \quad (\text{A15})$$

The resulting deconvolution algorithm is given in Algorithm 1.

Algorithm 1: Deconvolution

input : measured image \mathbf{w} , PSF \mathbf{H} , differential operators \mathbf{L}_i , \mathbf{D}_i , Lagrange parameters λ , λ_T , offset ϵ , max iterations N_{\max} , tolerance δ
output : deconvolved time series \mathbf{v}_{opt}
 initialization: calculate initial guess $\hat{\mathbf{v}}_i^{(0)} = \hat{\mathbf{P}}_t^{-1} \text{diag}(\hat{\mathbf{h}}^+) \hat{\mathbf{w}}_t$ for each time frame t ;
 set $\zeta = 0.8$;
while $k < N_{\max}$ and $e^{(k)} > \delta$ **do**
 calculate $\mathbf{U}^{(k)}$;
 while $\tilde{e}^{(k)} > e^{(k)}$ **do**
 calculate $\hat{\mathbf{v}}^{(k)} = \mathbf{v}^{(k)} + \zeta_k \mathbf{U}^{(k)}$;
 calculate $\tilde{\mathbf{R}}^{(k)} = \mathbf{b} - \mathbf{A}^{(k)} \hat{\mathbf{v}}^{(k)}$;
 calculate $\tilde{e}^{(k)} = \sum_{ij} (\tilde{R}_{ij}^{(k)})^2$;
 set $\zeta = 0.7\zeta$;
 end
 set $e^{(k+1)} = \tilde{e}^{(k)}$;
 set $\mathbf{R}^{(k+1)} = \tilde{\mathbf{R}}^{(k)}$;
 set $\mathbf{v}^{(k+1)} = \hat{\mathbf{v}}^{(k)}$;
 set $k=k+1$;
end

Appendix A.2. Practical Notes

It should be noted that to facilitate notation, especially for the time dependence, matrix notation has been used throughout the previous section(s). However, it is computationally highly impractical to implement the algorithm exactly this way due to the enormous matrix sizes. In our implementation, the matrix product between a circular matrix and a vector, such as the image degradation denoted by Hv is actually implemented as a convolution $h * v$, where $h(x, y)$ is the point spread function and $v(x, y)$ the image function depending on pixel values x, y . A matrix product with a transposed matrix, such as $H^T v$, is equivalent to convolution with a shifted kernel or a cross correlation, i.e., $h \cdot v$.

The parameters λ , λ_T , λ_N and as well as the maximum number of iterations N need to be determined empirically and can be widely different dependent on the type of data. In practice, λ_N is set to $100 \cdot \lambda$, and ϵ is simply a small number, such as 0.001. The best maximum number of iterations is often only $N = 1$. This leaves λ and λ_T to be chosen, which often work best when they are of a similar order of magnitude. Thus, effectively, only one parameter has to be chosen.

The source code is written in Python and provided at <https://github.com/IPMI-ICNS-UKE/TDEntropyDeconvolution>, accessed on 26 October 2021. The repository also provides a detailed documentation on how to use the code and example scripts for synthetic datasets, such as those shown in Figure 1. The example scripts can be used as starting point. At the moment, the code is implemented for 2D (i.e., static data, processed by the static ER algorithm) and 2D+time series data. If you are interested in using the approach for 3D and 3D+time data, please contact us. For the TD ER approach, the time series data have (technically) to consist of at least three frames. The maximum frame number and the maximum size of the frames is limited by the computer hardware. Currently, a time series of 600 frames, each of size 500×500 pixels, occupies approximately 2.4 GB RAM; however, for a frame size of 2048×2048 pixels, the demand increases to 40 GB. As the run time also scales with $O(n \log n)$ with n as the number of pixels of the time series, we recommend working on pre-defined regions of interest.

References

1. Wolf, I.M.A.; Diercks, B.P.; Gattkowsky, E.; Czarniak, F.; Kempinski, J.; Werner, R.; Schetelig, D.; Mittrücker, H.W.; Schumacher, V.; von Osten, M.; et al. Frontrunners of T cell activation: Initial, localized Ca^{2+} signals mediated by NAADP and the type 1 ryanodine receptor. *Sci. Signal.* **2015**, *8*, ra102–ra102. doi:10.1126/scisignal.aab0863.
2. Diercks, B.P.; Werner, R.; Weidemüller, P.; Czarniak, F.; Hernandez, L.; Lehmann, C.; Rosche, A.; Krüger, A.; Kaufmann, U.; Vaeth, M.; et al. ORAI1, STIM1/2, and RYR1 shape subsecond Ca^{2+} microdomains upon T cell activation. *Sci. Signal.* **2018**, *11*, eaat0358. doi:10.1126/scisignal.aat0358.
3. Ettinger, A.; Wittmann, T. Chapter 5—Fluorescence live cell imaging. In *Methods in Cell Biology*; Waters, J.C., Wittman, T., Eds.; Academic Press: Cambridge, MA, USA, 2014; Volume 123, pp. 77–94. doi:10.1016/B978-0-12-420138-5.00005-7.
4. Fujiwara, K.; Tanaka, H.; Mani, H.; Nakagami, T.; Takamatsu, T. Burst Emergence of Intracellular Ca^{2+} Waves Evokes Arrhythmic Oscillatory Depolarization via the Na^+ - Ca^{2+} Exchanger. *Circ. Res.* **2008**, *103*, 509–518. doi:10.1161/CIRCRESAHA.108.176677.
5. Weigert, M.; Schmidt, U.; Boothe, T.; Müller, A.; Dibrov, A.; Jain, A.; Wilhelm, B.; Schmidt, D.; Broaddus, C.; Culley, S.; et al. Content-aware image restoration: pushing the limits of fluorescence microscopy. *Nat. Methods* **2018**, *15*, 1090–1097. doi:10.1038/s41592-018-0216-7.
6. Chen, J.; Sasaki, H.; Lai, H.; Su, Y.; Liu, J.; Wu, Y.; Zhovmer, A.; Combs, C.A.; Rey-Suarez, I.; Chang, H.Y.; et al. Three-dimensional residual channel attention networks denoise and sharpen fluorescence microscopy image volumes. *Nat. Methods* **2021**, *18*, 678–687. doi:10.1038/s41592-021-01155-x.
7. Belthangady, C.; Royer, L.A. Applications, promises, and pitfalls of deep learning for fluorescence image reconstruction. *Nat. Methods* **2019**, *16*, 1215–1225. doi:10.1038/s41592-019-0458-z.
8. Wiener, N. *Extrapolation, Interpolation, and Smoothing of Stationary Time Series: with Engineering Applications*; MIT Press: Cambridge, MA, USA, 1964; Volume 8.
9. Boyat, A.K.; Joshi, B.K. Image denoising using wavelet transform and wiener filter based on log energy distribution over Poisson-Gaussian noise model. In *Proceedings of the 2014 IEEE International Conference on Computational Intelligence and Computing Research, Bhopal, India, 14–16 November 2014*; pp. 1–6. doi:10.1109/ICIC.2014.7238350.
10. Richardson, W.H. Bayesian-Based Iterative Method of Image Restoration. *J. Opt. Soc. Am. B* **1972**, *62*, 55. doi:10.1364/JOSA.62.000055.
11. Lucy, L.B. An iterative technique for the rectification of observed distributions. *Astron. J.* **1974**, *79*, 745. doi:10.1086/111605.

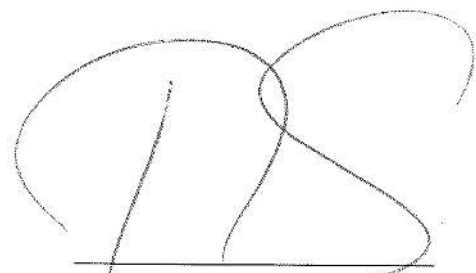
12. Sarder, P.; Nehorai, A. Deconvolution methods for 3-D fluorescence microscopy images. *IEEE Signal Process. Mag.* **2006**, *23*, 32–45. 00413. doi:10.1109/MSP.2006.1628876.
13. Sage, D.; Donati, L.; Soulez, F.; Fortun, D.; Schmit, G.; Seitz, A.; Guiet, R.; Vonesch, C.; Unser, M. DeconvolutionLab2: An open-source software for deconvolution microscopy. *Methods* **2017**, *115*, 28–41. doi:10.1016/j.jymeth.2016.12.015.
14. Arigovindan, M.; Fung, J.C.; Elnatan, D.; Mennella, V.; Chan, Y.H.M.; Pollard, M.; Branlund, E.; Sedat, J.W.; Agard, D.A. High-resolution restoration of 3D structures from widefield images with extreme low signal-to-noise-ratio. *Proc. Natl. Acad. Sci. USA* **2013**, *110*, 17344–17349. doi:10.1073/pnas.1315675110.
15. Hugelier, S.; Eilers, P.H.C.; Devos, O.; Ruckebusch, C. Improved superresolution microscopy imaging by sparse deconvolution with an interframe penalty. *J. Chemom.* **2017**, *31*, e2847. doi:10.1002/cem.2847.
16. Ahmad, M.; Hugelier, S.; Vitale, R.; Eilers, P.; Ruckebusch, C. A criterion for automatic image deconvolution with L0-norm regularization. *J. Chemom.* **2020**, *34*, e3227. doi:10.1002/cem.3227.
17. Paul, P.; Duessmann, H.; Bernas, T.; Huber, H.; Kalamatianos, D. Automatic noise quantification for confocal fluorescence microscopy images. *Comput. Med Imaging Graph.* **2010**, *34*, 426–434. doi:10.1016/j.compmedimag.2010.04.001.
18. Dynes, J.L.; Amcheslavsky, A.; Cahalan, M.D. Genetically targeted single-channel optical recording reveals multiple Orai1 gating states and oscillations in calcium influx. *Proc. Natl. Acad. Sci. USA* **2016**, *113*, 440–445. doi:10.1073/pnas.1523410113.
19. Lohr, C.; Beiersdorfer, A.; Fischer, T.; Hirnet, D.; Rotermund, N.; Sauer, J.; Schulz, K.; Gee, C.E. Using Genetically Encoded Calcium Indicators to Study Astrocyte Physiology: A Field Guide. *Front. Cell. Neurosci.* **2021**, *15*, 690147. doi:10.3389/fncel.2021.690147.

2.1.1 Publication I: Contribution

In this publication, a deconvolution algorithm (Arigovindan et al., 2013) was extended by a regularization term emphasizing the time dependency of an image sequence, S.10 term (1). The algorithm can be used to deconvolve Ca^{2+} microdomain sequences or other low SNR image sequences to increase the resolution of the sequence computationally. The algorithm was tested on different image sequence datasets. Two datasets concern Ca^{2+} imaging in T cells. In one of these datasets, lysosomal TPCs of Jurkat T cells were tagged with a genetically encoded Ca^{2+} indicator to visualize local lysosomal Ca^{2+} release. For the other dataset, Jurkat T cells were loaded with Fluo4 and FuraRed to visualize cytosolic Ca^{2+} microdomains. Moreover, the algorithm by Arigovinian and co-workers (Arigovindan et al., 2013) was implemented and tested on static images in our lab. I was involved in data acquisition and implementing the algorithm in the *Calcium Signaling* working group. Since the algorithm was written in the scripting language Python, I was responsible for installing all necessary programs to run the script in the laboratory of the *Calcium Signaling* group and for testing the script itself and the user-friendliness of the script. Moreover, I assisted adjusting the algorithm's parameters, e.g., for the analytical calculation of the PSF, for the microscope system used for the data acquisition. I was also involved in reviewing and editing the manuscript.

Hamburg, May 13, 2022

Place, Date



Signature of the supervisor

Prof. Dr. Dr. Andreas H. Guse
Direktor

2.2 Publication II

Published in February 2022 in Sci. Adv., Science Advances, 8(5), eabl9770, DOI: 10.1126/sciadv.abl9770, <https://www.science.org/doi/10.1126/sciadv.abl9770>

P2X4 and P2X7 are essential players in basal T cell activity and Ca²⁺ signaling milliseconds after T cell activation

Valerie J. Brock 1, Insa M. A. Wolf 1, Marco Er-Lukowiak 2, Niels Lory 3, Tobias Stähler 3, Lena-Marie Woelk 4, Hans-Willi Mittrücker 3, Christa E. Müller 5, Friedrich Koch-Nolte 3, Björn Rissiek 2, René Werner 4, Andreas H. Guse 1, Björn-Philipp Diercks 1*

1 The Ca²⁺ Signalling Group, Department of Biochemistry and Molecular Cell Biology, University Medical Center Hamburg-Eppendorf, 20246 Hamburg, Germany

2 Department of Neurology, University Medical Centre Hamburg Eppendorf, 20246 Hamburg, Germany

3 Department of Immunology, University Medical Centre Hamburg Eppendorf, 20246 Hamburg, Germany

4 Department of Computational Neuroscience, University Medical Centre Hamburg Eppendorf, 20246 Hamburg, Germany

5 Department of Pharmacy, University of Bonn, 53121 Bonn, Germany.

* Correspondence: b.diercks@uke.de

CELL BIOLOGY

P2X4 and P2X7 are essential players in basal T cell activity and Ca²⁺ signaling milliseconds after T cell activation

Valerie J. Brock¹, Insa M. A. Wolf¹, Marco Er-Lukowiak², Niels Lory³, Tobias Stähler³, Lena-Marie Woelk⁴, Hans-Willi Mittrücker³, Christa E. Müller⁵, Friedrich Koch-Nolte³, Björn Rissiek², René Werner⁴, Andreas H. Guse¹, Björn-Philipp Diercks^{1*}

Initial T cell activation is triggered by the formation of highly dynamic, spatiotemporally restricted Ca²⁺ microdomains. Purinergic signaling is known to be involved in Ca²⁺ influx in T cells at later stages compared to the initial microdomain formation. Using a high-resolution Ca²⁺ live-cell imaging system, we show that the two purinergic cation channels P2X4 and P2X7 not only are involved in the global Ca²⁺ signals but also promote initial Ca²⁺ microdomains tens of milliseconds after T cell stimulation. These Ca²⁺ microdomains were significantly decreased in T cells from P2rx4^{-/-} and P2rx7^{-/-} mice or by pharmacological inhibition or blocking. Furthermore, we show a pannexin-1-dependent activation of P2X4 in the absence of T cell receptor/CD3 stimulation. Subsequently, upon T cell receptor/CD3 stimulation, ATP release is increased and autocrine activation of both P2X4 and P2X7 then amplifies initial Ca²⁺ microdomains already in the first second of T cell activation.

INTRODUCTION

Efficient immune response requires precisely coordinated signaling pathways, both for cell-to-cell communication and for intracellular signal transduction. Important examples for these molecules involved in T cell activation are Ca²⁺ ions that act intracellularly or adenosine triphosphate (ATP) as a proinflammatory purinergic mediator (1, 2). The signaling pathways of these molecules are prominent targets for therapeutics (3–6). As T cell activation and signaling provide many potential spots for medical intervention, uncovering interactions between different signaling molecules will improve therapeutical approaches. T cell receptor (TCR)/CD3 complex-stimulated initial Ca²⁺ microdomains in T cells are evoked by the production of nicotinic acid adenine dinucleotide phosphate (NAADP), the most potent Ca²⁺-mobilizing second messenger (7), targeting ryanodine receptor type 1 (RYR1). Furthermore, RYR1 and ORAI1 channels, the latter activated by clusters of “stromal interacting molecule” (STIM) 1 and 2, closely collaborate in this process, likely in endoplasmic reticulum (ER)-plasma membrane (PM) junctions (8, 9). These initial Ca²⁺ microdomains are described as short-lived, highly dynamic Ca²⁺ signals with amplitudes of approximately 200 to 400 nM in primary mouse T cells arising in tens of milliseconds to seconds after stimulation of the TCR/CD3 complex (8, 9). Furthermore, preformed clusters of STIM1 and ORAI1 were found in T cells, resulting in lower and less frequent Ca²⁺ microdomains already without direct stimulation of the TCR/CD3 complex, suggesting a low-grade preactivation of these cells (9). Recently, a long sought-after NAADP binding protein named “hematological and neurological expressed 1-like protein” (HN1L)/“Jupiter microtubule associated homolog 2”

(JPT2) was found (10, 11). Knockout (KO) of HN1L/JPT2 significantly reduced the number of Ca²⁺ microdomains in primary T cells (10), similar to inhibition of NAADP by NAADP antagonist BZ194 treatment or KO of RYR1 (8, 9). Targeting NAADP signaling in a rat model of experimental autoimmune encephalomyelitis by BZ194 resulted in decreased proinflammatory cytokines and attenuated clinical symptoms (6).

P2X channels are ligand-gated ion channels activated by ATP (12–14). The two purinergic channels P2X4 and P2X7 have been shown to play an essential role in T cell function (15) and to amplify global Ca²⁺ signaling during T cell activation (16–18). Targeting P2X7 in a mouse model of contact hypersensitivity, a P2X7-inhibiting nanobody, namely, 13A7-HLE, decreased local inflammation by reducing inflammatory cytokine levels (19).

It is known that purinergic signaling is connected to Ca²⁺ signaling: An increasing Ca²⁺ concentration via store-operated Ca²⁺ entry (SOCE) through ORAI1 during T cell activation promotes the production of ATP inside the mitochondria immediately after TCR stimulation (18). ATP is transported to the cytosol and is subsequently released via pannexin-1 (PANX1) hemichannels, where it activates P2X4 and P2X7 channels in an autocrine manner, resulting in an influx of Ca²⁺. These Ca²⁺ signals were visualized several minutes after TCR stimulation (16–18). Impaired purinergic signaling caused by inhibition of the P2X4 channel in human and mouse T cells prevents T cell proliferation and migration (20), demonstrating the important physiological role of purinergic signaling on general T cell function.

In the present study, by using P2rx4^{-/-} and P2rx7^{-/-} T cells or inhibiting compounds or nanobodies, we show that P2X4 and P2X7 are already involved in the initial step of T cell activation, the generation of initial Ca²⁺ microdomains tens of milliseconds after TCR stimulation. By inhibition of PANX1 or degradation of extracellular ATP, we demonstrate that PANX1 delivers ATP for the extracellular activation of the two P2X channels in this initial step of T cell activation. Moreover, we show that low-grade preactivation of unstimulated T cells not only is dependent on the interaction of STIM1 and ORAI1 (9) but also relies on basal ATP release via PANX1 and

¹The Ca²⁺ Signalling Group, Department of Biochemistry and Molecular Cell Biology, University Medical Center Hamburg-Eppendorf, 20246 Hamburg, Germany. ²Department of Neurology, University Medical Centre Hamburg Eppendorf, 20246 Hamburg, Germany. ³Department of Immunology, University Medical Centre Hamburg Eppendorf, 20246 Hamburg, Germany. ⁴Department of Computational Neuroscience, University Medical Centre Hamburg Eppendorf, 20246 Hamburg, Germany. ⁵Department of Pharmacy, University of Bonn, 53121 Bonn, Germany. *Corresponding author. Email: b.diercks@uke.de

SCIENCE ADVANCES | RESEARCH ARTICLE

autocrine activation of P2X4. Thus, our data indicate that purinergic signaling not only amplifies global Ca^{2+} events during T cell activation but also plays an essential role in fine-tuning the basal activity and the initial activation of T cells, opening up advanced possibilities for clinical interventions.

RESULTS

P2X4 and P2X7 are involved in the formation of initial Ca^{2+} microdomains in primary T cells

To analyze the impact of P2X4 and P2X7 on initial Ca^{2+} microdomains, we used a high-resolution Ca^{2+} live-cell imaging system with an acquisition rate of 40 frames/s (8, 9) and freshly isolated primary CD4^+ T cells from wild-type (WT), $\text{P2rx4}^{-/-}$ and $\text{P2rx7}^{-/-}$ mice on a BALB/c background (21). Cells were stimulated with anti-CD3/anti-CD28-coated beads to mimic an immune synapse and stimulation via TCR/CD3 complex plus costimulation via CD28 (further termed TCR/CD3 stimulation). Initial Ca^{2+} microdomains were analyzed in a period from 0.5 s before and up to 15 s after bead contact (Fig. 1A). Directly (50 to 100 ms) after bead contact, WT T cells (Fig. 1A, top) showed increasing Ca^{2+} signals, starting with single local Ca^{2+} microdomains at the bead contact site and resulting in Ca^{2+} events spreading through the whole cell after 15 s. In contrast, T cells from $\text{P2rx4}^{-/-}$ and $\text{P2rx7}^{-/-}$ mice (Fig. 1A, middle and bottom) showed decreased Ca^{2+} microdomains directly in the initial period after bead contact. Ca^{2+} microdomains in the first 15 s occurred in 82% of the WT cells with an amplitude of 329 ± 14 nM and a frequency of approximately 0.29 signals per frame, which is equivalent to 12 signals per second. In $\text{P2rx4}^{-/-}$ and $\text{P2rx7}^{-/-}$ T cells, microdomains only occurred in 55 and 66% of the cells, with a significantly lower frequency of approximately 0.08 signals per frame (3 signals per second) and 0.1 signals per frame (5 signals per second; Fig. 1B). Moreover, the Ca^{2+} signals from $\text{P2rx4}^{-/-}$ T cells had a significantly lower amplitude of 266 ± 7 nM compared to the WT cells. By analyzing every 5 to 25 s after TCR stimulation (Fig. 1C), we observed a significantly decreased number of Ca^{2+} signals for cells from $\text{P2rx4}^{-/-}$ between 5 and 25 s after TCR stimulation, whereas cells from $\text{P2rx7}^{-/-}$ mice only show significantly decreased Ca^{2+} signals between 5 and 10 s compared to WT cells. The number of these highly dynamic Ca^{2+} microdomains directly at the artificial immune synapse was also decreased in the KOs 50 to 100 ms after stimulation compared to the WT (Fig. 1D), revealing an impact of P2X4 and P2X7 on Ca^{2+} microdomains tens of milliseconds after T cell stimulation.

Next, we compared the differences obtained by gene KOs (WT versus $\text{P2rx4}^{-/-}$ or $\text{P2rx7}^{-/-}$) to pharmacological inhibition using the chemical inhibitors for P2X4, 5-BDBD (22, 23) (Fig. S1) and PSB-15417 (24) (Fig. 2), and the inhibitory nanobody against P2X7, 13A7-dim-Alb (19) (Fig. 2). In control cells, Ca^{2+} microdomains occurred again directly (50 to 100 ms) after bead contact, whereas cells with inhibited P2X4 or P2X7 channels just show a few Ca^{2+} signals (Fig. 2A). In the first 15 s upon TCR stimulation, the Ca^{2+} microdomains were significantly decreased for both P2X4- and P2X7-inhibited cells, compared to the respective controls (Fig. 2B). The amplitude of the Ca^{2+} microdomains from cells upon P2X4 inhibition was again significantly reduced (Fig. 2B). The significantly decreased number of Ca^{2+} microdomains by inhibition of P2X4 and P2X7 as well as the decreased amplitude in cells upon P2X4 inhibition are in line with the results from P2X4 and P2X7 KO mice (Fig. 1).

Furthermore, between 2.5 s before and up to 25 s after TCR stimulation, a significant and consistent decrease of Ca^{2+} signals for the cells with inhibition of P2X4 (Fig. 2C, left) and P2X7 (Fig. 2C, right) was observed.

To analyze Ca^{2+} entry at the artificial immune synapse, we further compared Ca^{2+} microdomains in the outer sublayer of the cells at the contact site with the stimulating beads. The number of signals upon P2X4 and P2X7 inhibition was significantly reduced after TCR/CD3 stimulation compared to controls (Fig. 2D). Our results of P2X4 inhibition by PSB-15417 were confirmed with a second inhibitor for this channel, 5-BDBD (Fig. S1). Here, we also observed significantly reduced Ca^{2+} signals in the first 15 s after TCR/CD3 stimulation (Fig. S1B) as well as directly after stimulation at the artificial immune synapse (Fig. S1D). These results substantiate that initial Ca^{2+} entry events were driven by P2X4 and P2X7 channels, leading to the question of interaction of the two channels during this initial phase. P2X4 and P2X7 show the highest sequence similarity compared to other P2X family members, and the P2rx4 gene is located downstream of the P2rx7 gene on the same chromosome (25, 26). Moreover, homotrimers of P2X7 were already coimmunoprecipitated with P2X4 in macrophages, and Boumechache and colleagues (27) suggested an interaction of the channels inside the receptor complexes. To analyze colocalization during the formation of initial Ca^{2+} signals at the plasma membrane, superresolution imaging with optical reassignment (SoRa) was performed using directly conjugated nanobodies with the fluorophores CF568 and A647 against P2X4 and P2X7. Colocalization of the proteins was analyzed only at the plasma membrane of T cells to study the impact of interaction of P2X4 and P2X7 on Ca^{2+} influx (Fig. S2A). During the basal state without stimulation, P2X4 and P2X7 proteins located at the plasma membrane show a slight colocalization of about 11%, and after a short (10-s) activation with soluble anti-CD3, colocalization increased to 15% (Fig. S2B). In the first 10 s after stimulation of the cells, no significant increase in colocalization was observed, but after a longer activation time of 5 min, a significantly increased colocalization of P2X4 and P2X7 was observed (Fig. S2B). These results indicate the interaction of P2X4 and P2X7 during global Ca^{2+} events, but for the generation of the initial Ca^{2+} microdomains, an extensive interaction of P2X4 and P2X7 seems not to be necessary.

Next, we analyze downstream signaling in $\text{P2rx4}^{-/-}$ or $\text{P2rx7}^{-/-}$ CD4^+ T cells, as it was reported that CD4^+ T cells from mice showed decreased migration upon inhibition of P2X4 and, to a lesser extent, P2X7 and P2X1 channels (20). Accordingly, we observed a significantly decreased and delayed global Ca^{2+} response after T cell stimulation with soluble anti-CD3 in $\text{P2rx4}^{-/-}$ and $\text{P2rx7}^{-/-}$ compared to CD4^+ WT cells (Fig. S3, A to C). This further correlates with decreased expression of immediate early gene *Nur77* after 18 hours for which the expression level closely reflects the strength of TCR stimulation (28) and decreased proliferation of CD4^+ T cells for $\text{P2rx7}^{-/-}$; however, expression of activation marker *CD69* was not affected (Fig. S3, D to H).

Immediate ATP release following TCR stimulation activates P2X4 and P2X7

P2X4 and P2X7 are activated by extracellular ATP binding to the channels, resulting in Ca^{2+} influx into T cell (16, 17, 29). Do we observe the same effects as above in Figs. 1 and 2 by removing the P2X4 and P2X7 channel activator, the extracellular ATP? To address this

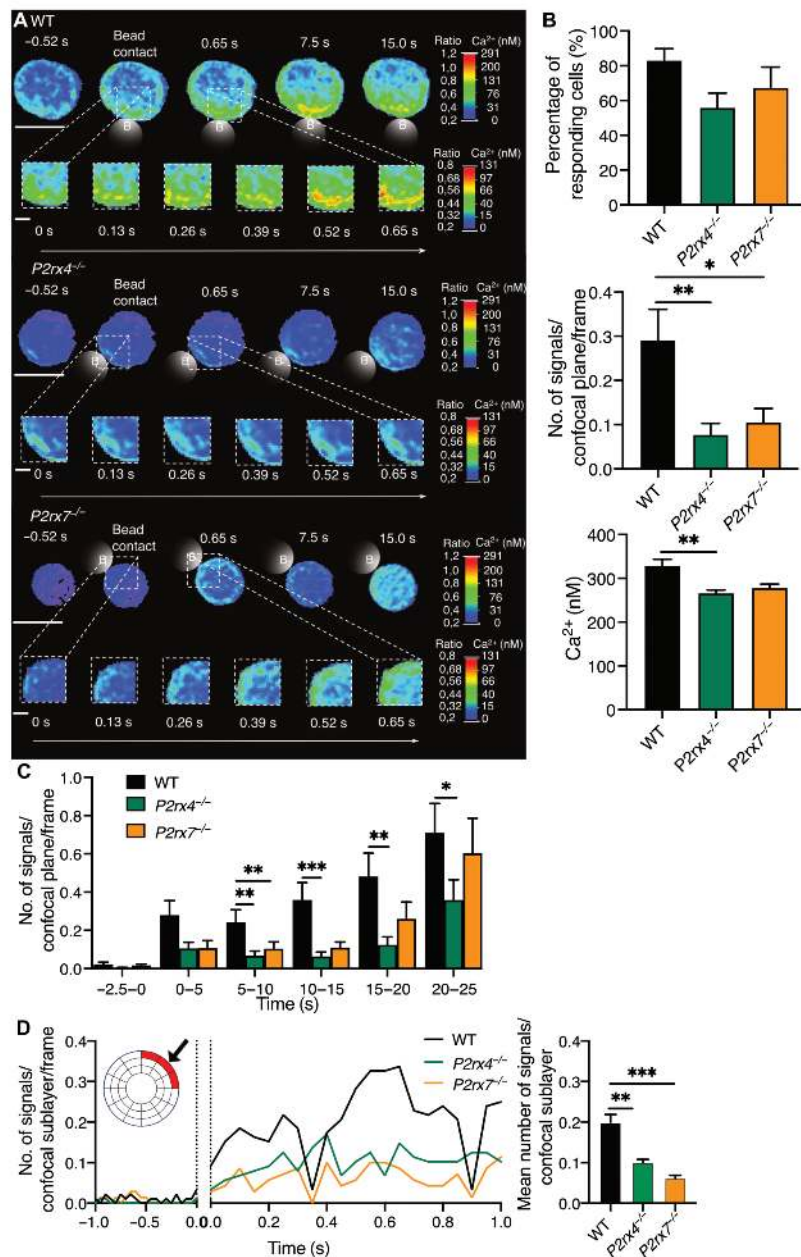


Fig. 1. Decreased Ca^{2+} microdomains in T cells from $\text{P2rx4}^{-/-}$ and $\text{P2rx7}^{-/-}$ KO mice. Ca^{2+} imaging of CD4^{+} T cells of WT or $\text{P2rx4}^{-/-}$ and $\text{P2rx7}^{-/-}$ mice. Cells were stimulated with anti-CD3/anti-CD28-coated beads. A minimum of 10 different mice were used. (B to D) Data are means \pm SEM; WT, $n=46$ cells; $\text{P2rx4}^{-/-}$, $n=47$ cells; $\text{P2rx7}^{-/-}$, $n=39$ cells. Statistical analysis by Kruskal-Wallis test. (A) Representative cells of WT or $\text{P2rx4}^{-/-}$ and $\text{P2rx7}^{-/-}$ were shown for 0.52 s before and up to 15 s after stimulation with anti-CD3/anti-CD28-coated beads (scale bar, 5 mm) as well as for 0 to 0.65 s in 0.13-s steps zoomed into the region of bead contact (scale bar, 1 mm). (B) Quantification of the first 15 s after bead contact for CD4^{+} T cells of WT or $\text{P2rx4}^{-/-}$ and $\text{P2rx7}^{-/-}$ mice. The percentage of responding cells, the number of Ca^{2+} microdomains per frame for whole cells (confocal plane), and the average Ca^{2+} concentration of these signals are shown. (C) Quantification of the number of Ca^{2+} microdomains per frame for the period 2.5 to 0 s before and every 5 s after bead contact up to 25 s after bead contact. (D) Analysis of the Ca^{2+} microdomains in the first second before and after TCR stimulation for the sublayers at the contact site (as indicated in red) (left). Quantification of the signals in the first second after bead contact (right). * $P < 0.05$, ** $P < 0.005$, *** $P < 0.001$.

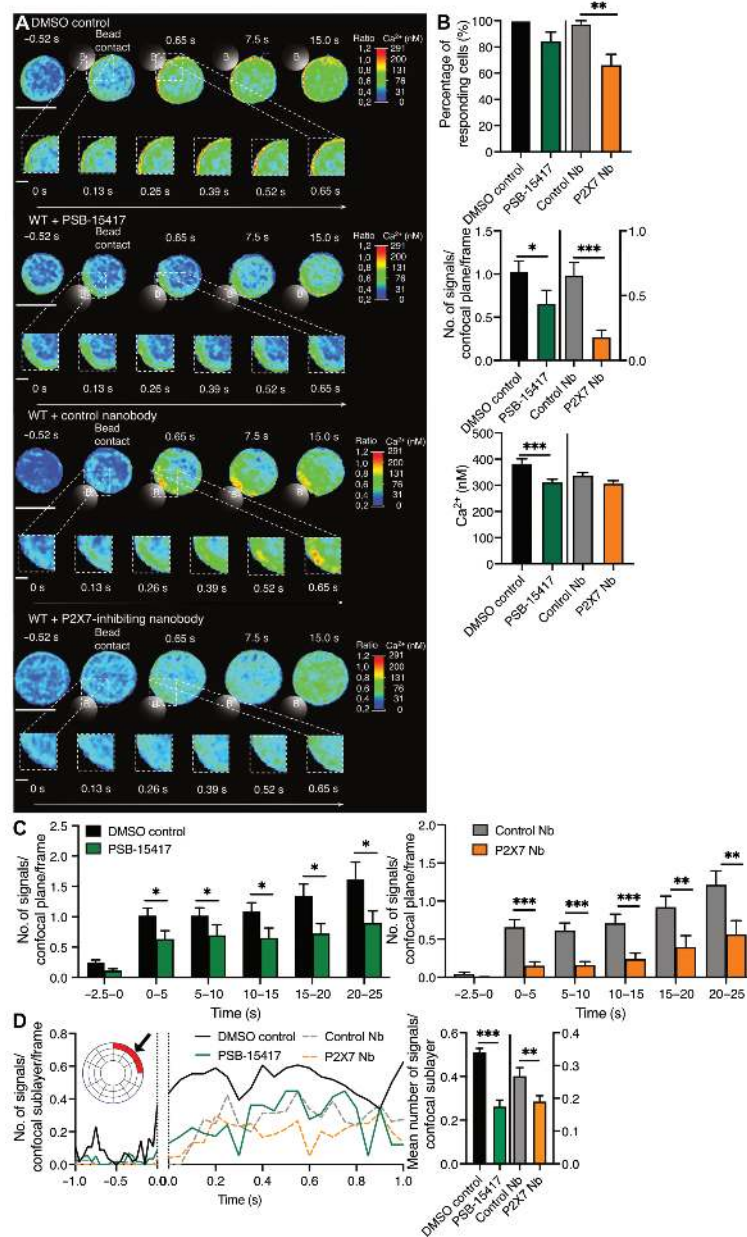


Fig. 2. Reduced Ca²⁺ microdomains in T cells with directly inhibited P2X4 and P2X7 channels. Ca²⁺ imaging of CD4⁺ T cells of WT mice incubated with or without PSB-15417 (1 mM) for the inhibition of P2X4 or inhibiting nanobody (P2X7-Nb) 13A7-dim-Alb (1 mg/ml) for the inhibition of P2X7. A dimethyl sulfoxide (DMSO) control (0.01%) or an irrelevant nanobody (Control Nb; dummy-dim-Alb, 1 mg/ml) was used. Cells were stimulated with anti-CD3/anti-CD28-coated beads. A minimum of five different mice were used. (B to D) Data are means \pm SEM; DMSO control, $n=28$ cells; control nanobody, $n=40$; cells treated with PSB-15417, $n=29$ cells; cells treated with the P2X7-inhibiting nanobody, $n=30$ cells. Statistical analysis by an unpaired two-tailed Mann-Whitney test. (A), inhibited P2X4 and P2X7 channels were shown for 0.52 s before and up to 15 s after stimulation with anti-CD3/anti-CD28-coated beads (scale bar, 5 μ m) as well as for 0 to 0.65 s in 0.13-s steps zoomed into the region of bead contact (scale bar, 1 μ m). (B) Quantification of the first 15 s after bead contact for CD4⁺ T cells of controls or inhibited P2X4 and P2X7. (C) Quantification of the number of Ca²⁺ microdomains per frame for the period 2.5 to 0 s before and every 5 s after bead contact up to 25 s after bead contact. DMSO control and cells treated with PSB-15417 were compared (left), as well as the control Nb with the P2X7-Nb (right). (D) Analysis of the Ca²⁺ microdomains in the first second before and after TCR stimulation for the sublayers at the contact site (as indicated in red) (left). Quantification of the signals in the first second after bead contact (right). * $P < 0.05$, ** $P < 0.005$, *** $P < 0.001$.

SCIENCE ADVANCES | RESEARCH ARTICLE

question, we added apyrase, which hydrolyzes tri- and diphosphate groups of nucleotides (30, 31). Three minutes before Ca^{2+} imaging, WT CD4^+ T cells were incubated with apyrase (10 U/ml). After 1 min of measurement, we stimulated the cells with anti-CD3/anti-CD28-coated beads. WT cells without apyrase incubation showed local Ca^{2+} microdomains increasing more and more after 15 s after bead contact through the cell (Fig. 3A, top). In comparison, cells treated with apyrase showed decreased local Ca^{2+} microdomains (Fig. 3A, bottom). In the first 15 s after activation in cells treated with apyrase, microdomains occurred with a significantly decreased frequency compared to the WT (WT, approximately 0.97 signals per frame; apyrase, approximately 0.25 signals per frame; Fig. 3B). In addition, investigating 5-s periods after TCR/CD3 stimulation also significantly reduced Ca^{2+} signals in cells treated with apyrase between 0 and 25 s compared to WT T cells not treated with apyrase that were observed (Fig. 3C). We conclude that the missing extracellular ATP because of degradation by apyrase (Fig. 3) resulted in decreased numbers of initial Ca^{2+} microdomains. As control, the same experiment was carried out using apyrase that was inactivated by boiling for 30 min (fig. S3). T cells incubated with boiled apyrase did not show any altered Ca^{2+} response (fig. S4). These results suggest a very fast release of ATP into the extracellular space. In addition, directly at the artificial immune synapse, we observed a reduced number of Ca^{2+} microdomains tens of milliseconds after stimulation in cells incubated with apyrase (Fig. 3D). Thus, ATP seems to be released immediately after stimulation of T cells, promoting the activation of the purinergic channels P2X4 and P2X7 to generate Ca^{2+} microdomains during the initial phase of Ca^{2+} signaling.

To further understand the mechanism of ATP release, we started to treat WT CD4^+ T cells with a mimetic inhibitor peptide for PANX1, termed $^{10}\text{panx1}$. PANX1 is part of a family of glycoproteins, consisting of three family members PANX1 to PANX3 (32), expressed in CD4^+ T cells (33) acting as the main ATP-releasing channel (34, 35). A typical T cell treated with the PANX1 inhibitor showed less Ca^{2+} signals after bead contact than the WT cell in the first 0.65 s and at the later time point of 15 s after T cell stimulation (Fig. 4A, top). Zoomed into the artificial immune synapse seconds after stimulation, only very few signals were detected for cells treated with $^{10}\text{panx1}$ (Fig. 4A, bottom). Quantifying the first 15 s after bead contact, Ca^{2+} microdomains were significantly reduced in cells treated with $^{10}\text{panx1}$ compared to WT T cells (Fig. 4B). To compare the temporal role of ATP release and the activation of the P2X channels in relation to the formation of Ca^{2+} microdomains, the number of Ca^{2+} microdomains was again analyzed 2.5 s before and in 5-s steps after T cell stimulation (Fig. 4C). T cells with reduced ATP release due to the inhibition of PANX1 showed significantly decreased Ca^{2+} signals between 0 and 5 s, 5 and 10 s, and 10 and 15 s. The initial Ca^{2+} microdomains at the artificial immune synapse significantly decreased in T cells treated with $^{10}\text{panx1}$ compared to WT T cells already in the first second after bead contact (Fig. 4D). Together, T cells reveal a very fast apyrase- or $^{10}\text{panx1}$ -sensitive ATP release into the extracellular space via PANX1, which is responsible for the activation of P2X4 and P2X7, resulting in the amplification of initial Ca^{2+} microdomains.

Basal ATP release via PANX1 activates P2X4 in unstimulated T cells

To understand the fine-tuning of the Ca^{2+} signals after T cell stimulation, Diercks et al. (9) showed in 2018 that lower and less frequent

Ca^{2+} microdomains in the absence of TCR/CD3 stimulation were already produced by preformed clusters of STIM1 and ORAI1. Therefore, we analyzed these Ca^{2+} microdomains using a high-resolution Ca^{2+} live-cell imaging system (8, 9) in P2X4 and P2X7 KO T cells, in cells treated with the P2X4 inhibitor PSB-15417, or in cells treated with the PANX1 inhibitor $^{10}\text{panx1}$ in the absence of TCR/CD3 stimulation (Fig. 5, A to C). Ca^{2+} microdomains occurred in nonstimulated WT or control T cells already with a lower frequency of approximately 0.07 to 0.2 signals per frame compared to Ca^{2+} microdomains upon TCR/CD3 stimulation with a frequency of approximately 0.3 to 1.0 signals per frame (Figs. 1 to 4B and 5, A to C, number of signals per confocal plane per frame). P2X4 KO cells showed, in the absence of TCR/CD3 stimulation, significantly reduced Ca^{2+} microdomain numbers during a 15-s period without stimulation, whereas P2rx7 $^{-/-}$ cells showed no altered Ca^{2+} response compared to WT cells (Fig. 5A). The amplitude of the signals in P2rx7 $^{-/-}$ T cells did not show differences to WT cells. Ca^{2+} signals were also significantly reduced in cells upon P2X4 inhibition by PSB-15417 (24), but the amplitude of the signals was not altered (Fig. 5B).

These results indicate a role of P2X4, but not of P2X7, in basal Ca^{2+} signaling in T cells in the absence of TCR/CD3 stimulation. Moreover, we demonstrate that the autocrine release of ATP is responsible for activating P2X4 in unstimulated cells by inhibiting the ATP release channel PANX1. In T cells treated with $^{10}\text{panx1}$, the number and amplitude of Ca^{2+} signals were significantly decreased compared to the WT (Fig. 5C).

Together, the results reveal two different mechanisms, one for T cells in the absence of TCR/CD3 stimulation and one for the first seconds in activated T cells (Fig. 6, A and B). In the absence of TCR/CD3 stimulation, lower and less frequent Ca^{2+} microdomains (Figs. 5, A to C, and 6A) were promoted via STIM1 and ORAI1 (9), resulting in the activation of PANX1 (36, 37). Subsequently, a low basal ATP release via PANX1 activates P2X4. After TCR/CD3 activation, increasing ATP release triggers not only P2X4 but now also the less sensitive P2X7 channel (38), leading to the formation of Ca^{2+} microdomains within tens of milliseconds (Figs. 1, 2, and 6B) comparable to our previous model of Ca^{2+} microdomain formation due to RYR1 or ORAI1 and STIM1/2 (8–10).

DISCUSSION

T cell Ca^{2+} microdomains are evoked upon TCR/CD3 stimulation by the production of NAADP that binds to HN1L/JPT2 and targets RYR1, as well as clusters of STIM1/2 with ORAI1 (8–10). Using specific inhibitors and cells from suitable KO mice, we identified two purinergic cation channels, namely, P2X4 and P2X7, which are involved in forming initial Ca^{2+} microdomains in tens of milliseconds after TCR/CD3 stimulation. In a similar setup to our experiments, a reduced number of Ca^{2+} microdomains within the first second after TCR/CD3 stimulation was demonstrated for *Orai1 $^{-/-}$* , *Stim1 $^{-/-}$* , *Stim2 $^{-/-}$* , and *Stim1 $^{-/-}$ /2 $^{-/-}$* as well as *Ryr1 $^{-/-}$* T cells or by NAADP antagonism by BZ194 (9) and recently by knocking out the NAADP receptor HN1L/JPT2 (10). The interaction between STIM1/2 and ORAI1/2/3 and the alteration in Ca^{2+} signaling profiles (9) are predicted to have an important influence on downstream effects, like the activation of the nuclear factor of activated T cells (NFAT) (39). It was shown that the loss of either STIM1 or STIM2 impairs both the formation of Ca^{2+} microdomains (9) and translocation of NFAT1

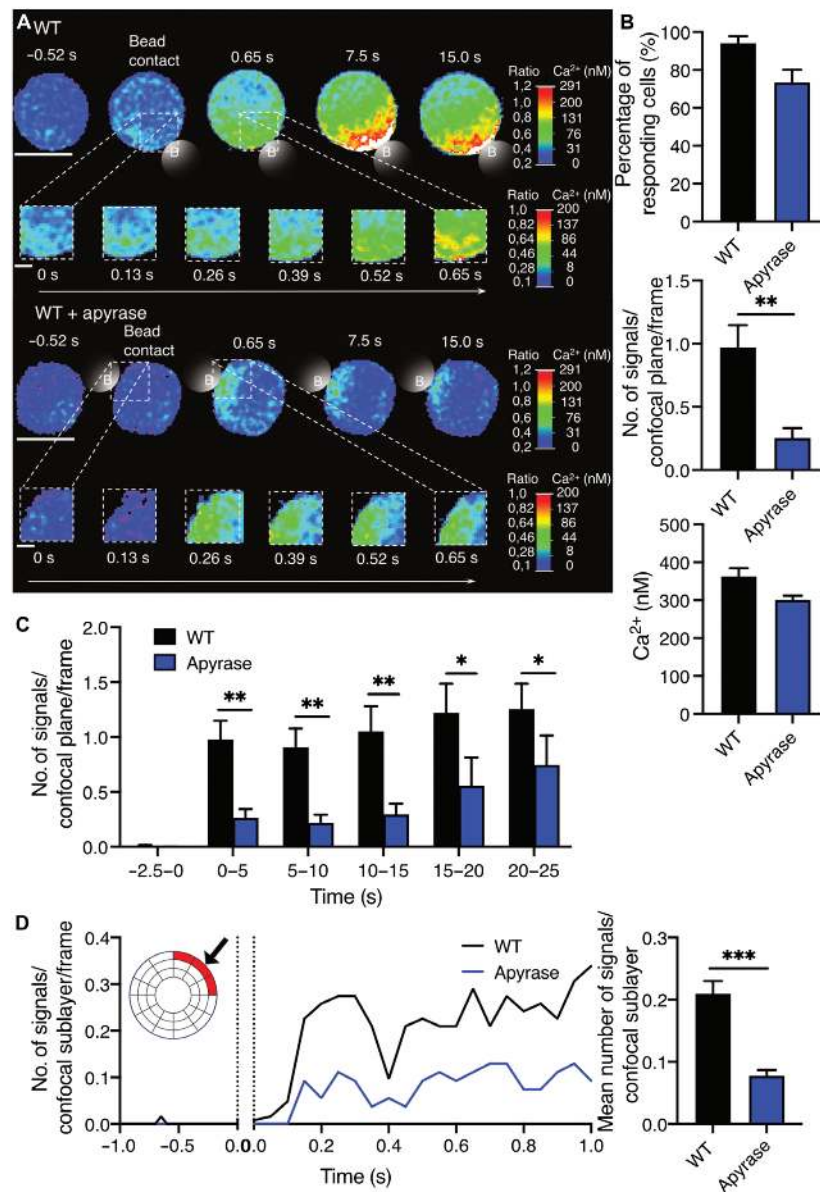


Fig. 3. Removal of extracellular ATP decreases Ca²⁺ microdomains. Ca²⁺ imaging of CD4⁺T cells of WT mice incubated with or without 10 U of apyrase. Cells were stimulated with anti-CD3/anti-CD28-coated beads. A minimum of five different mice were used. (B to D) Data are means \pm SEM; WT, $n = 31$ cells; cells treated with apyrase, $n = 27$ cells. Statistical analysis was done using a nonparametric unpaired two-tailed Mann-Whitney test. (A) Representative cells of WT or cells treated with apyrase were shown for 0.52 s before and up to 15 s after stimulation with anti-CD3/anti-CD28-coated beads (scale bar, 5 μ m) as well as for 0 to 0.65 s in 0.13-s steps zoomed into the region of bead contact (scale bar, 1 μ m). (B) Quantification of the first 15 s after bead contact for CD4⁺T cells of WT or cells treated with apyrase. The percentage of responding cells, the number of Ca²⁺ microdomains per frame for whole cells (confocal plane), and the average Ca²⁺ concentration of these signals are shown. (C) Quantification of the number of Ca²⁺ microdomains per frame for the period 2.5 s before and every 5 s after bead contact up to 25 s after bead contact. (D) Analysis of the Ca²⁺ microdomains in the first second before and after TCR stimulation for the sublayers at the contact site (as indicated in red) (left). Quantification of the signals in the first second after bead contact (right). * $P < 0.05$, ** $P < 0.005$, *** $P < 0.001$.

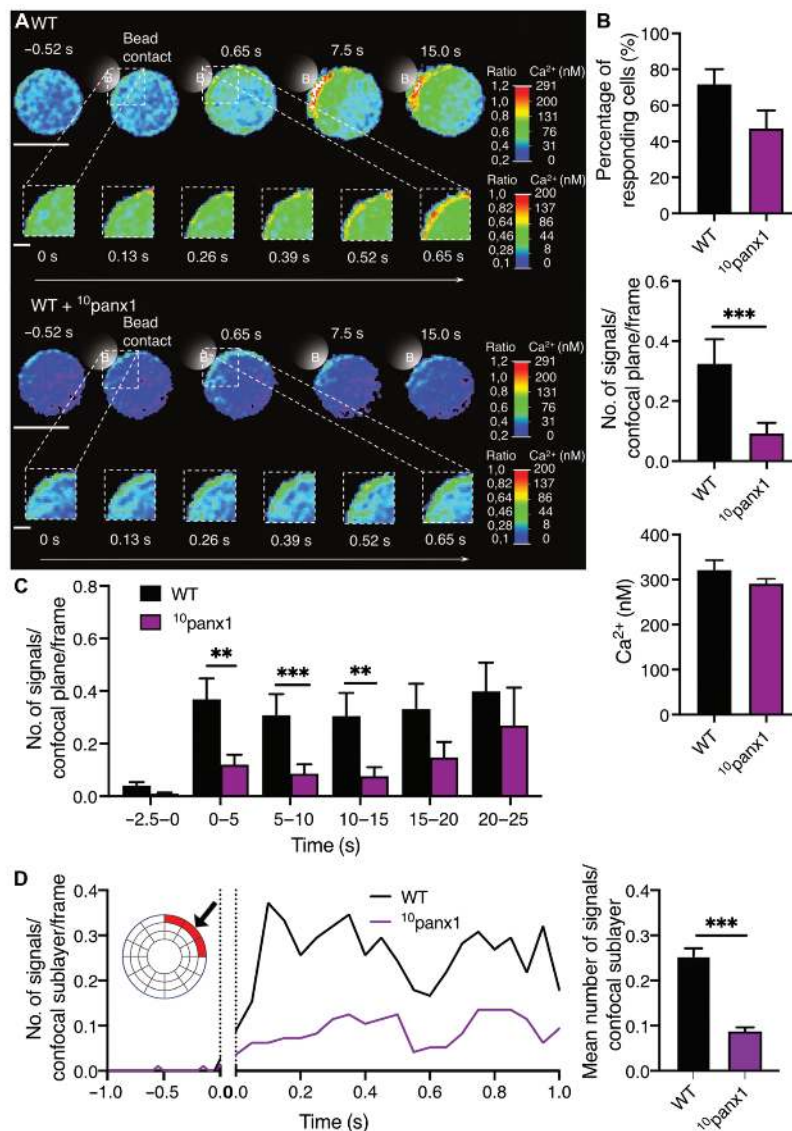


Fig. 4. Inhibition of PANX1 reduces the formation of Ca^{2+} microdomains. Ca^{2+} imaging of CD4^+ T cells of WT mice incubated with or without 200 nM PANX1 inhibitor ¹⁰panx1 20 min before measurements. Cells were stimulated with anti-CD3/anti-CD28-coated beads. A minimum of 10 different mice were used. (B to D) Data are means \pm SEM; WT, $n=39$ cells; cells treated with ¹⁰panx1, $n=48$ cells. Statistical analysis by an unpaired two-tailed Mann-Whitney test. (A) Representative cells of WT or cells treated with ¹⁰panx1 were shown for 0.52 s before and up to 15 s after stimulation with anti-CD3/anti-CD28-coated beads for whole cells (scale bar, 5 mm) as well as for 0 to 0.65 s in 0.13-s steps zoomed into the region of bead contact (scale bar, 1 mm). (B) Quantification of the first 15 s after bead contact for CD4^+ T cells of WT or cells treated with ¹⁰panx1. The percentage of responding cells, the number of Ca^{2+} microdomains per frame for whole cells (confocal plane), and the average Ca^{2+} concentration of these signals are shown. (C) Quantification of the number of Ca^{2+} microdomains per frame for the period 2.5 to 0 s before and every 5 s after bead contact up to 25 s after bead contact. (D) Analysis of the Ca^{2+} microdomains in the first second before and after TCR stimulation for the sublayers at the contact site (as indicated in red) (left). Quantification of the signals in the first second after bead contact (right). *** $P < 0.005$, **** $P < 0.001$.

and NFAT4 (40). Furthermore, antagonizing NAADP by BZ194 results in decreased translocation of NFAT and attenuated clinical scores in rat experimental autoimmune encephalomyelitis (6, 41). NFAT activation is also known to be triggered by purinergic signaling,

and loss of P2X7 resulted in diminished NFAT activation (17, 42, 43). The similarities of downstream effects and alteration in initial Ca^{2+} signaling between the known channels involved in early T cell activation and the two purinergic cation channels P2X4 and P2X7

SCIENCE ADVANCES | RESEARCH ARTICLE

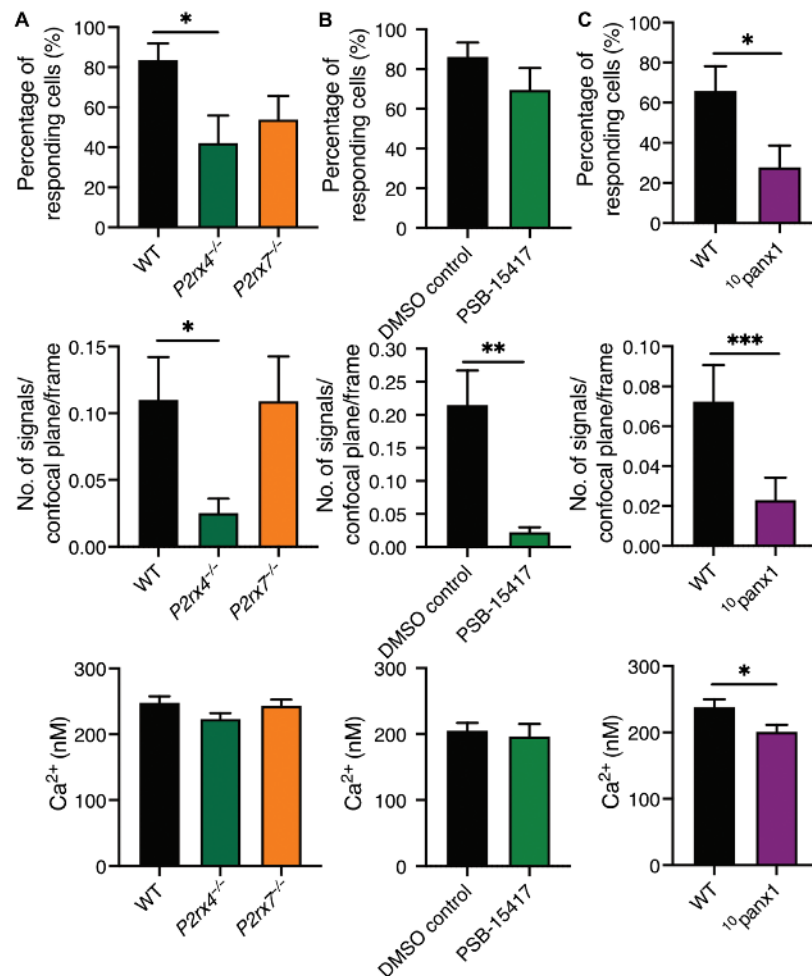


Fig. 5. Basal ATP release via PANX1 activates P2X4, promoting the formation of Ca²⁺ microdomains in the absence of TCR/CD3 stimulation. Ca²⁺ imaging of CD4⁺ T cells of WT mice or P2rx4^{-/-} and P2rx7^{-/-} mice. WT cells were incubated with or without PSB-15417 (1 mM) for the inhibition of P2X4 or 200 mM PANX1 inhibitor 10panx1 20 min before measurements. For the P2X4-inhibiting compound, a DMSO control (0.01%) was used. A minimum of four different mice were used. (A to C) Percentage of responding cells, number of Ca²⁺ microdomains per frame for whole cells (confocal plane), and average Ca²⁺ concentration of these signals. Data are means ± SEM; statistical analysis was done by a Kruskal-Wallis test or an unpaired two-tailed Mann-Whitney test. (A) Quantification of 15 s without stimulation for CD4⁺ T cells of WT or P2rx4^{-/-} and P2rx7^{-/-} mice. WT, n = 44 cells; P2rx4^{-/-}, n = 45 cells; P2rx7^{-/-}, n = 52 cells. (B) Quantification of 15 s without stimulation for CD4⁺ T cells of a DMSO control or cells treated with PSB-15417. DMSO control, n = 35 cells; cells treated with PSB-15417, n = 26 cells. (C) Quantification of 15 s without stimulation for CD4⁺ T cells of WT or cells treated with 10panx1. WT, n = 40 cells; cells treated with 10panx1, n = 47 cells. *P < 0.05, **P < 0.005, ***P < 0.001.

analyzed in this study are notable. Thus, we need to expand our model of initial T cell activation, including the purinergic pathway on a level equivalent to SOCE and NAADP signaling (Fig. 6B). Upon TCR stimulation, not only the NAADP/HN1L-JPT2/RYR1 axis together with SOCE through STIM1/2 and ORAI1 but also P2X4 and P2X7 are involved in the formation of initial Ca²⁺ microdomains.

An interplay of SOCE with purinergic signaling was already found by Woehrlé and colleagues (16) in Jurkat T cells, revealing colocalization of ORAI1 and STIM1 with P2X4 within 30 min of stimulation at the immune synapse. The low colocalization of P2X4 and P2X7 during the formation of initial Ca²⁺ microdomains before and

after T cell stimulation in the current study indicates no interaction of these channels in the basal state of T cells and the first tens of milliseconds after TCR stimulation. In contrast, at later time points, an increased colocalization was observed, consistent with earlier studies (27, 44). It was not confirmed that P2X4 and P2X7 form stable heteromers (45), and a mutual interaction for global Ca²⁺ signals could be assumed because of the impact of both channels on later stages of Ca²⁺ signaling (12–14, 16–18, 46) and the increased colocalization of P2X4 and P2X7 after 5 min of TCR stimulation (fig. S2). In addition, we showed the influence of both channels on the initial steps of T cell activation and Ca²⁺ microdomain formation,

SCIENCE ADVANCES | RESEARCH ARTICLE

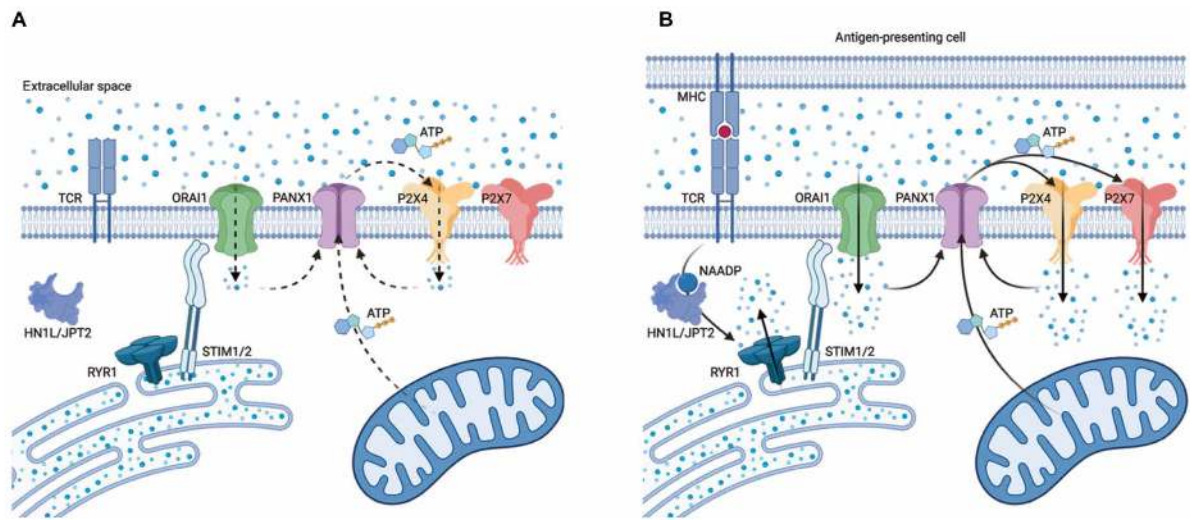


Fig. 6. Summary of Ca^{2+} microdomain formation in preactivated state and milliseconds after T cell activation. Ca^{2+} signaling before and milliseconds after stimulation of the TCR. Blue dots indicate Ca^{2+} signals, and dotted arrows indicate lower amounts of Ca^{2+} or ATP compared to solid arrows. Figures were created with BioRender. (A) A basal activity of T cells is due to preformed clusters of STIM1 and ORAI1 resulting in lower and less frequent Ca^{2+} microdomains. PANX1 is probably activated by these Ca^{2+} microdomains and releases low concentrations of ATP, which activates the sensitive purinergic channel P2X4, which also results in lower and less frequent Ca^{2+} microdomains. (B) Upon TCR stimulation, on the one hand, RYR1 is activated, probably by NAADP bound to HN1L/JPT2, resulting in local and transient Ca^{2+} release. NAADP-evoked Ca^{2+} release through RYR1 contributes directly to highly dynamic Ca^{2+} microdomains and promotes the activation of STIM1/2 and thus SOCE through ORAI1 channels, leading to an amplification of initial Ca^{2+} microdomains. On the other hand, increasing Ca^{2+} concentrations foster ATP release via PANX1 upon TCR stimulation, which activates P2X4 and the less sensitive P2X7 channel in an autocrine manner, and further promote again an amplification of initial Ca^{2+} microdomains.

but only P2X4 seem to be necessary for basal T cell activity without TCR/CD3 stimulation. Together, the results of colocalization and Ca^{2+} imaging indicate different time slots of P2X4 and P2X7 activity. Whereas P2X4 seem to be already active during antigen-presenting cell (APC) recognition and initial T cell activation, P2X7 is activated not until the initial TCR/CD3 stimulation. The different activation periods of P2X4 and P2X7 may influence downstream mechanisms, such as cytokine expression, T cell migration, or proliferation.

Several downstream effects in mice were previously described, for example, by Ulmann and co-workers (47) for P2X4 and Chessell and co-workers (48) for P2X7, who analyzed prostaglandin E_2 and different cytokine levels, like interleukin-6 (IL-6), in $\text{P2rx4}^{-/-}$ or $\text{P2rx7}^{-/-}$ mice after induced inflammatory pain, suggesting a prominent role of both purinergic channels during initial inflammatory signaling pathways. In human Jurkat T cells with silenced P2rx4 or P2rx7 , IL-2 transcription after stimulation with anti-CD3/anti-CD28-coated beads showed a significantly lower response (16, 17). Moreover, inhibition of P2X4 and, to a lesser extent, P2X7 or P2X1 leads to decreased proliferation, and only inhibition of P2X4 reduced the migration of CD4^+ T cells from mice (20). When combining these published and our own data, the following model was generated: Initial Ca^{2+} microdomains of $\text{P2rx4}^{-/-}$ or $\text{P2rx7}^{-/-}$ T cells are decreased in the first tens of milliseconds after T cell stimulation, resulting in a delayed global Ca^{2+} response within minutes and decreased expression of the activation marker Nur77 after 18 hours, apparently translating into reduced proliferation in $\text{P2rx7}^{-/-}$ (fig. S3, G and H) and migration of T cells upon P2X4 inhibition (20).

ATP acts as an essential extracellular signaling molecule, with a crucial role in many cellular processes like cell-to-cell communication,

inducing apoptosis, inflammatory reactions, or tumor growth (49–53). For example, human CD4^+ T cells incubated with 250 nM ATP showed increased secretion of cytokines like IL-2 (52). Our study suggests that ATP release through PANX1 activates P2X4 and P2X7 channels in an autocrine fashion (Figs. 3 and 4), consistent with earlier investigations (16, 46, 54, 55). Hence, removal of extracellular ATP or inhibition of ATP release significantly decreased initial Ca^{2+} microdomains that were observed in tens of milliseconds after TCR/CD3 stimulation (Figs. 3D and 4D), revealing a very fast release of ATP and activation of the two P2X channels. Mitochondrial ATP production and release were also shown for this early time period after T cell stimulation (18), once more connecting Ca^{2+} signaling to purinergic signaling, whereby ATP production in the mitochondria depends on initial Ca^{2+} signaling in T cells (56, 57).

More insights into the kinetics of this complex process were obtained by analyzing Ca^{2+} microdomains in T cells in the absence of TCR/CD3 stimulation. The fast release of ATP can be explained by the basal activity of PANX1 activating P2X4 to promote Ca^{2+} microdomains (Fig. 5C). After TCR/CD3 stimulation, the ATP release seems to be fostered to fully activate P2X4 and the less sensitive P2X7 channel (38) to promote Ca^{2+} microdomains. A basal T cell activity was also shown by preclustered STIM1 and ORAI1, promoting Ca^{2+} microdomains with lower amplitude and frequency already before T cell stimulation (9). We are now able to show the involvement of basal ATP release because of PANX1, resulting in P2X4 activation and the formation of less frequent Ca^{2+} microdomains in unstimulated T cells (Fig. 5, A to C). A basal mitochondrial ATP production in unstimulated cells claimed by Ledderose and colleagues (58) supports our findings of basal ATP release via PANX1

SCIENCE ADVANCES | RESEARCH ARTICLE

and preactivation of P2X4. Moreover, another purinergic channel, P2X1, was recently implicated in this basal phase of CD4⁺ T cell function, being activated by lower ATP concentrations than P2X4 or P2X7 (58). In unstimulated Jurkat T cells, P2X1 and P2X7 act on the activity of mitochondria to produce ATP, revealing a positive feedback loop of purinergic signaling during basal T cell activity (59). The importance of the precisely regulated ATP homeostasis elucidated in cancer cells. Here, the fine-tuning of extracellular ATP concentrations through the purinergic axis of P2X4, P2X7, and PANX1 can decide between a pathway of survival and tumor growth and a P2X7-mediated cell death (59–61). Different ATP concentrations induce different cellular responses. While ATP in the lower nanomolar range (1 to 50 nM) does not alter either proliferation or cell death of activated conventional CD4⁺ T cells and regulatory T cells, intermediate concentrations of ATP (250 nM) result in the activation of conventional CD4⁺ T cells. High concentrations (1 mM) of ATP decrease expression of CD54, CD49d, and CD25 during activation of conventional CD4⁺ T cells but enhance proliferation, adhesion capacity, and migration of regulatory T cells (52). A low permanent ATP release in unstimulated T cells and the formation of Ca²⁺ microdomains might be necessary, or at least supportive, for a fast immune response and APC recognition. To this end, the interaction of purinergic and Ca²⁺ signaling in T cells not stimulated via the TCR/CD3 complex might be an early step of the immune response to be targeted for development of therapeutic interventions. One issue needs to be addressed at this point: There is a huge difference in the sensitivity to ATP concentrations in humans and mice. Cell death is induced in mice by ATP concentrations in the micromolar range, whereas in humans millimolar concentrations are needed (62). One possible explanation might be the missing P2Y11 channel in mice (63). P2Y11 inhibits the P2X7-dependent pore formation and, to this end, P2X7-mediated cell death, but not Ca²⁺ signaling (64). Interaction between P2X and P2Y receptors seem to be adjustable key in ATP balance; P2X1 activity, for example, was shown to be potentiated by coexpression with P2Y1 and P2Y2 (65). P2X and P2Y interactions during Ca²⁺ signaling and microdomain formation require further investigations, and the difference between human and mouse channel expression needs to be kept in mind.

In conclusion, we identify a previously unknown function of P2X4 that is required for the formation of Ca²⁺ microdomains in the absence of TCR/CD3 stimulation, probably via a low basal ATP release via PANX1 (Fig. 6A). Moreover, we show that both P2X4 and P2X7 have a central role in initial Ca²⁺ microdomain formation (Fig. 6B) already in tens of milliseconds after T cell stimulation, because these Ca²⁺ microdomains were blocked by hydrolyzing extracellular ATP or blocking PANX1. There are several mechanisms of PANX1 activation (35), but how PANX1 is activated during basal T cell activity is still unclear and needs to be addressed in further investigations. It was recently described that PANX1 is activated by increasing Ca²⁺ concentrations (36, 37). To this end, the activation of PANX1 in the absence of TCR/CD3 stimulation might be due to preclustered STIM1 and ORAI1 promoting Ca²⁺ microdomains (9).

MATERIALS AND METHODS**Study design**

The aim of the study was to analyze the influence of purinergic signaling on the formation of Ca²⁺ microdomains in T cells. Primary murine CD4⁺ T cells were used, and Ca²⁺ imaging was done in cells

with pharmacological or genetic inhibition of P2X4, P2X7, or PANX1 channels. Ca²⁺ microdomain acquisition and detection was performed as previously described (66). The Ca²⁺ microdomain detection threshold for microdomains after activation was set to 112 nM and for microdomains without TCR/CD3 stimulation to 90 nM Ca²⁺. T cells with global and not spatiotemporally restricted Ca²⁺ amplitudes above the threshold of 90 nM were considered as preactivated and not included in this study. Colocalization of P2X4 and P2X7 before and after T cell activation was analyzed using SoRa. Downstream effects were analyzed in WT and genetically inhibited P2X4 and P2X7 CD4⁺ T cells using flow cytometry. All Ca²⁺ imaging experiments were done three or more times to achieve cell numbers of a minimum of 20. All other experiments were done three times.

Reagents

The Ca²⁺ indicators Fluo4-AM and FuraRed-AM were obtained from Life Technologies. They were dissolved in dimethyl sulfoxide (DMSO), and aliquots were stored at –20°C until measurements. The monoclonal antibodies (mAbs) anti-mouse CD3 and anti-mouse CD28 were obtained from BD Biosciences. The inhibiting compound 5-BDBD was purchased from Tocris; PSB-15417 was provided by C. Müller (Department of Pharmacy, University of Bonn); and the P2X7-inhibiting nanobody 13A7-dim-Alb and the control nanobody dummy-dim-Alb (19) as well as directly conjugated nanobodies against P2X4 (dimer +CF568) and P2X7 (dimer +A647) were provided by F. Koch-Nolte (Department of Immunology, University Medical Centre Hamburg Eppendorf). All other reagents were ordered from Sigma-Aldrich.

Animal models

P2rx4^{–/–} (P2rx4^{tm1Rass}; MGI (Mouse Genome Informatics): 3665297) and P2rx7^{–/–} mice (P2rx7^{tm1Gab}; MGI: 2386080) were backcrossed for 13 generations onto the BALB/c background and were used for experiments along with WT BALB/c mice. All mice were bred at the animal facility of the University Medical Center (UKE). All experiments involving tissue derived from animals were performed with the approval of the responsible regulatory committee (Hamburger Behörde für Gesundheit und Verbraucherschutz, Veterinärwesen/Lebensmittelsicherheit, ORG 941).

Isolation of primary T cells

T cells were isolated from freshly dissected spleens and lymph nodes of WT or KO mice on a BALB/c background. The spleens and lymph nodes were ground through a cell strainer (Ø 40 mm) using the upturned plunger of a syringe in 30 ml of RPMI 1640 containing 25 mM Hepes and GlutaMAX-1 (Gibco, Life Technologies), adding penicillin and streptomycin (100 U/ml) and 7.5% (v/v) newborn calf serum (Biochrom, Merck Millipore). Cell suspension was centrifuged (1200 rpm, 5 min, 4°C), and the cell pellet was dissolved in 5 ml of ammonium-chloride-potassium buffer [4.3 g of ammonium chloride, 0.5 g of KHCO₃, and 0.0186 g of Na₂-EDTA in 400 ml of H₂O (pH 7.2 to 7.4)] for 3 to 5 min for lysis of the erythrocytes. After incubation, the lysis was stopped by adding 25 ml of RPMI medium and by centrifuging at 1200 rpm, 5 min, and 4°C. The supernatant was discarded, and cell pellet was dissolved in 2 ml of Dulbecco's phosphate-buffered saline (DPBS) without CaCl₂ and MgCl₂ (Gibco, Life Technologies). CD4⁺ T cells were isolated using a negative selection kit according to the manufacturer's protocol (EasySep Mouse CD4⁺ T Cell Enrichment Kit, STEMCELL

SCIENCE ADVANCES | RESEARCH ARTICLE

Technologies Inc.). The purity of cells was analyzed by fluorescence-activated cell sorting (FACS) and was up to 97 to 98%.

Local Ca^{2+} imaging in primary T cells and Ca^{2+} microdomain detection

Freshly isolated CD4^+ T cells from WT or $\text{P2rx4}^{-/-}$ or $\text{P2rx7}^{-/-}$ mice were loaded in RPMI (see above) with the two Ca^{2+} dyes Fluo4 (10 mM) and FuraRed (20 mM), and Ca^{2+} imaging with a frame rate of 40 frames/s was done as described in detail by Diercks et al. (66). Cells were resuspended in Ca^{2+} buffer [140 mM NaCl, 5 mM KCl, 1 mM MgSO_4 , 1 mM CaCl_2 , 20 mM Hepes (pH 7.4), 1 mM NaH_2PO_4 , and 5 mM glucose] and imaged for 3 min on coverslips coated with 5 μl of bovine serum albumin (BSA) (5 mg/ml) and 5 μl of poly-L-lysine (0.1 mg/ml). After the first minute, they were either stimulated or not stimulated with anti-CD3/anti-CD28-coated beads adding 10 μl of the bead solution with a pipette, and Ca^{2+} changes were recorded for the last 2 min of measurements. During the postprocessing, all T cells were normalized on bead contact site and time.

For direct inhibition of P2X4 and P2X7, cells were incubated for 30 min before the Ca^{2+} measurements with a P2X4-inhibiting compound (5-BDBD, 10 mM) as well as PSB-15417 (1 mM) or a P2X7-inhibiting nanobody (13A7-dim-Alb, 1 mg/ml). The compounds were resolved in DMSO; to this end, a DMSO control (0.01 and 0.1%) for the measurements was used, as well as a nanobody control (dummy-dim-Alb; 1 mg/ml) for the measurements with the inhibiting nanobody. The addition of apyrase (10 U/ml) 3 min before measurements was used to remove the extracellular ATP. Moreover, a negative control was produced by heating the apyrase up for 30 min at 70°C. To inhibit the PANX1 hemichannel, cells were incubated with the PANX1 mimetic peptide $^{10}\text{panx1}(67)$ at a concentration of 200 nM for 20 min.

Ca^{2+} microdomains, defined as small, compact connected sets of pixels with high $[\text{Ca}^{2+}]_i$ values, were detected with a threshold of 112 nM in cells activated with anti-CD3/anti-CD28-coated beads or without stimulation with a threshold of 90 nM in an automated MATLAB script (66). To analyze Ca^{2+} microdomains developing close to the bead contact (as shown in Figs. 1D to 4D), the cell shapes were approximated to be circular, all cells of the considered group/condition rotated such that the bead contact sites agreed for the cells, and the cell areas were subdivided in a dartboard-like manner detailed in (66). Ca^{2+} microdomain statistics (number of microdomains, associated Ca^{2+} concentration) were then computed for the different dartboard compartments and specified time windows. For Figs. 1D to 4D, the three outer compartments at the bead contact site that are highlighted in red in figures were analyzed.

Colocalization analysis with SoRa

Primary CD4^+ T cells from BALB/c mice were left unstimulated or stimulated with soluble anti-CD3 (0.5 mg/ml) for 10 s or 5 min and were seeded on slides coated with poly-L-lysine (0.1 mg/ml). The cells were fixed with 4% (w/v) paraformaldehyde (Alfa Aesar) for 15 min and permeabilized with 0.05% (v/v) saponin (Fluka) again for 15 min. They were incubated overnight at 4°C with 10% (v/v) of fetal bovine serum to block unspecific binding sites. Cells were stained with directly conjugated nanobodies against P2X4 (dimer + CF568; 1:50) and P2X7 (dimer + A647; 1:50) (provided by T. Stähler, Department of Immunology, University Medical Centre Hamburg Eppendorf) for 1 hour. Slides with fixed cells were mounted on coverslips upside down with Abberior Mount solid at 4°C overnight. Image acquisition

was done using a superresolution spinning disk microscope (Visitron), a CSU-W1 SoRa optic (2.8 \times ; Yokogawa), a $\times 100$ magnification objective (Zeiss), and a scientific Complementary metal-oxide-semiconductor camera (Orca-Flash 4.0, C13440-20CU, Hamamatsu). The following lasers and filters were used: aP2X4-CF568: excitation, 561 nm laser; emission filter, 609/54 nm; aP2X7-A647: excitation, 640 nm laser; emission, 700/75 nm. Image deconvolution was based on the principle of Arigovindan et al. (68) [reimplemented and adapted by Woelk et al. (69)]. For colocalization analysis, the trainable weka (Waikato environment for knowledge analysis) segmentation plugin and watershed segmentation were used in Fiji (version 2.1.0/1.53c) to improve the separation of the single proteins, which were detected. Only proteins near the plasma membrane were analyzed for colocalization. For the calculation and quantification of the colocalization of P2X4 and P2X7, a MATLAB script, based on the published study by Nauth et al. (70), was used.

Global Ca^{2+} imaging in primary T cells

Freshly isolated CD4^+ T cells from WT, $\text{P2rx4}^{-/-}$, or $\text{P2rx7}^{-/-}$ mice were loaded in 500 μl of RPMI (see above) with 4 mM Fura2-AM for 35 min at 37°C. After 20 min of incubation, 2 ml of medium was added. After Fura2 loading, cells were washed with Ca^{2+} buffer [140 mM NaCl, 5 mM KCl, 1 mM MgSO_4 , 1 mM CaCl_2 , 1 mM NaH_2PO_4 , 20 mM Hepes, and 5.5 mM glucose (pH 7.4) (NaOH, sterile-filtered)] (10). Ca^{2+} imaging was performed using a Leica IRBE microscope equipped with a 40-fold objective and an electron-multiplying charge-coupled device camera (C9100-13, Hamamatsu). As a light source, a Sutter DG-4 High Speed Wavelength Switcher with the following filter set was used: excitation, hard-coated (HC) 340/26 nm and HC 387/11 nm; beam splitter, 400 DCLP; emission, 510/84 nm (10). Cells were imaged with an exposure time of 20 ms for 340 and 380 nm for 10 min on slides coated with 5 μl of BSA (5 mg/ml) and 5 μl of poly-L-lysine (0.1 mg/ml) and stimulated with 10 μl of soluble anti-CD3 after 2 min. Image acquisition was done in 16-bit mode with Volocity software (PerkinElmer), and postprocessing like background correction, splitting of the fluorescence channels, and selection of the regions of interest was performed with Fiji software (version 2.1.0/1.53c).

Flow cytometry

Spleen cells were isolated by pressing the organ successively through 70- and 40- μm cell strainers. Erythrocytes were depleted with lysis buffer [155 mM NH_4Cl , 10 mM KHCO_3 , 10 mM EDTA (pH 7.2)]. Cells were incubated in 500 μl of Iscove's modified Dulbecco's medium (IMDM) supplemented with fetal calf serum, glutamine, gentamicin, and 2-mercaptoethanol. Cells were stimulated for 18 hours with anti-CD3e mAb (1 mg/ml; clone 145-2C11, BioLegend, San Diego, CA) and anti-CD28 mAb (1 mg/ml; clone 37.5.1, BioLegend). For extracellular antibody staining, cells were incubated in PBS with 1% rat serum and anti-Fc receptor mAb (10 mg/ml; clone 2.4G2, BioXCell, West Lebanon, NH). Cells were incubated with a fixable dead cell stain (Alexa Flour 750 carboxylic acid, succinimidyl ester, Invitrogen, Eugene, OR), AF700-conjugated anti-CD4 mAb (clone RM4-5, BioLegend), and BV605-conjugated anti-CD69 mAb (clone H1.2F3, BioLegend) for 20 min on ice. Intracellular antibody staining was conducted with the Foxp3/Transcription Factor Staining Buffer Set (Invitrogen) according to the manufacturer's protocol. Cells were stained with phycoerythrin-conjugated anti-NUR77 mAb (clone 12.14, Invitrogen). Cells were analyzed using a FACSCelesta flow

SCIENCE ADVANCES | RESEARCH ARTICLE

cytometer (BD Biosciences, Franklin Lakes, NJ) and FlowJo software (Tree Star, Ashland, OR).

For the proliferation assay, spleen cells were incubated for 10 min at room temperature with carboxyfluorescein diacetate succinimidyl ester (CFSE) proliferation dye (5 mM; Invitrogen). The cells were washed twice and then incubated with anti-CD3 ϵ mAb (1 mg/ml; clone 145-2C11, BioLegend) and anti-CD28 mAb (1 mg/ml; clone 37.5.1, BioLegend) in supplemented IMDM. After 3 days, cells were stained with APC-conjugated anti-CD4 mAb (clone RM4-5, eBioscience, San Diego, CA) and a fixable dead cell stain (Alexa Flour 750 carboxylic acid, succinimidyl ester, Invitrogen) and analyzed by FACS.

Statistics

All data are presented as means \pm SEM of independent experiments performed as at least triplicates. Data were analyzed using MATLAB software (MathWorks) and Prism 9 (GraphPad Software). Groups were compared using Mann-Whitney U or Kruskal-Wallis tests or two-way analysis of variance (ANOVA) and Dunnett's multiple comparisons test. A P value of 0.05 was considered as significant.

SUPPLEMENTARY MATERIALS

Supplementary material for this article is available at <https://science.org/doi/10.1126/sciadv.abl9770>

[View/request a protocol for this paper from Bio-protocol.](#)

REFERENCES AND NOTES

- R. Flegert, J. Heeren, F. Koch-Nolte, V. O. Nikolaev, C. Lohr, C. Meier, A. H. Guse, Adenine nucleotides as paracrine mediators and intracellular second messengers in immunity and inflammation. *Biochem. Soc. Trans.* **47**, 329–337 (2019).
- M. Trebak, J. P. Kinet, Calcium signalling in T cells. *Nat. Rev. Immunol.* **19**, 154–169 (2019).
- S. D. Guile, L. Alcaraz, T. N. Birkinshaw, K. C. Bowers, M. R. Ebdon, M. Furber, M. J. Stocks, Antagonists of the P2X₇ receptor. From lead identification to drug development. *J. Med. Chem.* **52**, 3123–3141 (2009).
- E. C. Keystone, M. M. Wang, M. Layton, S. Hollis, I. B. McInnes, Clinical evaluation of the efficacy of the P2X₇ purinergic receptor antagonist AZD9056 on the signs and symptoms of rheumatoid arthritis in patients with active disease despite treatment with methotrexate or sulphasalazine. *Ann. Rheum. Dis.* **71**, 1630–1635 (2012).
- M. Vaeth, J. Yang, M. Yamashita, I. Zee, M. Eckstein, C. Knosp, U. Kaufmann, P. K. Jani, R. S. Lacruz, V. Flockerzi, I. Kacsóvics, M. Prakriya, S. Feske, ORAI2 modulates store-operated calcium entry and T cell-mediated immunity. *Nat. Commun.* **8**, 14714 (2017).
- C. Cordigliere, F. Odoardi, B. Zhang, M. Nebel, N. Kawakami, W. E. F. Klinkert, D. Lodygin, F. Lühder, E. Breunig, D. Schild, V. K. Ulaganathan, K. Dormair, W. Dammernann, B. V. L. Potter, A. H. Guse, A. Flügel, Nicotinic acid adenine dinucleotide phosphate-mediated calcium signalling in effector T cells regulates autoimmunity of the central nervous system. *Brain* **133**, 1930–1943 (2010).
- A. Guse, I. Ernst, R. Flegert, NAADP signaling revisited. *Curr. Top. Med. Chem.* **13**, 2978–2990 (2013).
- I. M. A. Wolf, B. P. Diercks, E. Gattkowski, F. Czarniak, J. Kempfski, R. Wemer, D. Schetelig, H. W. Mittrücker, V. Schumacher, M. Von Osten, D. Lodygin, A. Flügel, R. Flegert, A. H. Guse, Frontrunners of T cell activation: Initial, localized Ca²⁺ signals mediated by NAADP and the type 1 ryanodine receptor. *Sci. Signal.* **8**, ra102 (2015).
- B. P. Diercks, R. Wemer, P. Weidemüller, F. Czarniak, L. Hernandez, C. Lehmann, A. Rosche, A. Krüger, U. Kaufmann, M. Vaeth, A. V. Failla, B. Zobiak, F. I. Kandil, D. Schetelig, A. Ruthenbeck, C. Meier, D. Lodygin, A. Flügel, D. Ren, I. M. A. Wolf, S. Feske, A. H. Guse, ORAI1, STIM1/2, and RYR1 shape subsecond Ca²⁺ microdomains upon T cell activation. *Sci. Signal.* **11**, eaat0358 (2018).
- H. G. Roggenkamp, I. Khansahib, C. L. C. Hernandez, Y. Zhang, D. Lodygin, A. Krüger, F. Gu, F. Möckl, A. Löhndorf, V. Wolters, D. Wolke, A. Rosche, A. Bauche, D. Schetelig, R. Werner, H. Schlüter, A. V. Failla, C. Meier, R. Flegert, T. F. Walseth, A. Flügel, B. P. Diercks, A. H. Guse, HN1L/JPT2: A signaling protein that connects NAADP generation to Ca²⁺ microdomain formation. *Sci. Signal.* **14**, eabd5647 (2021).
- G. S. Gunaratne, E. Brailoiu, S. He, E. M. Untertwald, S. Patel, J. T. Slama, T. F. Walseth, J. S. Marchant, Essential requirement for JPT2 in NAADP-evoked Ca²⁺ signaling. *Sci. Signal.* **14**, eabd5605 (2021).
- U. Schenk, A. M. Westendorf, E. Radaelli, A. Casati, M. Ferro, M. Fumagalli, C. Verderio, J. Buer, E. Scanziani, F. Grassi, Purinergic control of T cell activation by ATP released through pannexin-1 hemichannels. *Sci. Signal.* **1**, ra6 (2008).
- G. Burnstock, J. M. Boeynaems, Purinergic signalling and immune cells. *Purinergic Signal.* **10**, 529–564 (2014).
- V. M. Ruiz-Rodríguez, J. D. Cortés-García, M. de Jesús Briones-Espinoza, E. Rodríguez-Varela, M. Vega-Cárdenas, A. Gómez-Otero, M. H. García-Hernández, D. P. Portales-Pérez, P2X₄ receptor as a modulator in the function of P2X₂ receptor in CD4⁺ T cells from peripheral blood and adipose tissue. *Mol. Immunol.* **112**, 369–377 (2019).
- F. Grassi, The P2X₇ receptor as a regulator of T cell development and function. *Front. Immunol.* **11**, 1179 (2020).
- T. Woehrl, L. Yip, A. El Khal, Y. Sumi, Y. Chen, Y. Yao, P. A. Insel, W. G. Junger, Pannexin-1 hemichannel-mediated ATP release together with P2X₁ and P2X₄ receptors regulate T-cell activation at the immune synapse. *Blood* **116**, 3475–3484 (2010).
- L. Yip, T. Woehrl, R. Coriden, M. Hirsh, Y. Chen, Y. Inoue, V. Ferrari, P. A. Insel, W. G. Junger, Autocrine regulation of T-cell activation by ATP release and P2X₇ receptors. *FASEB J.* **23**, 1685–1693 (2009).
- C. Ledderose, Y. Bao, M. Lidicky, J. Zipperle, L. Li, K. Strasser, N. I. Shapiro, W. G. Junger, Mitochondria are gate-keepers of T cell function by producing the ATP that drives purinergic signaling. *J. Biol. Chem.* **289**, 25936–25945 (2014).
- W. Danquah, M. S. Catherine, B. Rissiek, C. Pinto, S. P. Arnau, M. Amadi, D. Iacenda, J. H. Knop, A. Hammel, P. Bergmann, N. Schwarz, J. Assunção, W. Rothfrier, F. Haag, E. Tolosa, P. Bannas, B. G. Eric, T. Magnus, T. Laeremans, C. Stortelers, F. Koch-Nolte, Nanobodies that block gating of the P2X₇ ion channel ameliorate inflammation. *Sci. Transl. Med.* **8**, 366ra162 (2016).
- C. Ledderose, K. Liu, Y. Kondo, C. J. Slubowski, T. Dertrig, S. Denicoló, M. Arbab, J. Hubner, K. Konrad, M. Fakhari, J. A. Lederer, S. C. Robson, G. A. Visner, W. G. Junger, Purinergic P2X₄ receptors and mitochondrial ATP production regulate T cell migration. *J. Clin. Invest.* **128**, 3583–3594 (2018).
- M. Er-Lukowiak, Y. Duan, F. Rassendren, L. Ulmann, A. Nicke, F. Ufer, M. A. Friese, F. Koch-Nolte, T. Magnus, B. Rissiek, A P2X₇ passenger mutation affects the vitality and function of T cells in congenic mice. *iScience* **23**, 101870 (2020).
- B. Balázs, T. Dankó, G. Kovács, L. Koles, M. A. Hediger, Á. Zsembery, Investigation of the inhibitory effects of the benzodiazepine derivative, 5-BDBD on P2X₄ purinergic receptors by two complementary methods. *Cell. Physiol. Biochem.* **32**, 11–24 (2013).
- C. Coddou, R. Sandoval, M. J. Hevia, S. S. Stojilkovic, Characterization of the antagonist actions of 5-BDBD at the rat P2X₄ receptor. *Neurosci. Lett.* **690**, 219–224 (2019).
- A. Abdelrahman, V. Namasivayam, S. Hinz, A. C. Schiedel, M. Köse, M. Burton, A. El-Tayeb, M. Gillard, J. Bajorath, M. de Ryck, C. E. Müller, Characterization of P2X₄ receptor agonists and antagonists by calcium influx and radioligand binding studies. *Biochem. Pharmacol.* **125**, 41–54 (2017).
- Z. Hou, J. Cao, Comparative study of the P2X₂ gene family in animals and plants. *Purinergic Signal.* **12**, 269–281 (2016).
- R. Kopp, A. Krautloher, A. Ramirez-Fernández, A. Nicke, P2X₇ interactions and signaling—Making head or tail of it. *Front. Mol. Neurosci.* **12**, 183 (2019).
- M. Boumechache, M. Masin, J. M. Edwardson, D. Görecki, R. Murrell-Lagnado, Analysis of assembly and trafficking of native P2X₄ and P2X₇ receptor complexes in rodent immune cells. *J. Biol. Chem.* **284**, 13446–13454 (2009).
- J. F. Ashouri, A. Weiss, Endogenous Nur77 is a specific indicator of antigen receptor signaling in human T and B cells. *J. Immunol.* **198**, 657–668 (2017).
- F. DiVirgilio, P. Chiozzi, D. Ferrari, S. Falzoni, J. M. Sanz, A. Morelli, M. Torboli, G. Bolognesi, O. R. Baricordi, Nucleotide receptors: An emerging family of regulatory molecules in blood cells. *Blood* **97**, 587–600 (2001).
- M. Handa, G. Guidotti, Purification and cloning of a soluble ATP-diphosphohydrolase (Apyrase) from potato tubers (*Solanum tuberosum*). *Biochem. Biophys. Res. Commun.* **218**, 916–923 (1996).
- M. Tsukimoto, A. Tokunaga, H. Harada, S. Kojima, Blockade of murine T cell activation by antagonists of P2Y₆ and P2X₇ receptors. *Biochem. Biophys. Res. Commun.* **384**, 512–518 (2009).
- R. Bruzzone, S. G. Hormuzdi, M. T. Barbe, A. Herb, H. Moryer, Pannexins, a family of gap junction proteins expressed in brain. *Proc. Natl. Acad. Sci. U.S.A.* **100**, 13644–13649 (2003).
- K. F. Shoji, P. J. Sáez, P. A. Harcha, H. L. Aguila, J. C. Sáez, Pannexin1 channels act downstream of P2X₇ receptors in ATP-induced murine T-cell death. *Channels* **8**, 142–156 (2014).
- W. G. Junger, Immune cell regulation by autocrine purinergic signaling. *Nat. Rev. Immunol.* **11**, 201–212 (2011).
- Y. H. Chiu, M. S. Schappe, B. N. Desai, D. A. Bayliss, Revisiting multimodal activation and channel properties of Pannexin 1. *J. Gen. Physiol.* **150**, 19–39 (2018).
- P. Whyte-Fagundes, G. Zoidl, Mechanisms of pannexin1 channel gating and regulation. *Biochim. Biophys. Acta Biomembr.* **1860**, 65–71 (2018).
- K. A. Taylor, J. R. Wright, M. P. Mahaut-Smith, Regulation of Pannexin-1 channel activity. *Biochem. Soc. Trans.* **43**, 502–507 (2015).

SCIENCE ADVANCES | RESEARCH ARTICLE

38. K. Kaczmarek-Hájek, É. Lőrinczi, R. Hausmann, A. Nicke, Molecular and functional properties of P2X receptors—recent progress and persisting challenges. *Purinergic Signal*. **8**, 375–417 (2012).
39. Y. Gwack, S. Feske, S. Srikanth, P. G. Hogan, A. Rao, Signalling to transcription: Store-operated Ca^{2+} entry and NFAT activation in lymphocytes. *Cell Calcium* **42**, 145–156 (2007).
40. S. M. Emrich, R. E. Yoast, P. Xin, J. Sneyd, D. I. Yule, S. M. Emrich, R. E. Yoast, P. Xin, V. Arige, L. E. Wagner, N. Hempel, D. L. Gill, Article. Omnitemporal choreographies of all five STIM / Orai and IP_3 Rs underlie the complexity of mammalian Ca^{2+} signaling. *Cell Reports* **34**, 108760 (2021).
41. W. Dammernann, B. Zhang, M. Nebel, C. Cordiglieri, F. Odoardi, T. Kirchberger, N. Kawakami, J. Dowden, F. Schmid, K. Dommair, M. Hohenegger, A. Flügel, A. H. Guse, B. V. L. Potter, NAADP-mediated Ca^{2+} signaling via type 1 ryanodine receptor in T cells revealed by a synthetic NAADP antagonist. *Proc. Natl. Acad. Sci. U.S.A.* **106**, 10678–10683 (2009).
42. E. Adinolfi, A. L. Giuliani, E. De Marchi, A. Pegoraro, E. Orioli, F. Di Virgilio, The P2X7 receptor: A main player in inflammation. *Biochem. Pharmacol.* **151**, 234–244 (2018).
43. P. Prasai, G. C. Stefanos, W. Becker, Extracellular ATP activates NFAT-dependent gene expression in neuronal PC12 cells via P2X receptors. *BMC Neurosci.* **12**, 90 (2011).
44. C. Guo, M. Masin, O. S. Qureshi, R. D. Murrell-Lagnado, Evidence for functional P2X4/P2X7 heteromeric receptors. *Mol. Pharmacol.* **72**, 1447–1456 (2007).
45. A. Nicke, Homotrimeric complexes are the dominant assembly state of native P2X7 subunits. *Biochem. Biophys. Res. Commun.* **377**, 803–808 (2008).
46. C. M. Wang, C. Ploia, F. Anselmi, A. Sarukhan, A. Viola, Adenosine triphosphate acts as a paracrine signaling molecule to reduce the motility of T cells. *EMBO J.* **33**, 1354–1364 (2014).
47. L. Ulmann, H. Hirbec, F. Rassendren, P2X4 receptors mediate PGE2 release by tissue-resident macrophages and initiate inflammatory pain. *EMBO J.* **29**, 2290–2300 (2010).
48. I. P. Chessell, J. P. Hatcher, C. Bountra, A. D. Michel, J. P. Hughes, P. Green, J. Egerton, M. Murfin, J. Richardson, W. L. Peck, C. B. A. Graham, M. Anna, Y. Yiangou, R. Birch, P. Anand, G. N. Buell, Disruption of the P2X7 purinoreceptor gene abolishes chronic inflammatory and neuropathic pain. *Pain* **114**, 386–396 (2005).
49. M. V. Zamarava, R. Z. Sabirov, E. Maeno, Y. Ando-Akatsuka, S. V. Bessonova, Y. Okada, Cells die with increased cytosolic ATP during apoptosis: A bioluminescence study with intracellular luciferase. *Cell Death Differ.* **12**, 1390–1397 (2005).
50. P. Pellegatti, L. Raffaghello, G. Bianchi, F. Piccardi, V. Pistoia, F. Di Virgilio, Increased level of extracellular ATP at tumor sites: In vivo imaging with plasma membrane luciferase. *PLOS ONE* **3**, e2599 (2008).
51. J. Linden, F. Koch-Nolte, G. Dahl, Purine release, metabolism, and signaling in the inflammatory response. *Annu. Rev. Immunol.* **37**, 325–347 (2019).
52. S. TrabANELLI, D. Očadlíková, S. Gulinielli, A. Curti, V. Salvestrini, R. de Paula Vieira, M. Idzko, F. Di Virgilio, D. Ferrari, R. M. Lemoli, Extracellular ATP exerts opposite effects on activated and regulatory CD4⁺ T cells via purinergic P2 receptor activation. *J. Immunol.* **189**, 1303–1310 (2012).
53. T. M. Chused, S. Apasov, M. Sitkovsky, Murine T lymphocytes modulate activity of an ATP-activated P2Z-type purinoreceptor during differentiation. *J. Immunol.* **157**, 1371–1380 (1996).
54. C. Ledderose, Y. Bao, J. Zhang, W. G. Junger, Novel method for real-time monitoring of ATP release reveals multiple phases of autocrine purinergic signalling during immune cell activation. *Acta Physiol.* **213**, 334–345 (2015).
55. Z. Deng, Z. He, G. Maksae, R. M. Bitter, M. Rau, J. A. J. Fitzpatrick, P. Yuan, Cryo-EM structures of the ATP release channel pannexin 1. *Nat. Struct. Mol. Biol.* **27**, 373–381 (2020).
56. P. S. Brookes, Y. Yoon, J. L. Robotham, M. W. Anders, S. S. Sheu, Calcium, ATP, and ROS: A mitochondrial love-hate triangle. *Am. J. Physiol. Cell Physiol.* **287**, C817–C833 (2004).
57. C. J. Fox, P. S. Hammeman, C. B. Thompson, Fuel feeds function: Energy metabolism and the T-cell response. *Nat. Rev. Immunol.* **5**, 844–852 (2005).
58. C. Ledderose, Y. Bao, S. Ledderose, T. Woehrl, M. Heinisch, L. Yip, J. Zhang, S. C. Robson, N. I. Shapiro, W. G. Junger, Mitochondrial dysfunction, depleted purinergic signaling, and defective T cell vigilance and immune defense. *J. Infect. Dis.* **213**, 456–464 (2016).
59. C. Ledderose, T. Woehrl, S. Ledderose, K. Strasser, R. Seist, Y. Bao, J. Zhang, W. G. Junger, Cutting off the power: Inhibition of leukemia cell growth by pausing basal ATP release and P2X receptor signaling? *Purinergic Signal*. **12**, 439–451 (2016).
60. D. Draganov, S. Gopalakrishna-Pillai, Y. R. Chen, N. Zuckerman, S. Moeller, C. Wang, D. Ann, P. P. Lee, Modulation of P2X4/P2X7/Pannexin-1 sensitivity to extracellular ATP via Ivermectin induces a non-apoptotic and inflammatory form of cancer cell death. *Sci. Rep.* **5**, 16222 (2015).
61. O. Kepp, L. Bezu, T. Yamazaki, F. Di Virgilio, M. J. Smyth, G. Kroemer, L. Galluzzi, ATP and cancer immunosurveillance. *EMBO J.* e108130 (2021).
62. B. Rissiek, F. Haag, O. Boyer, F. Koch-Nolte, S. Adriouch, P2X7 on mouse T cells: One channel, many functions. *Front. Immunol.* **6**, 204 (2015).
63. K. Dreisig, B. R. Kornum, A critical look at the function of the P2Y11 receptor. *Purinergic Signal*. **12**, 427–437 (2016).
64. K. Dreisig, L. Sund, M. W. Dommer, N. P. Kristensen, K. Boddum, R. Viste, S. Fredholm, N. Odum, M. Jättelä, S. Skov, B. R. Kornum, Human P2Y11 expression level affects human P2X7 receptor-mediated cell death. *Front. Immunol.* **9**, 1159 (2018).
65. C. Vial, A. B. Tobin, R. J. Evans, G-protein-coupled receptor regulation of P2X1 receptors does not involve direct channel phosphorylation. *Biochem. J.* **382**, 101–110 (2004).
66. B. P. Diercks, R. Wemer, D. Schetelig, I. M. A. Wolf, A. H. Guse, High-resolution calcium imaging method for local calcium signaling. *Methods Mol. Biol.* **1929**, 27–39 (2019).
67. P. Pelegrin, A. Surprenant, Pannexin-1 mediates large pore formation and interleukin-1 β release by the ATP-gated P2X7 receptor. *EMBO J.* **25**, 5071–5082 (2006).
68. M. Arigovindan, J. C. Fung, D. Elnatan, V. Mennella, Y. H. M. Chan, M. Pollard, E. Branlund, J. W. Sedat, D. A. Agard, High-resolution restoration of 3D structures from widefield images with extreme low signal-to-noise ratio. *Proc. Natl. Acad. Sci. U.S.A.* **110**, 17344–17349 (2013).
69. L. M. Woelk, S. A. Kannabiran, V. J. Brock, C. E. Gee, C. Lohr, A. H. Guse, B. P. Diercks, R. Wemer, Time-dependent image restoration of low-SNR live-cell Ca^{2+} fluorescence microscopy data. *Int. J. Mol. Sci.* **22**, 11792 (2021).
70. T. Nauth, F. Huschka, M. Schweizer, J. B. Bosse, A. Diepold, A. V. Failla, A. Steffen, T. Stradal, M. Wolters, M. Aepfelbacher, Visualization of translocons in Yersinia type III protein secretion machines during host cell infection. *PLOS Pathog.* **14**, e1007527 (2018).

Acknowledgments: We acknowledge discussions with members of The Calcium Signalling Group and members of SFB 1328. Nb13A7 can be provided by F.K.–N. pending scientific review and a completed material transfer agreement. Requests for Nb13A7 should be submitted to nolte@uke.de. **Funding:** This work was supported by Deutsche Forschungsgemeinschaft (DFG) (project number 335447717; SFB 1328, project A01 to A.H.G.; project A02 to B.–P.D. and R.W.; project A03 to H.–W.M.; project A10 and Z01 to F.K.–N.; and project A11 to C.E.M.); Joachim-Herz-Stiftung (Hamburg), Infectophysics Consortium (project 4, to A.H.G.); NCL-Stiftung Hamburg (to A.H.G.); the Hamburg Ministry of Science, Research and Equality (LF-FV75/0070-134, to A.H.G.); and University Medical Center Hamburg-Eppendorf (M31 consortium, to A.H.G.). **Author contributions:** Conceptualization: I.M.A.W., A.H.G., and B.–P.D. Methodology: V.J.B., B.–P.D., L.–M.W., R.W., M.E.–L.B.R., T.S., F.K.–N., and C.E.M. Investigation: V.J.B., M.E.–L.N.L., and T.S. Visualization: V.J.B., I.M.A.W., N.L., A.H.G., and B.–P.D. Funding acquisition: I.M.A.W., B.–P.D., R.W., A.H.G., F.K.–N., C.E.M., and H.–W.M. Supervision: B.–P.D., I.M.A.W., R.W., A.H.G., F.K.–N., C.E.M., and H.–W.M. Writing—original draft: V.J.B. Writing—review and editing: V.J.B., B.–P.D., A.H.G., R.W., B.R., and H.–W.M. **Competing interests:** F.K.–N. is the inventor on a patent related to this work, filed by the University Medical Center Hamburg-Eppendorf and Ablynx NV (WO2013178783, filed on 31 May 2013, published on 5 December 2013). The authors declare no other competing interests. **Data and materials availability:** All data needed to evaluate the conclusions in the paper are present in the paper and/or the Supplementary Materials.

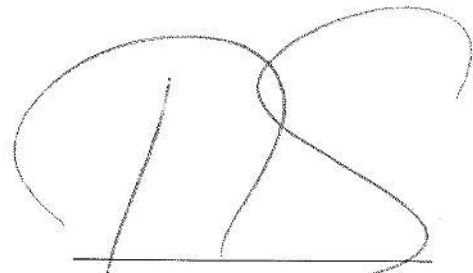
Submitted 17 August 2021
Accepted 14 December 2021
Published 4 February 2022
10.1126/sciadv.abl9770

2.2.1 Publication II: Contribution

In this publication, the roles of the purinergic cation channels P2X4 and P2X7 and of the ATP releasing channel PANX1 on the formation of Ca^{2+} microdomains were analyzed using a high-resolution live-cell-imaging system as described earlier by our group (Diercks et al., 2019; Wolf et al., 2015). I performed all Ca^{2+} microdomain measurements in murine CD4^+ T cells in the presence and absence of direct TCR/CD3 stimulation with and without anti-CD3/anti-CD28 coated beads. To elucidate the influence of P2X4, P2X7 and PANX1 on the formation of Ca^{2+} microdomains, I used a wide set of approaches, including knockout mouse models, chemical antagonists, inhibiting nanobodies, apyrase and inactivated apyrase. Additionally, I was responsible for the co-localization measurements of P2X4 and P2X7 using super-resolution imaging with optical reassignment (SoRa) to analyze the interaction of the channels. Downstream effects of the P2X4 and P2X7 channel deficiency were studied. Thus, I measured global Ca^{2+} signals in the T cells loaded with Fura-2. Finally, I carried out the statistical data analysis, prepared the figures and wrote the first draft of the manuscript.

Hamburg, May 13, 2022

Place, Date



Signature of the supervisor

Prof. Dr. Dr. Andreas H. Guse
Direktor

2.2.2 Publication II: Paper of the Month

**UKE Paper of the Month März 2022****P2X4 and P2X7 are essential players in basal T cell activity and Ca²⁺ signaling milliseconds after T cell activation**

Brock, Valerie J, Wolf, Insa M A, Er-lukowiak, Marco Lory, Niels, Stähler, Tobias, Woelk, Lena-Marie, Mittrücker, Hans-Willi, Müller, Christa E, Koch-Nolte, Friedrich, Rissiek, Björn, Werner, René, Guse, Andreas H, Diercks, Björn-Philipp

[Science Advances 2022 Feb 04; 8 \(5\). eab19770](https://doi.org/10.1126/science.adb19770)

ABSTRACT:

Initial T cell activation is triggered by the formation of highly dynamic, spatiotemporally restricted Ca²⁺ microdomains. Purinergic signaling is known to be involved in Ca²⁺ influx in T cells at later stages compared to the initial microdomain formation. Using a high-resolution Ca²⁺ live-cell imaging system, we show that the two purinergic cation channels P2X4 and P2X7 not only are involved in the global Ca²⁺ signals but also promote initial Ca²⁺ microdomains tens of milliseconds after T cell stimulation. These Ca²⁺ microdomains were significantly decreased in T cells from P2rx4^{-/-} and P2rx7^{-/-} mice or by pharmacological inhibition or blocking. Furthermore, we show a pannexin-1– dependent activation of P2X4 in the absence of T cell receptor/CD3 stimulation. Subsequently, upon T cell receptor/CD3 stimulation, ATP release is increased and autocrine activation of both P2X4 and P2X7 then amplifies initial Ca²⁺ microdomains already in the first second of T cell activation.

STATEMENT:

Although, the ATP-gated channels P2X4 and P2X7 were shown to influence global Ca²⁺ signals and the immune response some years before, their role in the formation of initial Ca²⁺ signals in the first milliseconds after T cell activation was still unclear. In this publication, we show for the first time the role of P2X4 and P2X7 on the formation of Ca²⁺ microdomains before and after T cell stimulation. The infrequent, T cell receptor stimulation independent Ca²⁺ microdomains are promoted by P2X4 but not by P2X7. In contrast, only P2X7 influence the expression of NUR77 and the proliferation of the T cells. The results highlight the functional differences of P2X4 and P2X7 and opens up advanced possibilities for clinical interventions based on these differences.

BACKGROUND:

This work was mainly performed in the Ca²⁺ Signalling Group, Department of Biochemistry and Molecular Cell Biology, by the first authors Valerie J. Brock and supervised by Björn-Philipp Diercks. Importantly, the project was supported by the DFG SFB1328 “Adenine Nucleotides in Immunity and Inflammation” project A02, A03, A11 and Z02.

3. Discussion

3.1 Summary of the results implemented in this thesis

The aim of this PhD project was to understand the impact of purinergic signaling on the formation of initial Ca^{2+} microdomains. The visualization of Ca^{2+} signals, especially of the spatiotemporally restricted Ca^{2+} microdomains, is challenging. To this end, an advanced image deconvolution algorithm was adjusted for Ca^{2+} imaging sequences. The unique algorithm, which emphasizes the time dependency of an imaging sequence for image reconstruction, was tested on different datasets concerning Ca^{2+} imaging: (i) one synthetic dataset with simulated Ca^{2+} signals, (ii) two datasets visualizing Ca^{2+} microdomains with different Ca^{2+} indicators in T cells and (iii) another dataset of spontaneous Ca^{2+} signals in astrocytes.

As major part, we analyzed the role of the ATP-gated cation channels P2X4 and P2X7 on the formation of Ca^{2+} microdomains using either knockout mice, pharmacological antagonists or inhibiting nanobodies. For the first time, P2X4 and P2X7 channels were shown to promote the formation of Ca^{2+} microdomains milliseconds after T cell stimulation. Moreover, this thesis hypothesized that extracellular ATP released from the activated cell via PANX1, fosters the Ca^{2+} microdomain formation by activating the P2X channels. In CD4^+ T cells, in the absence of direct TCR/CD3 stimulation, the purinergic axis of P2X4/PANX1 triggered the formation of Ca^{2+} microdomains with lower amplitude and frequency compared to those occurring after TCR/CD3 stimulation. Co-localization analysis of P2X4 and P2X7 revealed no functional interaction of the two channels during the formation of initial Ca^{2+} microdomains in the absence or presence of TCR/CD3 stimulation. An extended (5 min) stimulation of the T cell with an anti-CD3 antibody increased colocalization of P2X4 and P2X7. Finally, global Ca^{2+} signaling was decreased in both, *P2rx4*^{-/-} and *P2rx7*^{-/-}. In contrast, only in T cells of *P2rx7*^{-/-}, but not of *P2rx4*^{-/-}, the expression of NUR77 and the proliferation of the T cells was reduced, revealing functional differences of the two purinergic channels in T cells.

3.2 Ca^{2+} signaling: image restoration

Deconvolution techniques can improve the resolution of a blurred image or reconstruct the blurred image of an object (Wallace et al., 2001). Several image restoration techniques have been developed and are suitable for different approaches, like photography (Kang, 1998) and microscopy (McNally et al., 1999; Sage et al., 2017). This thesis aimed to extend a deconvolution algorithm suited for fluorescence image sequences of Ca^{2+} microdomains.

3 Discussion

Common algorithms are often optimized for natural images and applied to fluorescence images regardless of their highly different characteristics. Fluorescence images generally show small, single structures on dark backgrounds, whereas natural images, e.g. photos, contain different structural elements with smooth transitions of brighter to darker elements and more colors (Dey et al., 2006; Kang, 1998; McNally et al., 1999; Schelten et al., 2015). Deconvolution algorithms generate estimations of an original object to create an image of it (Wallace et al., 2001). To this end, different approaches are needed for fluorescence images compared to other images. Arigovindan and colleagues (2013) assume that fluorescence images are characterized by sparsely distributed high-intensity points. They introduced an “entropy-like” regularizer term with a logarithmic weighting that has a more pronounced sparsifying effect for the intensity variations in fluorescence images. They claim and experimentally show that their algorithm captures the spatial image patterns of fluorescence images better than commonly used modern methods (Fig. 3.1), e.g. Huygens constrained maximum-likelihood method (Arigovindan et al., 2013).

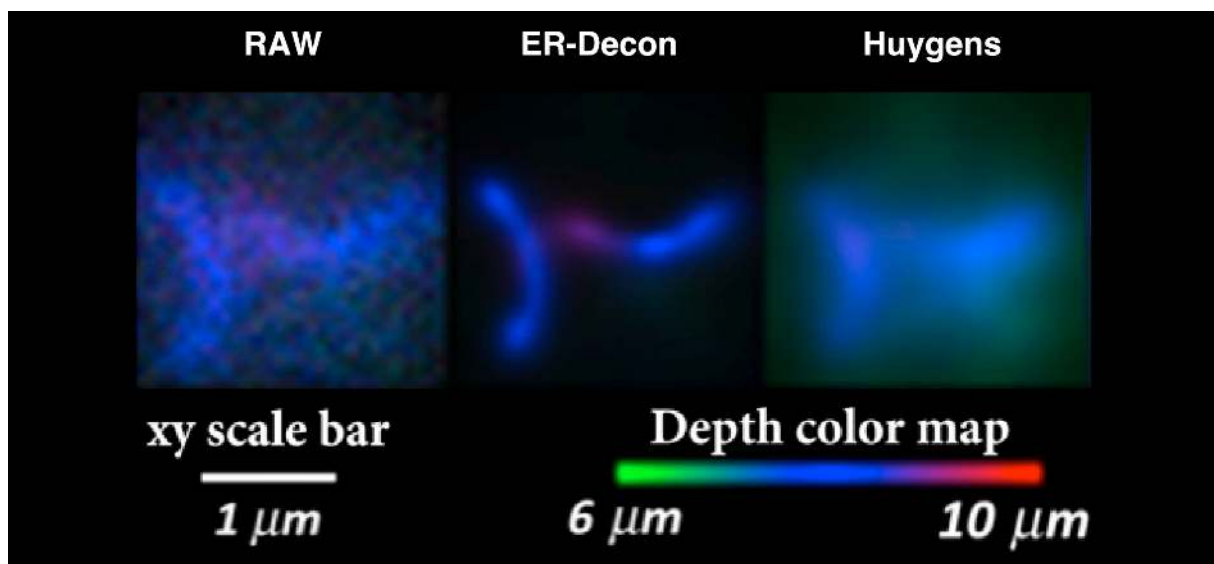


Figure 3.1: Spatial image patterns were captured better by the “entropy-like” deconvolution algorithm (ER-Decon). Depth color-coded z-projections of deconvolved live images of yeast Zip1 filament. Raw image (left, RAW). Image after deconvolution with the “entropy-like” algorithm (middle, ER-Decon) and after deconvolution with Huygens constrained maximum-likelihood method (right, Huygens). Modified from Arigovindan et al. 2013.

The algorithm emphasizes the spatial characteristics of a fluorescence image, whereas it does not address the temporal characteristics of an image sequence. The Ca^{2+} microdomain measurements we usually perform, are sequences and not single-frame images. The spatial features of a single frame can change in a series of multiple frames. Deconvolution algorithms like the “entropy-like” algorithm deal with this only for every single frame (Arigovindan et al., 2013), while temporal relationships are not considered. Thus, the “entropy-like” algorithm, including the spatial regularization (Arigovindan et al., 2013), was extended during this thesis by the time-dependency of an image sequence. The advantage of the extended algorithm is a

3 Discussion

new regularizer term utilizing now the temporal information of an image sequence to improve the temporal resolution (Woelk et al., 2021). To this end, not only Ca^{2+} imaging sequences will benefit from the new deconvolution algorithm but also a wide range of other molecular fluorescence approaches analyzing time-dependent changes.

Although deconvolution techniques can enhance the spatial and temporal resolution of a blurred image, artifact formation is a problem. Artifacts are characterized by the loss of very dim signals and structures or the blurring or “blowing up” of very bright signals (Wallace et al., 2001). For example, the Lucy-Richardson algorithm often produces intensity oscillation artifacts due to a noise amplification after a small number of iterations, which can be clearly improved by a specific regularization term (Dey et al., 2006). Here, our algorithm tends to blur only spots of very high Ca^{2+} concentrations, which might be due to the commonly used data fidelity component of the algorithm that suppresses high-frequency components (Woelk et al., 2021). In future approaches, this commonly used data fidelity component needs to be adjusted to improve the algorithm for high SNR images.

The algorithm was written using the scripting language Python, enhancing the portability to different platforms like Windows or Macintosh (Chapman & Chang, 2000). Moreover, Python is easy to read for a wide community and the established code consists of only a few data-dependent adjustable parameters (Arigovindan et al., 2013; Woelk et al., 2021), increasing user-friendliness. The adjustable parameters influence the smoothness and restoration of weak intensities in the spatial and temporal direction (Arigovindan et al., 2013; Woelk et al., 2021) and the iterative nature of the algorithm might increase artifacts by amplifying it (Anastasopoulou et al., 2019). Anastasopoulou and colleagues (2019) described the appearance of artifacts in their image with a higher iteration number during their optimization of parameters for a different iterative deconvolution algorithm. Nevertheless, iterations do not necessarily increase artifact formation. Thus, the adjustable parameters must be chosen thoughtfully, depending on the used algorithm and the input data.

3.3 The complexity of the Ca^{2+} channel network

The formation of Ca^{2+} microdomains is a quite complex network of different, interacting key players of Ca^{2+} release and entry channels (Brock et al., 2022; Diercks et al., 2018; Gu et al., 2021; Roggenkamp et al., 2021; Wolf et al., 2015). The second messenger NAADP, which is rapidly produced by the NADPH oxidase DUOX2 (Gu et al., 2021) and orchestrated by the NAADP-binding protein HN1L/JPT2, targets the RYR1 channel in the ER membrane (Roggenkamp et al., 2021). Ca^{2+} release from the ER is sensed by STIM1 and STIM2, activating SOCE by ORAI1 (Diercks et al., 2018). We recently published the role of the ATP-gated cation channels P2X4 and P2X7 on the formation of Ca^{2+} microdomains (Brock et al.,

3 Discussion

2022), pointing out another, so far unknown key player of the Ca^{2+} microdomain formation network. A question that arises is why Ca^{2+} microdomain formation is influenced by such a huge network of different channels and proteins? Since global Ca^{2+} signaling maintains many diverse cell responses, like cytokine expression, cell metabolism, migration, invasion and differentiation (Bootman & Bultynck, 2020; Gu et al., 2021; Ledderose et al., 2018; Macian, 2005; Y. Wang et al., 2020), the versatility of interacting proteins forming Ca^{2+} microdomains might direct the responses of the cells depending on their physiological needs.

The translocation of NFAT to the nucleus was shown to be triggered by Ca^{2+} signals formed by NAADP-mediated RYR1 activity, SOCE and purinergic signaling via the P2X channels (Dammermann et al., 2009; Emrich et al., 2021; Prasai et al., 2011). The structure of the NFAT DNA-binding domain is highly flexible, permitting the interaction with many different transcription partners, like the activator protein (AP) 1 or the interferon regulatory factor 4 (IRF4) (Jain et al., 1992; Macian, 2005; Rengarajan et al., 2002). Thus, NFAT activation induces diverse T cell responses, like the expression of different cytokines, proliferation and differentiation (Amasaki et al., 2002; Macian, 2005; Yoshida et al., 1998).

Kar and colleagues (2011) revealed that local Ca^{2+} signals have a greater impact on the initiation of the translocation of NFAT1 than long-lasting global Ca^{2+} signals. Additionally, they proposed a so-called "short term memory" of the NFAT1 translocation to maintain gene expression long after the initiation by local Ca^{2+} signals (Kar et al., 2011). In hippocampal neurons, a similar observation was described. After a short 3 min depolarization, a persistent, heightened level of nuclear NFATc4 was detected up to 60 min (Oliveria et al., 2007). Incubation of the cells with a fast Ca^{2+} chelator (BAPTA) and a slow chelator (EGTA) indicated the dependency of NFAT translocation on spatiotemporally restricted Ca^{2+} signals. NFATc4 translocation was strongly suppressed by BAPTA, whereas EGTA treatment did not alter NFATc4 movement (Oliveria et al., 2007). The dependency of NFAT translocation on spatiotemporally restricted Ca^{2+} signals and the versatility of the output of NFAT gene transcription seems to be one part of the explanation for the utility of the complex network of Ca^{2+} microdomain modulators.

However, cell migration has also been described to be dependent on precisely coordinated Ca^{2+} signals. In non-excitabile melanoma cells, it was shown that their ability to initiate invadopodia formation, degradation of extracellular membrane and migration into tissues, is coordinated by a SOCE-dependent Ca^{2+} /calmodulin – proline-rich tyrosine kinase 2 (Pyk2) – sarcoma (Src) kinase pathway (Lu et al., 2019). They observed spontaneous " Ca^{2+} glows" originated exclusively from Ca^{2+} entry and not from Ca^{2+} release from cellular Ca^{2+} stores. Moreover, they demonstrated that SOCE-mediated Src activation only occurs in adherent cells due to the activation of the cell adhesion kinase Pyk2 (Lu et al., 2019). Newest findings in an

3 Discussion

osteosarcoma cell line suggest that the migratory ability is affected by different SOCE levels due to constitutively active STIM1 or dominant negative STIM1 (Lin et al., 2022). Many studies discuss the impact of SOCE on adhesion and migration (Hammad & Machaca, 2021; Lin et al., 2022; Lu et al., 2019), although, Ca^{2+} signals promoted by P2X4 were implicated in T cell migration (Ledderose et al., 2018). After T cell activation, P2X4 is activated at the front of the cell, while P2Y11 receptors at the back trigger mitochondrial trafficking to the activation site to stabilize the formation of the immune synapse and amplify Ca^{2+} signals promoted by P2X7 (Ledderose et al., 2020). This mechanism highlights the role of precisely localized Ca^{2+} signals to initiate directed cell migration.

All these cellular processes need energy. Accordingly, Ca^{2+} signaling is linked to energy metabolism of a cell. Stimulation of T cells rapidly increases ATP production inside the mitochondria which translocate towards the immune synapse (Ledderose et al., 2014, 2018). Already in unstimulated cells a basal $\text{IP}_3\text{R-MCU}$ -mediated Ca^{2+} transfer from the ER into the mitochondrion is essential for optimal mitochondrial activity and cellular bioenergetics (Cárdenas et al., 2010). The mitochondria not only sense IP_3R -mediated Ca^{2+} signals for their energy production, but also were shown to regulate SOCE by buffering high $[\text{Ca}^{2+}]_i$ concentrations, which otherwise results in a negative feedback loop inhibiting SOCE (Hoth et al., 1997).

Conclusively, these data reveal the complexity of the Ca^{2+} microdomain network and the interplay with ATP and purinergic signaling, and finally highlight the importance of fine-tuning it.

3.4 P2X4 and P2X7: structural and functional differences

In this thesis, we analyzed the influence of P2X4 and P2X7 on the formation of Ca^{2+} microdomains and identified different time periods of action of the two channels (Brock et al., 2022).

Analysis of the structure might give insights into the functional differences, although the structure of the P2X channels show many similarities. Especially the overall shape of the dolphin-like extracellular and transmembrane domains is comparable (Hattori & Gouaux, 2012; Mansoor et al., 2016; McCarthy et al., 2019). Three ATP-binding sites are present in a trimeric P2X channel at each interface of a subunit pair (Hattori & Gouaux, 2012). The ATP-binding sites are located in the extracellular domains and coordinated by the head, left flipper and upper body of one subunit and by the dorsal fin and lower body of the neighboring subunit (Hattori & Gouaux, 2012; Sheng & Hattori, 2022). The naming of the structural elements is related to the dolphin-like shape of the P2X channels. The ATP forms a U-shape with the β - and γ -phosphates folded towards the adenine ring inside the binding pocket (Hattori & Gouaux, 2012). Comparison of, e.g. the human P2X3 (hP2X3, a P2X channel with a high ATP affinity)

3 Discussion

and rat P2X7 (rP2X7, the P2X channel with the lowest ATP affinity) demonstrated that the U-shape form of ATP and the shape of the occupied binding pocket are virtually identical (McCarthy et al., 2019). Thus, we will have a deeper look into the channel structures, to identify structural differences, that might correlate with the functional differences observed in this thesis.

Differences of the ATP binding pocket demonstrate one first insight into channel differences. The binding pocket of the rP2X7 comprises a narrow channel (Fig.2, 11 \AA orifice) in the apo state, whereas the hP2X3 binding pocket shows a wider channel (Fig. 3.2, 17 \AA orifice) (McCarthy et al., 2019). This observation correlates with the size of ATP of 14 \AA (Azarashvili et al., 2011), limiting the ligand access for a channel with a smaller orifice. Moreover, this correlation might be related to the different ATP affinities of the channels. While P2X3 is sensitive to ATP concentrations in the nanomolar range, P2X7 gets activated at ATP concentrations in the micromolar range (Kaczmarek-Hájek et al., 2012). In contrast, the P2X4 channel shows intermediate ATP affinities between P2X3 and P2X7, that also correlates with an intermediate ATP binding pocket orifice of approx. 15 \AA of the zebrafish P2X4 (zfP2X4) structure (Fig. 3.2). The ligand accessibility might explain the different times of activity of P2X4 and P2X7 observed in this thesis. Since ATP can access the P2X4 channel easier due to the wider orifice compared to the one of P2X7, P2X4 might be activated earlier and, like proposed before, is more sensitive to ATP. More experiments are needed to confirm the effects of the ligand accessibility on the differences in ATP affinity of the P2X channels.

Moreover, in the binding pocket of the P2X4 channel, an amino acid substitution of leucine

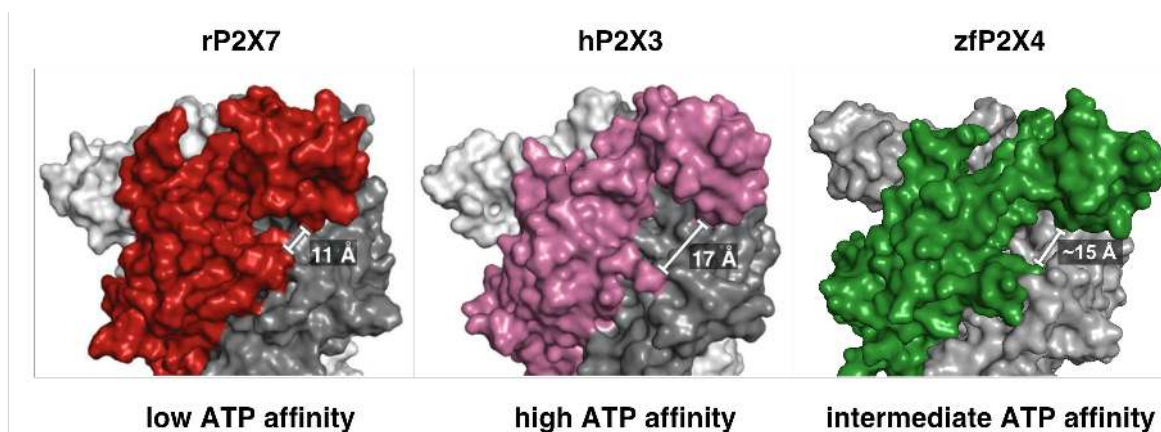


Figure 3.2: Extracellular orthosteric binding site. Comparison of the binding pocket orifice of the rP2X7 and hP2X3 in the apo state with the binding pocket of the zfP2X4 in the apo state. Figures of rP2X7 and hP2X3 modified from McCarthy et al. 2019. zfP2X4 crystal structure published by Hattori and Gouaux 2012 and displayed with PyMOL (Version 2.5.2, Schrödinger, LLC.). Distance measurement of the zfP2X4 orifice by PyMOL.

(Leu) at L214 of the dorsal fin domain alters ligand binding and signal transduction (Zhang et al., 2014). The L214 directly hydrophobically interacts with the ATP and influences channel desensitization (Zhang et al., 2014). In contrast, in the P2X3 channel the residue serine (S) 275 in the left flipper is implicated in ATP binding and desensitization (Petrenko et al., 2011).

3 Discussion

Zhang and colleagues (2014) tested for the P2X4 channel different amino acids substitutions at the position L214, which resulted in more rapidly desensitizing channels, like the isoleucine (Ile) of P2X1 and the methionine (Met) of P2X3 channel. Under natural conditions, the P2X4 channels show a slower desensitization compared to P2X1 and P2X3, whereas no desensitization has been described for P2X7 (Habermacher et al., 2016; McCarthy et al., 2019). The substitution of Leu in the residue L214 in P2X4 with Ile increases and with Met decreases the desensitization rate. Consequently, they hypothesized that this residue might influence agonist orientation inside the binding pocket (Zhang et al., 2014).

These results demonstrate the structural influence on the different ATP affinities, which are linked to functional differences of the P2X channels. In this thesis, the P2X4 channel, but not the P2X7, was demonstrated to influence TCR/CD3-independent Ca^{2+} microdomains (Brock et al., 2022), correlating with its higher ATP affinity. Since a first, so far measurable, ATP burst occurs within 30 seconds after T cell stimulation (Ledderose et al., 2014), a lower ATP release might appear already in the absence of direct TCR/CD3 stimulation, which can activate the more sensitive P2X4 channel. These assumed spatiotemporally restricted ATP microdomains need further investigations. Additionally, the different channel desensitization rates could be associated with the different time spots of P2X4 and P2X7 activity. For P2X7, no desensitization is described (McCarthy et al., 2019), correlating with the greater impact of P2X7 on the downstream signals in T cells, like its influence on the expression of NUR77 (Brock et al., 2022).

Another approach to explain the functional differences of P2X channels is an additional key for channel desensitization introduced in 2016 by Mansoor and colleagues. They claim that the cytoplasmic cap, found in the crystal structure of the hP2X3, stabilizes the channel opening and, to this end, sets the rate for channel desensitization (Mansoor et al., 2016). Removal of the flexible cytoplasmic cap leads to a recoil of the TM2 for channel desensitization (Mansoor et al., 2016). Analysis of the rP2X7 channel structure confirmed the influence of the cytoplasmic cap on channel desensitization. In rP2X7, the cytoplasmic cap is anchored by long fatty acids and this prevents the TM2 recoiling for channel desensitization (McCarthy et al., 2019). The differences of the cytoplasmic cap in P2X3 and P2X7 are associated with the variations in desensitization of these channels. Since the proposed structure of the P2X4 channel is truncated in the cytosolic region (Hattori & Gouaux, 2012; Kawate et al., 2009), no cytoplasmic cap for this channel is described so far. It can be assumed that the P2X4 channel shows structural characteristics of the cytoplasmic cap between the fast-desensitizing P2X3 channel and the non-desensitizing P2X7 channel due to its intermediate desensitization properties. Further investigations in the structure of the cytosolic region of the P2X4 channel are needed to confirm this assumption. The structural analysis of the P2X channels, and further

3 Discussion

the implication of different amino acid residues and channel domains on ATP binding properties and channel desensitization demonstrate the complexity of the P2X channel gating. Thus, the complexity of P2X channel gating may explain the wide range of functional activities of the P2X channels, especially of P2X4 and P2X7.

As mentioned before, we demonstrated different time periods for P2X4 and P2X7 activity. While P2X4 is already active prior direct TCR/CD3 stimulation, P2X7 gets activated after TCR/CD3 stimulation (Brock et al., 2022), possibly due to the specific ATP binding properties of P2X4 and P2X7. The early activity of P2X4 might forward a rapid response within milliseconds to an external T cell stimulus. Following T cell stimulation, P2X4 but not P2X7 translocates to the immune synapse (Woehrle et al., 2010). Both channels promote the formation of Ca²⁺ microdomains after TCR/CD3 stimulation (Brock et al., 2022), and further amplify the Ca²⁺ signals for a global Ca²⁺ response and T cell activation (Brock et al., 2022; Trebak & Kinet, 2019; Woehrle et al., 2010; Yip et al., 2009). The P2X7 channel might have a higher impact on the amplification of the Ca²⁺ response because of the non-desensitizing properties of this channel. The cytosolic ballast of P2X7 contains a binding site for guanine nucleotides and a dinuclear zinc ion complex (McCarthy et al., 2019), indicating interactions of P2X7 with other proteins, which might also alter channel functions compared to other P2X channels.

Functional differences of P2X4 and P2X7 are described, e.g. their influence on cell migration. Stimulation of human CD4⁺ T cells and of the human leukemia cell line Jurkat with the chemokine CXCL12, which binds to the chemokine receptor CXCR4, triggers T cell migration to the APC controlled by the accumulation of mitochondria with the P2X4 receptor at the front of the T cells (Ledderose et al., 2018). In this context, inhibition of the P2X7 channel did not alter migration speed, whereas inhibition of P2X4 decreased migration speed (Ledderose et al., 2018). The cell migration (speed and range) was correlated with the expression level of CD69 (Ledderose et al., 2018), which is a marker for early T cell activation (Ziegler et al., 1994). Inhibition of P2X4 significantly decreased CD69 expression after stimulation with the chemokine, whereas inhibition of P2X7 did not effect it (Ledderose et al., 2018).

Additionally, in human PBMC cells stimulated with soluble anti-CD3, the CD69 expression was decreased in T cells after P2X4 inhibition (Ledderose et al., 2020). The proposed stimulation condition ensures that the CD4⁺ T cells directly interact with APCs to achieve the required co-stimulation with the CD28 co-receptor for a complete T cell activation (Ledderose et al., 2020). In contrast, in this thesis, the CD69 expression was not altered in murine *P2rx4*^{-/-} and *P2rx7*^{-/-} T cells after stimulation with soluble anti-CD3 and anti-CD28 (Brock et al., 2022), indicating a possible stimulus-dependent activation of P2X4 to promote migration of the T cell to the APC, which is followed by the T cell activation. The activity of P2X4 during cell migration further

3 Discussion

correlates with the low-grade activity of P2X4 in the absence of direct TCR/CD3 stimulation described in this thesis (Brock et al., 2022). P2X4 might act as a precursor to promote T cell migration to the APC to initiate Ca^{2+} microdomain formation and to stabilize the immune synapse followed by a fostered ATP release and production, P2X7 stimulation and a strong activation of the T cell.

Consequently, the P2X7 channel activity might be required for a strong T cell response, which is reflected by the decreased expression level of Nur77 (a marker of the strength of T cell stimulation) in murine *P2rx7^{-/-}* T cells (Brock et al., 2022). Analysis of the responses of the P2X4 and P2X7 channels to different stimuli in human and murine T cells will further elucidate the functional differences of these two channels during the T cell activation. Furthermore, investigations in the structural difference of P2X4 and P2X7, will help to produce highly specific antagonists and agonists for their functional differentiation.

3.5 ATP release

The P2X channels, analyzed in this thesis, are ATP gated. Extracellular ATP is proposed to activate the channels for opening and Ca^{2+} influx. Hence, the first approach to analyze the impact of extracellular ATP on the formation of Ca^{2+} microdomains after TCR/CD3 stimulation was to remove the extracellular ATP. To this end, T cells were incubated with apyrase, which is an ATP degrading enzyme (Handa & Guidotti, 1996), resulting in significantly reduced Ca^{2+} microdomains (Brock et al., 2022). Moreover, previous publications have highlighted the PANX1 channel releasing the ATP after T cell stimulation to activate the P2X channels (Schenk et al., 2008; Woehrle et al., 2010). Thus, we analyzed Ca^{2+} microdomains in cells incubated with a PANX1 antagonist in the presence and absence of direct TCR/CD3 stimulation (Brock et al., 2022). TCR/CD3-independent Ca^{2+} microdomains were reduced after PANX1 inhibition, indicating a required ATP release during this stage of T cell activity. ATP release independent of cell stimulation was already proposed in other cell types. In human bone marrow-derived mesenchymal stem cells (hMSCs), spontaneously occurring Ca^{2+} oscillations were evoked by CNX hemichannel-mediated ATP release (Kawano et al., 2006). Since many studies reveal the role of ATP acting as an autocrine and paracrine signaling molecule (Bours et al., 2006; Junger, 2011; Trabanelli et al., 2012), a precise release of spatiotemporally restricted ATP microdomains in the absence of direct TCR/CD3 stimulation is not unlikely to forward rapid responses.

The release of ATP is a well-organized mechanism mediated by a wide range of releasing channels and proteins or exocytosis (Pankratov et al., 2007; Taruno, 2018; Y. Wang et al., 2013). A huge variety of pharmacological and biological antagonists were used to identify and differentiate ATP releasing channels like CNX, PANX1 or voltage-regulated channels

3 Discussion

(VRAC/MACs) in many cell types (Lohman & Isakson, 2014). The proposed specific gap junction blocker carbenoxolone (CBX) inhibits not only PANX1 and different CNX (Bruzzone et al., 2005) but also VRAC-mediated currents (Benfenati et al., 2009; Zahiri et al., 2021). Hence, CBX is only one example demonstrating the specificity issues of the pharmacological antagonists for ATP releasing channels.

Since the specificity of pharmacological approaches to distinguish between the ATP releasing channels was unsatisfactory, another method was introduced producing specific mimetic peptides mimicking primary amino acid sequences of the CNX or PANX1 channels (Dahl et al., 1994; Lohman & Isakson, 2014). The initial idea of these mimetic peptides was to imitate the docking gate of gap junction channels (Dahl et al., 1994; J. Wang et al., 2007). The peptides were used to inhibit CNX or PANX1 channels specifically. However, an inhibitory effect of CNX mimetic peptides on PANX1 was demonstrated and *vice versa*, hypothesizing the mechanism of action of these “mimetic” peptides is by a steric channel block rather than mimicking some gap junction protein characteristics (J. Wang et al., 2007).

The antagonist for PANX1 used in this theses was the mimetic peptide ¹⁰Panx1 (Brock et al., 2022). Thus, we cannot exclude the role of CNX in the release of ATP during the formation of Ca²⁺ microdomains. Analysis of CNX in lymphocyte subpopulations reveal the surface expression of the CNXs Cx40 and Cx43, which were upregulated after cell stimulation (Oviedo-Orta et al., 2000). Additionally, an ATP release via vesicular exocytosis after T cell stimulation was reported in previous studies (Tokunaga et al., 2010). Hence, the ATP releasing mechanism during the formation of Ca²⁺ microdomains needs to be addressed in more detail. Knockout models and more specific pharmacological approaches, as well as the development of highly specific inhibiting nanobodies for CNX and PANX1 like those already available for P2X7 (Danquah et al., 2016), might be suitable strategies to validate the results.

For PANX1, a knockout mouse line is available, but it is bred on C57BL/6J background (Vandenbeuch et al., 2015). We performed all mouse experiments implemented in this study on the Balb/C background due to a single nucleotide polymorphism (SNP) of *P2rx7*. Different mouse lines carry either a proline (Pro) or a Leu at the position 452 of the C-terminal tail of the P2X7 receptor, influencing P2X7 mediated pore formation (Adriouch et al., 2002), but not Ca²⁺ flux (Le Stunff et al., 2004; Sorge et al., 2012). The *P2rx4*^{-/-} C57BL/6J mouse was backcrossed from a Balb/C background and differs from the WT C57BL/6J in the single nucleotide polymorphism of *P2rx7*, leading to a higher P2X7 surface expression and a higher sensitivity to ATP and NAD⁺ compared to the WT (Er-Lukowiak et al., 2020). Although Ca²⁺ signaling is not directly influenced by the SNP, we decided to work on the Balb/C background to enable comparability of T cells from *P2rx4*^{-/-} and *P2rx7*^{-/-} and the corresponding WT. Accordingly,

3 Discussion

analysis of the inhibited PANX1 channel were performed on the same mouse background, on which no PANX1 knockout is available.

3.6 Species-dependent differences: transferability of mouse data

The influence of the purinergic signaling via PANX1, P2X4 and P2X7 on the formation of Ca²⁺ microdomains described in this thesis was studied in primary murine T cells. Using knockouts of P2X4 and P2X7 enabled a clear differentiation of the channel function, especially in the formation of TCR/CD3-independent Ca²⁺ microdomains. As we have seen for the differentiation of ATP releasing channels, pharmacological antagonists are often lacking specificity, while side effects cannot be excluded for a knockout as well as pharmacological approaches. In the study implemented in this thesis, we used both knockout and pharmacological or nanobody-mediated inhibition of P2X4 and P2X7, verifying the functional effects (Brock et al., 2022). The aim of analyzing the influence of these channels on the formation of Ca²⁺ microdomains was to elucidate the mechanism of T cell activation as an initial part of the adaptive immune response, thus opening up new possibilities for therapeutic targets. Accordingly, it might be interesting to discuss if and to what extent the data acquired using murine T cells are transferable to humans.

A very remarkable difference is the P2Y11 receptor that is expressed in human but not in murine cells (Dreisig & Kornum, 2016). The P2Y11 receptor is associated with an ATP-, NAD⁺- or NAADP-mediated Ca²⁺ and AC signaling as well as cAMP production (Dreisig & Kornum, 2016; Moreschi et al., 2006, 2008). Moreover, P2Y11 was shown to influence P2X7. The GPCR receptor affects the sensitivity of P2X7 to ATP and protects the cells against pore formation and cell death, whereas P2X7-associated Ca²⁺ signaling is not influenced (Dreisig et al., 2018). Dreisig and colleagues (2018) postulated that the decreased responsiveness of naïve human CD8⁺ T cells to ATP was due to the P2Y11 receptor expression. Since murine T cells lack the *P2ry11*, the species-dependent differences in ATP responsiveness might also be due to this receptor, although some studies hypothesize the existence of a P2Y11-like protein in mice (Bourguignon et al., 2019; Prada et al., 2019). In retinal microvessels from rats, a similar P2X7-mediated cell death preventing mechanism due to another P2Y receptor than P2Y11 was shown, namely P2Y4 (Sugiyama et al., 2005). P2Y4 was found to prevent pore formation after ATP induction (Sugiyama et al., 2005), implying that P2Y11 functions might be replaced by the activity of other receptors in species lacking the P2Y11 receptor or, like proposed before, by a P2Y11-like protein.

Ledderose and co-workers (2020) also demonstrated the unique role of P2Y11 on P2X channels. During the formation of an immune synapse, P2Y11 via the cAMP/protein kinase A (PKA) pathway together with P2X4 orchestrates mitochondria to the front of the cell to foster

3 Discussion

localized ATP release to enhance P2X4- and P2X7-mediated Ca^{2+} signaling and cell migration (Ledderose et al., 2020). The P2Y11 receptor is a good example of receptor-dependent differences in human and murine cells. This GPCR influences the sensitivity of the P2X7 receptor and functions with the P2X4 receptor in a cooperative manner. The impact of the receptor on the formation of Ca^{2+} microdomains due to its ability to alter P2X channel function is still unclear since we performed our analysis in murine T cells. Further investigations on the interaction of P2X and P2Y receptors and the formation of P2X-mediated Ca^{2+} microdomains in human CD4^+ T cells are required.

Beside interaction partners of the purinergic channel can differ in murine and human cells, the P2X7 channel, e.g. shows species-dependent structural differences. The P2X7 channel activation kinetics were demonstrated to speed up during repeated stimulation with ATP (McCarthy et al., 2019; Roger et al., 2010). This phenomenon, called channel facilitation, was not due to an increased channel expression at the PM, but due to some biophysical properties of the channel (Roger et al., 2010). The human and rat P2X7 channel differ in channel facilitation. The hP2X7 facilitates slower than the rP2X7. Interestingly, these differences are due to a CaM-binding site in the C-terminal end of the rP2X7, which is absent in the hP2X7 (Roger et al., 2010). The recently published full-length structure of rP2X7 highlights the cytosolic ballast as an important channel compartment for interactions with other proteins (McCarthy et al., 2019). A structural comparison of this region in different species may reveal functional differences between human and other species.

Functional differences were observed here in comparison to previous studies. We performed expression analysis of, e.g. CD69 in P2X4 and P2X7 knockout mice and analyzed the proliferation of CD4^+ T cells (Brock et al., 2022). The expression of CD69, a marker for early T cell activation, was not altered in murine CD4^+ T cells of *P2rx4^{-/-}* and *P2rx7^{-/-}* after TCR/CD3 stimulation, whereas the proliferation of these cells was significantly decreased in T cells of the *P2rx7^{-/-}* mice (Brock et al., 2022). In contrast, in human CD4^+ T cells stimulated with CXCL12, the CD69 expression was significantly decreased after P2X4 inhibition, but not after P2X7 inhibition, while the proliferation of these cells was decreased for both inhibiting conditions (Ledderose et al., 2018). While the different stimuli might trigger these differences, it is also possible that they are species-dependent.

Many studies use knock-out or knock-in mouse models to mimic human diseases. However, drastic functional differences are shown for the P2X2 receptor in humans and mice in response to zinc (Tittle & Hume, 2008), pointing out that the transferability of mouse models on human diseases cannot be generalized.

Species differences were not only observed for purinergic signaling but also Ca^{2+} signaling via SOCE. In T cells of human ORAI1-deficient patients, a complete absence of CRAC currents

3 Discussion

is observed (Feske et al., 2006), whereas mice lacking ORAI1 showed only reduced currents (Gwack et al., 2008). Moreover, STIM1 deficient mice were demonstrated to be resistant to different diseases, e.g. experimental immune thrombocytopenia or acute pneumonitis (Braun et al., 2009), whereas patients with a STIM1 deficiency exhibit these diseases (Picard et al., 2009). These results demonstrate species-dependent differences in the output of ORAI1 and STIM1 deficiency in humans and mice.

Although the results discussed above reveal species-dependent differences in purinergic and Ca^{2+} signaling, many functional results were similar between humans and mice. The approach to analyze the channel- and receptor-mediated signaling using mouse models enhance our knowledge of these pathways and their impact on the immune response. P2X4 and P2X7, e.g. were demonstrated to influence Ca^{2+} signaling in primary murine and human CD4^+ T cells after TCR/CD3 stimulation and in both species, P2X4 but not P2X7 was shown to be implicated in a state of T cell activity prior to TCR/CD3 stimulation (Brock et al., 2022; Ledderose et al., 2018). Additionally, the inhibition of P2X7 decreased in both, mice and humans, the release of proinflammatory cytokines like $\text{IL-1}\beta$ (Danquah et al., 2016).

Moreover, similarities were observed in STIM1 deficient mice and humans in the agonist-selected T cell (e.g., Tregs and NK T cell) development (Fuchs et al., 2012; Oh-Hora et al., 2013; Picard et al., 2009). Comparative analysis of the pathology and signaling pathways of human and mouse data with single-channel deficiencies are essential for clinical trials of related diseases and the development of new therapeutics. Not only the similarities, but also the differences of these data are important to enhance our knowledge of the signaling mechanisms and their influence on immune responses.

3.7 Cell type-specific signaling and channelopathy

Ca^{2+} and ATP are common signaling molecules, influencing cell functions in various cell types. In the study included in this thesis, we used murine CD4^+ T cells to analyze the purinergic-signaling-dependent Ca^{2+} microdomain formation (Brock et al., 2022). These cells exhibit an $\alpha\beta$ TCR heterodimer in their TCR/CD3 complex (Borst et al., 1984). Another T cell subset exhibit the $\gamma\delta$ TCR heterodimer, and thus were named $\gamma\delta$ T cells. $\gamma\delta$ TCRs are less expressed in the circulating T cells of humans; less than 10 % exhibit this TCR subtype (Carding & Egan, 2002). This T cell subset, of which the majority are $\text{V}\gamma 9\text{V}\delta 2^+$, have many innate cell-like features like a fast activation after recognition and the recognition of stress-related non-peptide antigens, like the phosphoantigen (pAg) isopentenyl pyrophosphate (IPP) (Bonneville et al., 2010; Carding & Egan, 2002). The purinergic receptors A2a, P2X4, P2X7 and P2Y11 are highly expressed in these cells (Manohar et al., 2012). Expression analysis of CD69 in $\gamma\delta$ T cells stimulated with anti-CD3/anti-CD28-coated beads and incubated with inhibitors for these

3 Discussion

purinergic receptors reveal no differences compared to the WT. In contrast, after stimulation of the cells with IPP, inhibition with suramin, a non-specific P2 receptor inhibitor, decreased the expression levels of CD69 significantly. In addition, inhibition of P2X4 significantly reduced the expression of TNF- α and INF- γ after stimulation with anti-CD3/anti-CD28-coated beads or IPP, indicating the unique role of P2X4 on the activation of $\gamma\delta$ T cells (Manohar et al., 2012). V γ 9V δ 2⁺ T cells display a delayed and long-lasting Ca²⁺ response compared to conventional CD4⁺ T cells after TCR/CD3 or pAg-mediated stimulation (Nedellec et al., 2010). The restrained and delayed response in V γ 9V δ 2⁺ T cells was sped up and enhanced by the co-stimulation of the activating NK cell receptor (NKG2D) and regulated by a PKC θ transduction pathway (Nedellec et al., 2010). The atypical Ca²⁺ response properties of the V γ 9V δ 2⁺ T cells and the special role of P2X4 above P2X7 on the functions of these cells, reveal differences in activation cascade between $\gamma\delta$ and CD4⁺ T cells.

The activation of B cells was linked to Ca²⁺ signaling via the interaction of STIM and ORAI, comparable to CD4⁺ T cells (Berry et al., 2020). Interestingly, the strength of BCR stimulation controls cell survival, cell-cycle entry and proliferation. While a low BCR stimulation forwarded cell death relative to untreated cells, an increased stimulation strength improved cell viability, cell numbers, the number of dividing cells and the number of divisions per cell (Berry et al., 2020). Thus, Ca²⁺ signaling is related to a variety of functions in different cell types and fine-tuned by similar mechanisms, including, among others, SOCE and ATP-gated P2X channels. Moreover, unraveling the Ca²⁺ signaling network in specific cell types, like in this thesis, the influence of P2X4 and P2X7 on the formation of Ca²⁺ microdomains in CD4⁺ T cells, will increase our understanding of transferable key regulators for other cell types. The extent of the influence of a specific channel or receptor on one or another cell function might vary between the different cell types, but a few of the key players were already extensively analyzed, demonstrating great therapeutic targets treating a wide range of diseases.

Besides the development of channel-specific therapeutic, the identification and analysis of the pathology of diseases related to the deficiency of a specific Ca²⁺ channel are also of great interest. The pathology of such disease is linked to the functional outcomes of channel activity, and therefore increases our knowledge of single-channel specificities. Diseases that contribute to the dysfunction or deficiency of a single ion channel or transporter are called channelopathies (Vaeth & Feske, 2018). The ORAI1 and STIM1 dysfunction-related diseases are collectively called CRAC channelopathy.

CRAC channelopathy is characterized by immunodeficiency, autoimmunity, altered lymphocyte function and non-immune symptoms like congenital muscular hypotonia or ectodermal dysplasia (Lacruz & Feske, 2015; Lian et al., 2018; Picard et al., 2009). Patients with the CRAC channelopathy due to a loss of function mutation or null mutation of *ORAI1*

3 Discussion

have an impaired T cell function, characterized by a defective proliferation after stimulation and diminished cytokine production, e.g., IL-2, IL-22, TNF- α and INF- γ (Lian et al., 2018). These findings are similar to patients with a deficiency in STIM1 (Fuchs et al., 2012; Picard et al., 2009). The immunodeficiency associated with CRAC channelopathy seems to be due to the reduced T cell and not B cell function, since the B cell development and antibody responses are unaffected in mice lacking STIM1 and STIM2 (Matsumoto et al., 2011).

The P2X gene family exhibit a large set of SNPs with gain or loss of functions of the concerning receptor, implicated in various disease. Especially SNPs of the P2X7 channel are investigated intensively (Caseley et al., 2014). The variety of SNPs of a specific P2X channel results in a wide range of disease associations, whereby a generalized phenotype for patients with a, e.g. P2X4 or P2X7 deficiency, like the postulated phenotypes of the CRAC channelopathy, is not defined so far.

The loss of function mutation Y315C in the P2X4 receptor, e.g., was demonstrated to increase pulse pressure in a large white test cohort (Stokes et al., 2011). The same SNP in the *P2rx4* was shown to be implicated in an age-related macular degeneration (AMD). Patients with AMD contain this variant 2-fold more frequently than the healthy control cohort (Gu et al., 2013). This loss of function mutation influences the P2X7-mediated phagocytosis implying an interaction of this P2X4 variant with the P2X7 channel and an effect, especially on macrophages. Additionally, the mutated P2X4 receptor was much less sensitive to ATP (Gu et al., 2013; Stokes et al., 2011). Modeling of the P2X4 Y315C variant reveals that this SNP influences the shape of agonist binding inside the binding pocket for ATP (Stokes et al., 2011). Since this loss of function often occurs in a heterozygous inheritance with the WT P2X4 variant (Stokes et al., 2011), the effects of the SNP might be rescued to some extent. Interestingly, this SNP in the P2X4 channel is sometimes coinherited with a SNP in the P2X7 channel, increasing the effects described for the P2X4 Y315C mutation (Gu et al., 2013).

As mentioned before, SNPs of the P2X7 are quite frequent in the human P2X7 channel leading to various gain or loss of function mutations (Caseley et al., 2014). One SNP of the P2X7 channel was already introduced in this thesis, the amino acid polymorphism at position 451 of the C-terminal tail of the mouse P2X7 channel, influencing P2X7-mediated pore formation (Adriouch et al., 2002), but not Ca²⁺ flux (Le Stunff et al., 2004; Sorge et al., 2012). The SNP variant varies between different mouse strains in its amino acid residue (Pro or Leu) and needs to be considered while working with transgenic mice (Er-Lukowiak et al., 2020). As mentioned above, this SNP was the reason for us to work on the Balb/C mouse background in this thesis (Brock et al., 2022). Additionally, the P451L mutation was examined to be associated with reduced neuropathic and inflammatory pain (Sorge et al., 2012). Accordingly, several other SNPs imply the association of P2X7 with neuropathic and inflammatory pain like the gain of

3 Discussion

function mutations A348T and H155Y (McHugh et al., 2012; Ursu et al., 2014). Moreover, these mutations were mentioned to be related to gender-dependent differences in the prevalence of pain disorders (Ursu et al., 2014). While a pain reduction in the loss of function mutation R270H is controversially discussed (Ursu et al., 2014), a decreased Ca^{2+} flux and pore formation ability were demonstrated. More recent studies investigating the role of R270H in pain intensity and chronic inflammation reduction strengthen the association of P2X7 in this context (Kambur et al., 2018; Sorge et al., 2012).

Another loss of function mutation (homo- and heterozygote), E496A in the C-terminal tail of the P2X7 channel, was three-fold higher in patients with chronic lymphocytic leukemia (CLL) (Wiley et al., 2002) and patients carrying this polymorphism of the 1513C instead of the 1513A allele had a better overall survival (Thunberg et al., 2002). This observation is contrary to the reduced susceptibility of leukemic B cells to undergo ATP-induced apoptosis and the prolonged survival in vivo (Wiley et al., 2002).

The highly variable P2X genes result in a huge set of SNPs with implications in different human diseases. For the *P2rx7* gene, e.g. 32 non-synonymous SNPs were postulated so far (Fuller et al., 2009). The coinheritance of different SNPs of *P2rx7* or SNPs of *P2rx7* and *P2rx4* alter postulated effects of a single SNP (Fuller et al., 2009; Gu et al., 2013), thus resulting in ambiguous pathologies of P2X4- and P2X7-related diseases compared to the clearer pathology of ORAI1/STIM1 deficiencies.

However, the SNPs of the P2X channels are possibly useful as biomarkers for certain diseases. Moreover, combining the pathology of such diseases with molecular analysis of the signaling pathways of single channels will help to identify their physiological role in an organism.

3.8 Outlook

Here, we developed a deconvolution script adjusted for Ca^{2+} imaging sequences and analyzed Ca^{2+} microdomains evoked by the activation of the purinergic ATP-gated channels P2X4 and P2X7.

The new deconvolution script (Woelk et al., 2021) was not used on the data of the measurements of the Ca^{2+} microdomains evoked by P2X4 and P2X7 channel activity (Brock et al., 2022) so far. In future investigations on Ca^{2+} microdomains, the use of this new deconvolution script will computationally increase the resolution of the Ca^{2+} signals and might give new insights into subcellular features of these signals. The implication of RYR1, IP_3R and ORAI1 on the formation of Ca^{2+} microdomains is a well-studied topic of the last decades (Diercks et al., 2018; Trebak & Kinet, 2019; Wolf et al., 2015), whereas the role of P2X channels on the initial formation of Ca^{2+} signals was not established. The activity of P2X4 and

3 Discussion

P2X7 during the first seconds after T cell stimulation highlights their role for the adaptive immune response, although the polymorphic nature of the P2X gene (Caseley et al., 2014; Fuller et al., 2009) appears to impede a clear identification of the channel physiology and pathology. Moreover, stimulus- and cell-type-dependent differences of Ca²⁺ microdomains formation need further investigations which might elucidate channel specifications for a certain stimulus or cell type, like the role of the P2X4 channel in orchestrating the response of $\gamma\delta$ T cells (Manohar et al., 2012).

The thesis established the role of purinergic signaling of PANX1, P2X4 and P2X7 on the initial T cell activation using Ca²⁺ measurements, however the ATP, released via PANX1 and activating the P2X channels, is not visualized in this thesis. Future studies focusing on ATP live-cell imaging during the T cell activation are needed to elucidate the ATP kinetic during cell activation.

Several studies investigated the role of ATP during the cell activation using luciferin/luciferase assays or high-performance liquid chromatography (HPLC) measurements (Burow et al., 2015; Ledderose et al., 2014; Manohar et al., 2012; Yip et al., 2009), hence not reflecting the real-time ATP kinetic at the cell surface during the activation.

Another approach is to bind an ATP sensor to specific cell compartments. One possibility for this approach is to generate fluorescent, genetically-encoded ATP sensors, which can be transfected into cells (Imamura et al., 2009; Pellegatti et al., 2008). The Förster fluorescence resonance energy transfer (FRET)-based ATP indicator ATeam is constructed of the ϵ subunit of the bacterial F₀F₁ ATP synthase linked at the C- and N-terminus with a CFP and YFP. Imamura and co-workers (2009) demonstrated that the ATP affinity of the ATeam is in the high micromolar to the low millimolar range but can be adjusted by substituting the ϵ subunit with that of a different bacteria or by introducing point mutations into the interface between the N- and C- terminal domains of the ϵ subunit. Moreover, the ATeam exhibits a high selectivity for ATP above other nucleoside polyphosphates. For primary cells, the use of genetically-encoded indicators is limited since the transfection of primary cells is challenging and often troubled with a low efficiency and bad cell viability (Kumar et al., 2021; Tay, 2020).

Additionally, chemosensors were developed for measuring the ATP concentrations in cell compartments and at the cell surface. Hence, a promising approach is the use of metal chelators coupled with a chromophore, like the dipicolylamine (DPA)-Zn(II) complex (Kurishita et al., 2012; Moro et al., 2010). The coupling of these complexes to a specific linker enables the sensors to localize in the PM or other cell compartments, like the mitochondria or at the surface of nanoparticles (Kurishita et al., 2012; Ledderose et al., 2018; Moro et al., 2011). One advantage of these chemosensors is the possibility of an “on-line” usage, thus no transfection is needed. The indicators are sensitive in the low micromolar range and sufficient changes in

3 Discussion

the fluorescence intensity are observed for ATP and ADP. These chemosensors also sense (with a lower affinity) other nucleoside polyphosphates, e.g. GTP or UDP (Kurishita et al., 2012; Moro et al., 2011), thus, they are not highly selective for ATP.

A recently published sensor for ATP combines the advantages of the genetically-encoded indicators based on the bacterial F_0F_1 ATP synthase with high selectivity for ATP and the chemosensor with the ability for an “on-line” usage. The so-called ATPOS sensor is based, as mentioned, on the ϵ subunit of a bacterial F_0F_1 ATP synthase, like the ATeam, and enhanced by a cysteine point mutation at which a small-molecule fluorophore is conjugated (Kitajima et al., 2020). It can be linked to the PM of cells via a biotin-streptavidin linkage, thus it can be added to the cells just prior to the measurements. The ATPOS sensor has a high ATP selectivity and a high ATP affinity in the range of high nanomolar to several micromolar. The binding kinetics, association and dissociation, of the ATPOS indicate that the sensor is fast enough to follow ATP dynamics in the time scale of seconds (Kitajima et al., 2020). To this end, the sensor might be a nice tool to analyze spatiotemporally restricted ATP signals after T cell stimulation in future approaches.

References

- Abbas, A. K., Lichtman, A. H., & Pillai, S. (2018). *CELLULAR AND MOLECULAR IMMUNOLOGY*. Elsevier Inc.
- Acuto, O., & Michel, F. (2003). CD28-mediated co-stimulation: A quantitative support for TCR signalling. *Nature Reviews Immunology*, 3(12), 939–951. <https://doi.org/10.1038/nri1248>
- Adriouch, S., Dox, C., Welge, V., Seman, M., Koch-Nolte, F., & Haag, F. (2002). Cutting Edge: A Natural P451L Mutation in the Cytoplasmic Domain Impairs the Function of the Mouse P2X7 Receptor. *The Journal of Immunology*, 169(8), 4108–4112. <https://doi.org/10.4049/jimmunol.169.8.4108>
- Amasaki, Y., Adachi, S., Ishida, Y., Iwata, M., Arai, N., Arai, K. I., & Miyatake, S. (2002). A constitutively nuclear form of NFAT κ shows efficient transactivation activity and induces differentiation of CD4⁺CD8⁺ T cells. *Journal of Biological Chemistry*, 277(28), 25640–25648. <https://doi.org/10.1074/jbc.M201860200>
- Anastasopoulou, M., Gorpas, D., Koch, M., Liapis, E., Glasl, S., Klemm, U., Karlas, A., Lasser, T., & Ntziachristos, V. (2019). Fluorescence imaging reversion using spatially variant deconvolution. *Scientific Reports*, 9(1), 1–11. <https://doi.org/10.1038/s41598-019-54578-0>
- Antonioli, L., Pacher, P., Vizi, E. S., & Haskó, G. (2013). CD39 and CD73 in immunity and inflammation. *Trends in Molecular Medicine*, 19(6), 355–367. <https://doi.org/10.1016/j.molmed.2013.03.005>
- Arigovindan, M., Fung, J. C., Elnatan, D., Mennella, V., Chan, Y. H. M., Pollard, M., Branlund, E., Sedat, J. W., & Agard, D. A. (2013). High-resolution restoration of 3D structures from widefield images with extreme low signal-to-noise-ratio. *Proceedings of the National Academy of Sciences of the United States of America*, 110(43), 17344–17349. <https://doi.org/10.1073/pnas.1315675110>
- Azarashvili, T. S., Odinkova, I. V., Krestinina, O. V., Baburina, Y. L., Grachev, D. E., Teplova, V. V., & Holmuhamedov, E. L. (2011). Role of phosphorylation of porin (VDAC) in regulation of mitochondrial outer membrane under normal conditions and alcohol intoxication. *Biochemistry (Moscow) Supplement Series A: Membrane and Cell Biology*, 5(1), 11–20. <https://doi.org/10.1134/S1990747811010028>
- Benfenati, V., Caprini, M., Nicchia, G. P., Rossi, A., Dovizio, M., Cervetto, C., Nobile, M., & Ferroni, S. (2009). Carbenoxolone inhibits volume-regulated anion conductance in cultured rat cortical astroglia. *Channels*, 3(5). <https://doi.org/10.4161/chan.3.5.9568>
- Berry, C. T., Liu, X., Myles, A., Nandi, S., Chen, Y. H., Hershberg, U., Brodsky, I. E., Cancro, R., & Litt, M. (2013). The P2X7 Receptor Is a Signaling Platform for the Regulation of the Innate Immune Response. *Journal of Biological Chemistry*, 288(12), 8145–8154. <https://doi.org/10.1074/jbc.M112.428000>

References

- M. P., Lengner, C. J., May, M. J., & Freedman, B. D. (2020). BCR-Induced Ca²⁺ Signals Dynamically Tune Survival, Metabolic Reprogramming, and Proliferation of Naive B Cells. *Cell Reports*, *31*(2), 107474. <https://doi.org/10.1016/j.celrep.2020.03.038>
- Birnbaum, M. E., Berry, R., Hsiao, Y. S., Chen, Z., Shingu-Vazquez, M. A., Yu, X., Waghray, D., Fischer, S., McCluskey, J., Rossjohn, J., Walz, T., & Garcia, K. C. (2014). Molecular architecture of the αβ T cell receptor-CD3 complex. *Proceedings of the National Academy of Sciences of the United States of America*, *111*(49), 17576–17581. <https://doi.org/10.1073/pnas.1420936111>
- Blanchard, D. K., Wei, S., Duan, C., Pericle, F., Diaz, J. I., & Djeu, J. Y. (1995). Role of extracellular adenosine triphosphate in the cytotoxic T- lymphocyte-mediated lysis of antigen presenting cells. *Blood*, *85*(11), 3173–3182. <https://doi.org/10.1182/blood.v85.11.3173.bloodjournal85113173>
- Bonneville, M., O'Brien, R. L., & Born, W. K. (2010). γ δ T cell effector functions: A blend of innate programming and acquired plasticity. *Nature Reviews Immunology*, *10*(7), 467–478. <https://doi.org/10.1038/nri2781>
- Bonora, M., Patergnani, S., Rimessi, A., de Marchi, E., Suski, J. M., Bononi, A., Giorgi, C., Marchi, S., Missiroli, S., Poletti, F., Wieckowski, M. R., & Pinton, P. (2012). ATP synthesis and storage. *Purinergic Signalling*, *8*(3), 343–357. <https://doi.org/10.1007/s11302-012-9305-8>
- Bootman, M. D., & Bultynck, G. (2020). Fundamentals of cellular calcium signaling: A primer. *Cold Spring Harbor Perspectives in Biology*, *12*(1). <https://doi.org/10.1101/cshperspect.a038802>
- Borea, P. A., Gessi, S., Merighi, S., Vincenzi, F., & Varani, K. (2018). Pharmacology of adenosine receptors: The state of the art. *Physiological Reviews*, *98*(3), 1591–1625. <https://doi.org/10.1152/physrev.00049.2017>
- Borst, J., Coligan, J. E., Oettgen, H., Pessano, S., Malin, R., & Terhorst, C. (1984). The delta- and epsilon-chains of the human T3/T-cell receptor complex are distinct polypeptides. *Nature*, *312*(5993), 455–458.
- Boumechache, M., Masin, M., Edwardson, J. M., Górecki, D., & Murrell-Lagnado, R. (2009). Analysis of assembly and trafficking of native P2X4 and P2X7 receptor complexes in rodent immune cells. *Journal of Biological Chemistry*, *284*(20), 13446–13454. <https://doi.org/10.1074/jbc.M901255200>
- Bourguignon, T., Benoist, L., Chadet, S., Miquelstorena-Standley, E., Fromont, G., Ivanes, F., & Angoulvant, D. (2019). Stimulation of murine P2Y11-like purinoreceptor protects against hypoxia/reoxygenation injury and decreases heart graft rejection lesions. *Journal of Thoracic and Cardiovascular Surgery*, *158*(3), 780-790.e1.

References

- <https://doi.org/10.1016/j.jtcvs.2018.12.014>
- Bours, M. J. L., Swennen, E. L. R., Di Virgilio, F., Cronstein, B. N., & Dagnelie, P. C. (2006). Adenosine 5'-triphosphate and adenosine as endogenous signaling molecules in immunity and inflammation. *Pharmacology and Therapeutics*, *112*(2), 358–404. <https://doi.org/10.1016/j.pharmthera.2005.04.013>
- Brandman, O., Liou, J., Park, W. S., & Meyer, T. (2007). STIM2 is a feedback regulator that stabilizes basal cytosolic and endoplasmic reticulum Ca²⁺ levels. *Cell*, *131*(7), 1327–1339. <https://doi.org/10.1016/j.cell.2007.11.039>
- Braun, A., Gessner, J. E., David, V. S., Syed, S. N., Konrad, S., Stegner, D., Vögtle, T., Schmidt, R. E., & Nieswandt, B. (2009). STIM1 is essential for Fcγ receptor activation and autoimmune inflammation. *Blood*, *113*(5), 1097–1104. <https://doi.org/10.1182/blood-2008-05-158477>
- Brock, V. J., Wolf, I. M. A., Er-Lukowiak, M., Lory, N., Stähler, T., Woelk, L.-M., Mittrücker, H.-W., Müller, C. E., Koch-nolte, F., Rissiek, B., Werner, R., Guse, A. H., & Diercks, B.-P. (2022). P2X4 and P2X7 are essential players in basal T cell activity and Ca²⁺ signaling milliseconds after T cell activation. *Science Advances*, *8*(5), 1–14. <https://doi.org/10.1126/sciadv.abl9770>
- Brookes, P. S., Yoon, Y., Robotham, J. L., Anders, M. W., & Sheu, S. S. (2004). Calcium, ATP, and ROS: A mitochondrial love-hate triangle. *American Journal of Physiology - Cell Physiology*, *287*(4 56-4). <https://doi.org/10.1152/ajpcell.00139.2004>
- Browne, L. E. (2012). Structure of P2X receptors. *Wiley Interdisciplinary Reviews: Membrane Transport and Signaling*, *1*(1), 56–69. <https://doi.org/10.1002/wmts.24>
- Bruzzo, R., Barbe, M. T., Jakob, N. J., & Monyer, H. (2005). Pharmacological properties of homomeric and heteromeric pannexin hemichannels expressed in *Xenopus* oocytes. *Journal of Neurochemistry*, *92*(5), 1033–1043. <https://doi.org/10.1111/j.1471-4159.2004.02947.x>
- Bu, J. Y., Shaw, A. S., & Chan, A. C. (1995). Analysis of the interaction of ZAP-70 and syk protein-tyrosine kinases with the T-cell antigen receptor by plasmon resonance. *Proceedings of the National Academy of Sciences of the United States of America*, *92*(11), 5106–5110. <https://doi.org/10.1073/pnas.92.11.5106>
- Burnstock, G., & Boeynaems, J. M. (2014). Purinergic signalling and immune cells. *Purinergic Signalling*, *10*(4), 529–564. <https://doi.org/10.1007/s11302-014-9427-2>
- Burow, P., Klapperstück, M., & Markwardt, F. (2015). Activation of ATP secretion via volume-regulated anion channels by sphingosine-1-phosphate in RAW macrophages. *Pflugers Archiv European Journal of Physiology*, *467*(6), 1215–1226. <https://doi.org/10.1007/s00424-014-1561-8>

References

- Cahalan, M. D., & Chandy, K. G. (2009). The functional network of ion channels in T lymphocytes. *Immunological Reviews*, *231*(1), 59–87. <https://doi.org/10.1111/j.1600-065X.2009.00816.x>
- Cárdenas, C., Miller, R. A., Smith, I., Bui, T., Molgó, J., Müller, M., Vais, H., Cheung, K. H., Yang, J., Parker, I., Thompson, C. B., Birnbaum, M. J., Hallows, K. R., & Foskett, J. K. (2010). Essential Regulation of Cell Bioenergetics by Constitutive InsP₃ Receptor Ca²⁺ Transfer to Mitochondria. *Cell*, *142*(2), 270–283. <https://doi.org/10.1016/j.cell.2010.06.007>
- Carding, S. R., & Egan, P. J. (2002). $\gamma\delta$ T cells: Functional plasticity and heterogeneity. *Nature Reviews Immunology*, *2*(5), 336–345. <https://doi.org/10.1038/nri797>
- Caseley, E. A., Muench, S. P., Roger, S., Mao, H. J., Baldwin, S. A., & Jiang, L. H. (2014). Non-synonymous single nucleotide polymorphisms in the P2X receptor genes: Association with diseases, impact on receptor functions and potential use as diagnosis biomarkers. *International Journal of Molecular Sciences*, *15*(8), 13344–13371. <https://doi.org/10.3390/ijms150813344>
- Chambers, J. K., Macdonald, L. E., Sarau, H. M., Ames, R. S., Freeman, K., Foley, J. J., Zhu, Y., McLaughlin, M. M., Murdock, P., McMillan, L., Trill, J., Swift, A., Aiyar, N., Taylor, P., Vawter, L., Naheed, S., Szekeres, P., Hervieu, G., Scott, C., Watson, J. M., Murphy, A. J., Duzic, E., Klein, C., Bergsma, D. J., Wilson, S., & Livi, G. P. (2000). A G protein-coupled receptor for UDP-glucose. *Journal of Biological Chemistry*, *275*(15), 10767–10771. <https://doi.org/10.1074/jbc.275.15.10767>
- Chapman, B. A., & Chang, J. T. (2000). Biopython: Python tools for computational biology. *ACM SIGBIO Newsletter*, *20*(August), 15–19.
- Cook, S. P., & McCleskey, E. W. (2002). Cell damage excites nociceptors through release of cytosolic ATP. *Pain*, *95*(1–2), 41–47. [https://doi.org/10.1016/S0304-3959\(01\)00372-4](https://doi.org/10.1016/S0304-3959(01)00372-4)
- Corriden, R., & Insel, P. A. (2010). Basal release of ATP: An autocrine-paracrine mechanism for cell regulation. *Science Signaling*, *3*(104), 1–13. <https://doi.org/10.1126/scisignal.3104re1>
- Courtney, A. H., Lo, W.-L., & Weiss, A. (2018). TCR Signaling: Mechanisms of Initiation and Propagation. *Trends in Biochemical Sciences*, *43*(2), 108–123. <https://doi.org/10.1016/j.tibs.2017.11.008>
- Dahl, G., Nonner, W., & Werner, R. (1994). Attempts to define functional domains of gap junction proteins with synthetic peptides. *Biophysical Journal*, *67*(5), 1816–1822. [https://doi.org/10.1016/S0006-3495\(94\)80663-0](https://doi.org/10.1016/S0006-3495(94)80663-0)
- Dammermann, W., Zhang, B., Nebel, M., Cordiglieri, C., Odoardi, F., Kirchberger, T., Kawakami, N., Dowden, J., Schmid, F., Dornmair, K., Hohenegger, M., Flügel, A., Guse,

References

- A. H., & Potter, B. V. L. (2009). NAADP-mediated Ca^{2+} signaling via type 1 ryanodine receptor in T cells revealed by a synthetic NAADP antagonist. *Proceedings of the National Academy of Sciences of the United States of America*, *106*(26), 10678–10683. <https://doi.org/10.1073/pnas.0809997106>
- Danquah, W., Catherine, M. S., Rissiek, B., Pinto, C., Arnau, S. P., Amadi, M., Iacenda, D., Knop, J. H., Hammel, A., Bergmann, P., Schwarz, N., Assunção, J., Rotthier, W., Haag, F., Tolosa, E., Bannas, P., Eric, B. G., Magnus, T., Laeremans, T., Stortelers, C., & Friedrich, K. N. (2016). Nanobodies that block gating of the P2X7 ion channel ameliorate inflammation. *Science Translational Medicine*, *8*(366). <https://doi.org/10.1126/scitranslmed.aaf8463>
- Demuro, A., & Parker, I. (2006). Imaging single-channel calcium microdomains. *Cell Calcium*, *40*(5–6), 413–422. <https://doi.org/10.1016/j.ceca.2006.08.006>
- Dey, N., Blanc-Feraud, L., Zimmer, C., Roux, P., Kam, Z., Olivo-Marin, J. C., & Zerubia, J. (2006). Richardson-Lucy algorithm with total variation regularization for 3D confocal microscope deconvolution. *Microscopy Research and Technique*, *69*(4), 260–266. <https://doi.org/10.1002/jemt.20294>
- Di Virgilio, F., Chiozzi, P., Ferrari, D., Falzoni, S., Sanz, J. M., Morelli, A., Torboli, M., Bolognesi, G., & Baricordi, O. R. (2001). Nucleotide receptors: An emerging family of regulatory molecules in blood cells. *Blood*, *97*(3), 587–600. <https://doi.org/10.1182/blood.V97.3.587>
- Diercks, B. P., Werner, R., Schetelig, D., Wolf, I. M. A., & Guse, A. H. (2019). High-resolution calcium imaging method for local calcium signaling. *Methods in Molecular Biology*, *1929*, 27–39. https://doi.org/10.1007/978-1-4939-9030-6_3
- Diercks, B. P., Werner, R., Weidemüller, P., Czarniak, F., Hernandez, L., Lehmann, C., Rosche, A., Krüger, A., Kaufmann, U., Vaeth, M., Failla, A. V., Zobiak, B., Kandil, F. I., Schetelig, D., Ruthenbeck, A., Meier, C., Lodygin, D., Flügel, A., Ren, D., Wolf, I. M. A., Feske, S., & Guse, A. H. (2018). ORA1, STIM1/2, and RYR1 shape subsecond Ca^{2+} microdomains upon T cell activation. *Science Signaling*, *11*(561). <https://doi.org/10.1126/scisignal.aat0358>
- Dosch, M., Gerber, J., Jebbawi, F., & Beldi, G. (2018). Mechanisms of ATP release by inflammatory cells. *International Journal of Molecular Sciences*, *19*(4), 1–16. <https://doi.org/10.3390/ijms19041222>
- Dreisig, K., & Kornum, B. R. (2016). A critical look at the function of the P2Y11 receptor. *Purinergic Signalling*, *12*(3), 427–437. <https://doi.org/10.1007/s11302-016-9514-7>
- Dreisig, K., Sund, L., Dommer, M. W., Kristensen, N. P., Boddum, K., Viste, R., Fredholm, S., Odum, N., Jäättelä, M., Skov, S., & Kornum, B. R. (2018). Human P2Y11 expression level

References

- affects human P2X7 receptor-mediated cell death. *Frontiers in Immunology*, *9*, 1–12. <https://doi.org/10.3389/fimmu.2018.01159>
- Dynes, J. L., Amcheslavsky, A., & Cahalan, M. D. (2016). Genetically targeted single-channel optical recording reveals multiple Orai1 gating states and oscillations in calcium influx. *Proceedings of the National Academy of Sciences of the United States of America*, *113*(2), 440–445. <https://doi.org/10.1073/pnas.1523410113>
- Emrich, S. M., Yoast, R. E., Xin, P., Sneyd, J., Yule, D. I., Emrich, S. M., Yoast, R. E., Xin, P., Arige, V., Wagner, L. E., Hempel, N., & Gill, D. L. (2021). Omnitemporal choreographies of all five STIM/Orai and IP3Rs underlie the complexity of mammalian Ca²⁺ signaling. *CellReports*, *34*(9), 108760. <https://doi.org/10.1016/j.celrep.2021.108760>
- Er-Lukowiak, M., Duan, Y., Rassendren, F., Ulmann, L., Nicke, A., Ufer, F., Friese, M. A., Koch-Nolte, F., Magnus, T., & Rissiek, B. (2020). A *P2rx7* Passenger Mutation Affects the Vitality and Function of T cells in Congenic Mice. *IScience*, *23*(12). <https://doi.org/10.1016/j.isci.2020.101870>
- Erb, L., & Weisman, G. A. (2012). Coupling of P2Y receptors to G proteins and other signaling pathways. *Wiley Interdisciplinary Reviews: Membrane Transport and Signaling*, *1*(6), 789–803. <https://doi.org/10.1002/wmts.62>
- Ettinger, A., & Wittmann, T. (2014). Fluorescence live cell imaging. In *Methods in Cell Biology* (1st ed., Vol. 123). Elsevier Inc. <https://doi.org/10.1016/B978-0-12-420138-5.00005-7>
- Feske, S., Gwack, Y., Prakriya, M., Srikanth, S., Puppel, S. H., Tanasa, B., Hogan, P. G., Lewis, R. S., Daly, M., & Rao, A. (2006). A mutation in Orai1 causes immune deficiency by abrogating CRAC channel function. *Nature*, *441*(7090), 179–185. <https://doi.org/10.1038/nature04702>
- Flögel, U., Burghoff, S., Van Lent, P. L. E. M., Temme, S., Galbarz, L., Ding, Z., El-Tayeb, A., Huels, S., Bönner, F., Borg, N., Jacoby, C., Müller, C. E., Van Den Berg, W. B., & Schrader, J. (2012). Selective activation of adenosine A2A receptors on immune cells by a CD73-dependent prodrug suppresses joint inflammation in experimental rheumatoid arthritis. *Science Translational Medicine*, *4*(146), 2–10. <https://doi.org/10.1126/scitranslmed.3003717>
- Frascoli, M., Marcandalli, J., Schenk, U., & Grassi, F. (2012). Purinergic P2X7 Receptor Drives T Cell Lineage Choice and Shapes Peripheral $\gamma\delta$ Cells. *The Journal of Immunology*, *189*(1), 174–180. <https://doi.org/10.4049/jimmunol.1101582>
- Fuchs, S., Rensing-Ehl, A., Speckmann, C., Bengsch, B., Schmitt-Graeff, A., Bondzio, I., Maul-Pavicic, A., Bass, T., Vraetz, T., Strahm, B., Ankermann, T., Benson, M., Caliebe, A., Fölster-Holst, R., Kaiser, P., Thimme, R., Schamel, W. W., Schwarz, K., Feske, S., & Ehl, S. (2012). Antiviral and Regulatory T Cell Immunity in a Patient with Stromal Interaction

References

- Molecule 1 Deficiency. *The Journal of Immunology*, 188(3), 1523–1533. <https://doi.org/10.4049/jimmunol.1102507>
- Fuller, S. J., Stokes, L., Skarratt, K. K., Gu, B. J., & Wiley, J. S. (2009). Genetics of the P2X7 receptor and human disease. *Purinergic Signalling*, 5(2), 257–262. <https://doi.org/10.1007/s11302-009-9136-4>
- Garçon, F., Patton, D. T., Emery, J. L., Hirsch, E., Rottapel, R., Sasaki, T., & Okkenhaug, K. (2008). CD28 provides T-cell costimulation and enhances PI3K activity at the immune synapse independently of its capacity to interact with the p85/p110 heterodimer. *Blood*, 111(3), 1464–1471. <https://doi.org/10.1182/blood-2007-08-108050>
- Gazzerro, E., Baratto, S., Assereto, S., Baldassari, S., Panicucci, C., Raffaghello, L., Scudieri, P., De Battista, D., Fiorillo, C., Volpi, S., Chaabane, L., Malnati, M., Messina, G., Bruzzone, S., Traggiai, E., Grassi, F., Minetti, C., & Bruno, C. (2019). The Danger Signal Extracellular ATP Is Involved in the Immunomediated Damage of α -Sarcoglycan-Deficient Muscular Dystrophy. *American Journal of Pathology*, 189(2), 354–369. <https://doi.org/10.1016/j.ajpath.2018.10.008>
- Gil-Hernández, A., Arroyo-Campuzano, M., Simoni-Nieves, A., Zazueta, C., Gomez-Quiroz, L. E., & Silva-Palacios, A. (2021). Relevance of Membrane Contact Sites in Cancer Progression. *Frontiers in Cell and Developmental Biology*, 8(January), 1–19. <https://doi.org/10.3389/fcell.2020.622215>
- Gil, D., Guse, A. H., & Dupont, G. (2021). Three-Dimensional Model of Sub-Plasmalemmal Ca^{2+} Microdomains Evoked by the Interplay Between ORAI1 and InsP_3 Receptors. *Frontiers in Immunology*, 12(April), 1–15. <https://doi.org/10.3389/fimmu.2021.659790>
- Grassi, F. (2020). The P2X7 Receptor as Regulator of T Cell Development and Function. *Frontiers in Immunology*, 11(June), 2–7. <https://doi.org/10.3389/fimmu.2020.01179>
- Grynkiewicz, G., Poenie, M., & Tsien, R. Y. (1985). A new generation of Ca^{2+} indicators with greatly improved fluorescence properties. *Journal of Biological Chemistry*, 260(6), 3440–3450. [https://doi.org/10.1016/s0021-9258\(19\)83641-4](https://doi.org/10.1016/s0021-9258(19)83641-4)
- Gu, B. J., Baird, P. N., Vessey, K. A., Skarratt, K. K., Fletcher, E. L., Fuller, S. J., Richardson, A. J., Guymer, R. H., & Wiley, J. S. (2013). A rare functional haplotype of the *P2RX4* and *P2RX7* genes leads to loss of innate phagocytosis and confers increased risk of age-related macular degeneration. *FASEB Journal*, 27(4), 1479–1487. <https://doi.org/10.1096/fj.12-215368>
- Gu, F., Krüger, A., Roggenkamp, H. G., Alpers, R., Lodygin, D., Jaquet, V., Möckl, F., Hernandez C., L. C., Winterberg, K., Bauche, A., Rosche, A., Grasberger, H., Kao, J. Y., Schetelig, D., Werner, R., Schröder, K., Carty, M., Bowie, A. G., Huber, S., Meier, C., Mittrücker, H.-W., Heeren, J., Krause, K.-H., Flügel, A., Diercks, B.-P., & Guse, A. H.

References

- (2021). Dual NADPH oxidases DUOX1 and DUOX2 synthesize NAADP and are necessary for Ca²⁺ signaling during T cell activation . *Science Signaling*, 14(709). <https://doi.org/10.1126/scisignal.abe3800>
- Gudlur, A., Zeraik, A. E., Hirve, N., & Hogan, P. G. (2020). STIM calcium sensing and conformational change. *The Journal of Physiology*, 598(9), 1695–1705. <https://doi.org/10.1113/JP276524>
- Gunaratne, G. S., Brailoiu, E., He, S., Unterwald, E. M., Patel, S., Slama, J. T., Walseth, T. F., & Marchant, J. S. (2021). Essential requirement for JPT2 in NAADP-evoked Ca²⁺ signaling. *Science Signaling*, 14(675). <https://doi.org/10.1126/scisignal.abd5605>
- Guse, A. H., Gil Montoya, D. C., & Diercks, B. P. (2021). Mechanisms and functions of calcium microdomains produced by ORAI channels, D-myo-inositol 1,4,5-trisphosphate receptors, or ryanodine receptors. *Pharmacology and Therapeutics*, 223, 107804. <https://doi.org/10.1016/j.pharmthera.2021.107804>
- Gwack, Y., Srikanth, S., Oh-hora, M., Hogan, P. G., Lamperti, E. D., Yamashita, M., Gelinas, C., Neems, D. S., Sasaki, Y., Feske, S., Prakriya, M., Rajewsky, K., & Rao, A. (2008). Hair Loss and Defective T- and B-Cell Function in Mice Lacking ORAI1. *Molecular and Cellular Biology*, 28(17), 5209–5222. <https://doi.org/10.1128/mcb.00360-08>
- Habermacher, C., Dunning, K., Chataigneau, T., & Grutter, T. (2016). Molecular structure and function of P2X receptors. *Neuropharmacology*, 104, 18–30. <https://doi.org/10.1016/j.neuropharm.2015.07.032>
- Hammad, A. S., & Machaca, K. (2021). Store operated calcium entry in cell migration and cancer metastasis. *Cells*, 10(5), 1–19. <https://doi.org/10.3390/cells10051246>
- Handa, M., & Guidotti, G. (1996). Purification and cloning of a soluble ATP-diphosphohydrolase (Apyrase) from potato tubers (*Solanum tuberosum*). *Biochemical and Biophysical Research Communications*, 218(3), 916–923. <https://doi.org/10.1006/bbrc.1996.0162>
- Harwood, N. E., & Batista, F. D. (2010). Early events in B cell activation. *Annual Review of Immunology*, 28, 185–210. <https://doi.org/10.1146/annurev-immunol-030409-101216>
- Hattori, M., & Gouaux, E. (2012). Molecular mechanism of ATP binding and ion channel activation in P2X receptors. *Nature*, 485(7397), 207–212. <https://doi.org/10.1038/nature11010>
- He, M. L., Gonzalez-Iglesias, A. E., Tomic, M., & Stojilkovic, S. S. (2005). Release and extracellular metabolism of ATP by ecto-nucleotidase eNTPDase 1-3 in hypothalamic and pituitary cells. *Purinergic Signalling*, 1(2), 135–144. <https://doi.org/10.1007/s11302-005-6208-y>
- Hirve, N., Rajanikanth, V., Hogan, P. G., & Gudlur, A. (2018). Coiled-Coil Formation Conveys

References

- a STIM1 Signal from ER Lumen to Cytoplasm. *Cell Reports*, 22(1), 72–83. <https://doi.org/10.1016/j.celrep.2017.12.030>
- Horenstein, A. L., Chillemi, A., Zaccarello, G., Bruzzone, S., Quarona, V., Zito, A., Serra, S., & Malavasi, F. (2013). A CD38/CD203A/CD73 ectoenzymatic pathway independent of CD39 drives a novel adenosinergic loop in human T lymphocytes. *Oncot Immunology*, 2(9), 1–14. <https://doi.org/10.4161/onci.26246>
- Hoth, M., Fanger, C. M., & Lewis, R. S. (1997). Mitochondrial regulation of store-operated calcium signaling in T lymphocytes. *Journal of Cell Biology*, 137(3), 633–648. <https://doi.org/10.1083/jcb.137.3.633>
- Hou, Z., & Cao, J. (2016). Comparative study of the P2X gene family in animals and plants. *Purinergic Signalling*, 12(2), 269–281. <https://doi.org/10.1007/s11302-016-9501-z>
- Hwang, J. R., Byeon, Y., Kim, D., & Park, S. G. (2020). Recent insights of T cell receptor-mediated signaling pathways for T cell activation and development. *Experimental and Molecular Medicine*, 52(5), 750–761. <https://doi.org/10.1038/s12276-020-0435-8>
- Imamura, H., Huynh Nhat, K. P., Togawa, H., Saito, K., Iino, R., Kato-Yamada, Y., Nagai, T., & Noji, H. (2009). Visualization of ATP levels inside single living cells with fluorescence resonance energy transfer-based genetically encoded indicators. *Proceedings of the National Academy of Sciences of the United States of America*, 106(37), 15651–15656. <https://doi.org/10.1073/pnas.0904764106>
- Imura, Y., Morizawa, Y., Komatsu, R., Shibata, K., Shinozaki, Y., Kasai, H., Moriishi, K., Moriyama, Y., & Koizumi, S. (2013). Microglia release ATP by exocytosis. *Glia*, 61(8), 1320–1330. <https://doi.org/10.1002/glia.22517>
- Islam, M. R., Uramoto, H., Okada, T., Sabirov, R. Z., & Okada, Y. (2012). Maxi-anion channel and pannexin 1 hemichannel constitute separate pathways for swelling-induced ATP release in murine L929 fibrosarcoma cells. *American Journal of Physiology - Cell Physiology*, 303(9), 924–935. <https://doi.org/10.1152/ajpcell.00459.2011>
- Islam, M. S. (2020). Calcium Signaling: From Basic to Bedside. *Advances in Experimental Medicine and Biology*, 1131, 1–6. https://doi.org/10.1007/978-3-030-12457-1_1
- Jacobson, K. A., Jayasekara, M. P. S., & Costanzi, S. (2012). Molecular Structure of P2Y Receptors: Mutagenesis, Modeling, and Chemical Probes. *Wiley Interdiscip Rev Membr Transp Signal*, 1(6). <https://doi.org/10.1002/wmts.68>
- Jain, J., McCaffrey, P. G., Valge-Archer, V. E., & Rao, A. (1992). Nuclear factor of activated T cells contains Fos and Jun. *Nature*, 356, 801–804. <https://doi.org/10.1016/B978-0-12-394447-4.30088-8>
- Jentsch, T. J. (2016). VRACs and other ion channels and transporters in the regulation of cell volume and beyond. *Nature Reviews Molecular Cell Biology*, 17(5), 293–307.

References

- <https://doi.org/10.1038/nrm.2016.29>
- Junger, W. G. (2011). Immune cell regulation by autocrine purinergic signalling. *Nature Reviews Immunology*, *11*(3), 201–212. <https://doi.org/10.1038/nri2938>
- Kaczmarek-Hájek, K., Lőrinczi, É., Hausmann, R., & Nicke, A. (2012). Molecular and functional properties of P2X receptors-recent progress and persisting challenges. *Purinergic Signalling*, *8*(3), 375–417. <https://doi.org/10.1007/s11302-012-9314-7>
- Kambur, O., Kaunisto, M. A., Winsvold, B. S., Wilsgaard, T., Stubhaug, A., Zwart, J. A., Kalso, E., & Nielsen, C. S. (2018). Genetic variation in *P2RX7* and pain tolerance. *Pain*, *159*(6), 1064–1073. <https://doi.org/10.1097/j.pain.0000000000001188>
- Kang, M. G. (1998). Generalized multichannel image deconvolution approach and its applications. *Optical Engineering*, *37*(11), 2953. <https://doi.org/10.1117/1.601883>
- Kar, P., Nelson, C., & Parekh, A. B. (2011). Selective activation of the transcription factor NFAT1 by calcium microdomains near Ca²⁺ release-activated Ca²⁺ (CRAC) channels. *Journal of Biological Chemistry*, *286*(17), 14795–14803. <https://doi.org/10.1074/jbc.M111.220582>
- Kawano, S., Otsu, K., Kuruma, A., Shoji, S., Yanagida, E., Muto, Y., Yoshikawa, F., Hirayama, Y., Mikoshiba, K., & Furuichi, T. (2006). ATP autocrine/paracrine signaling induces calcium oscillations and NFAT activation in human mesenchymal stem cells. *Cell Calcium*, *39*(4), 313–324. <https://doi.org/10.1016/j.ceca.2005.11.008>
- Kawate, T., Michel, J. C., Birdsong, W. T., & Gouaux, E. (2009). Crystal structure of the ATP-gated P2X4 ion channel in the closed state. *Nature*, *460*(7255), 592–598. <https://doi.org/10.1038/nature08198>
- Kitajima, N., Takikawa, K., Sekiya, H., Satoh, K., Asanuma, D., Sakamoto, H., Takahashi, S., Hanaoka, K., Urano, Y., Namiki, S., Iino, M., & Hirose, K. (2020). Real-time in vivo imaging of extracellular ATP in the brain with a hybrid-type fluorescent sensor. *ELife*, *9*, 1–18. <https://doi.org/10.7554/eLife.57544>
- Kolen, K., & Slegers, H. (2006). Integration of P2Y receptor-activated signal transduction pathways in G protein-dependent signalling networks. *Purinergic Signalling*, *2*(3), 451–469. <https://doi.org/10.1007/s11302-006-9008-0>
- Kopp, R., Krautloher, A., Ramírez-Fernández, A., & Nicke, A. (2019). P2X7 Interactions and Signaling – Making Head or Tail of It. *Frontiers in Molecular Neuroscience*, *12*(August), 1–25. <https://doi.org/10.3389/fnmol.2019.00183>
- Kumar, A. R. K., Shou, Y., Chan, B., Krishaa, L., & Tay, A. (2021). Materials for Improving Immune Cell Transfection. *Advanced Materials*, *33*(21), 1–21. <https://doi.org/10.1002/adma.202007421>
- Kurishita, Y., Kohira, T., Ojida, A., & Hamachi, I. (2012). Organelle-localizable fluorescent

References

- chemosensors for site-specific multicolor imaging of nucleoside polyphosphate dynamics in living cells. *Journal of the American Chemical Society*, *134*(45), 18779–18789. <https://doi.org/10.1021/ja308754g>
- Lacruz, R. S., & Feske, S. (2015). Diseases caused by mutations in ORAI1 and STIM1. *Annals of the New York Academy of Sciences*, *1356*(1), 45–79. <https://doi.org/10.1111/nyas.12938>
- Le Duc, D., Schulz, A., Lede, V., Schulze, A., Thor, D., Brüser, A., & Schöneberg, T. (2017). P2Y Receptors in Immune Response and Inflammation. *Advances in Immunology*, *136*, 85–121. <https://doi.org/10.1016/bs.ai.2017.05.006>
- Le Stunff, H., Auger, R., Kanellopoulos, J., & Raymond, M. N. (2004). The Pro-451 to Leu Polymorphism within the C-terminal Tail of P2X7 Receptor Impairs Cell Death but Not Phospholipase D Activation in Murine Thymocytes. *Journal of Biological Chemistry*, *279*(17), 16918–16926. <https://doi.org/10.1074/jbc.M313064200>
- Ledderose, C., Bao, Y., Lidicky, M., Zipperle, J., Li, L., Strasser, K., Shapiro, N. I., & Junger, W. G. (2014). Mitochondria are gate-keepers of T cell function by producing the ATP that drives purinergic signaling. *Journal of Biological Chemistry*, *289*(37), 25936–25945. <https://doi.org/10.1074/jbc.M114.575308>
- Ledderose, C., Bromberger, S., Slubowski, C. J., Sueyoshi, K., & Junger, W. G. (2020). Frontline Science: P2Y11 receptors support T cell activation by directing mitochondrial trafficking to the immune synapse. *Journal of Leukocyte Biology*, *109*, 497–508. <https://doi.org/10.1002/JLB.2HI0520-191R>
- Ledderose, C., Liu, K., Kondo, Y., Slubowski, C. J., Dertnig, T., Denicoló, S., Arbab, M., Hubner, J., Konrad, K., Fakhari, M., Lederer, J. A., Robson, S. C., Visner, G. A., & Junger, W. G. (2018). Purinergic P2X4 receptors and mitochondrial ATP production regulate T cell migration. *Journal of Clinical Investigation*, *128*(8), 3583–3594. <https://doi.org/10.1172/JCI120972>
- Li, M., Silberberg, S. D., & Swartz, K. J. (2013). Subtype-specific control of P2X receptor channel signaling by ATP and Mg²⁺. *Proceedings of the National Academy of Sciences of the United States of America*, *110*(36), E3455–E3463. <https://doi.org/10.1073/pnas.1308088110>
- Lian, J., Cuk, M., Kahlfuss, S., Kozhaya, L., Vaeth, M., Rieux-Laucat, F., Picard, C., Benson, M. J., Jakovcevic, A., Bilic, K., Martinac, I., Stathopoulos, P., Kacs Kovics, I., Vraetz, T., Speckmann, C., Ehl, S., Issekutz, T., Unutmaz, D., & Feske, S. (2018). ORAI1 mutations abolishing store-operated Ca²⁺ entry cause anhidrotic ectodermal dysplasia with immunodeficiency. *Journal of Allergy and Clinical Immunology*, *142*(4), 1297–1310.e11. <https://doi.org/10.1016/j.jaci.2017.10.031>

References

- Lin, Y. S., Lin, Y. H., Thi, M. N., Hsiao, S. C., & Chiu, W. T. (2022). STIM1 controls the focal adhesion dynamics and cell migration by regulating SOCE in osteosarcoma. *International Journal of Molecular Sciences*, *23*(1). <https://doi.org/10.3390/ijms23010162>
- Linden, J., Koch-Nolte, F., & Dahl, G. (2019). Purine Release, Metabolism, and Signaling in the Inflammatory Response. *Annual Review of Immunology*, *37*(1), 325–347. <https://doi.org/10.1146/annurev-immunol-051116-052406>
- Liou, J., Kim, M. L., Heo, W. Do, Jones, J. T., Myers, J. W., Ferrell Jr, J. E., & Meyer, T. (2005). STIM Is a Ca²⁺ Sensor Essential for Ca²⁺-Store-Depletion-Triggered Ca²⁺ Influx. *Current Biology*, *15*(13), 1235–1241. <https://doi.org/10.1016/j.cub.2005.05.055>
- Lohman, A. W., & Isakson, B. E. (2014). Differentiating connexin hemichannels and pannexin channels in cellular ATP release. *FEBS Letters*, *588*(8), 1379–1388. <https://doi.org/10.1016/j.febslet.2014.02.004>
- Lu, F., Sun, J., Zheng, Q., Li, J., Hu, Y., Yu, P., He, H., Zhao, Y., Wang, X., Yang, S., & Cheng, H. (2019). Imaging elemental events of store-operated Ca²⁺ entry in invading cancer cells with plasmalemmal targeted sensors. *Journal of Cell Science*, *132*(6). <https://doi.org/10.1242/jcs.224923>
- Ma, Z., Tanis, J. E., Taruno, A., & Foskett, J. K. (2016). Calcium homeostasis modulator (CALHM) ion channels. *Pflügers Archiv European Journal of Physiology*, *468*(3), 395–403. <https://doi.org/10.1007/s00424-015-1757-6>
- Macian, F. (2005). NFAT proteins: Key regulators of T-cell development and function. *Nature Reviews Immunology*, *5*(6), 472–484. <https://doi.org/10.1038/nri1632>
- Mank, M., & Griesbeck, O. (2008). Genetically encoded calcium indicators. *Chemical Reviews*, *108*(5), 1550–1564. <https://doi.org/10.1021/cr078213v>
- Manohar, M., Hirsh, M. I., Chen, Y., Woehrle, T., Karande, A. A., & Junger, W. G. (2012). ATP release and autocrine signaling through P2X4 receptors regulate $\gamma\delta$ T cell activation. *Journal of Leukocyte Biology*, *92*(4), 787–794. <https://doi.org/10.1189/jlb.0312121>
- Mansoor, S. E., Lü, W., Oosterheert, W., Shekhar, M., Tajkhorshid, E., & Gouaux, E. (2016). X-ray structures define human P2X3 receptor gating cycle and antagonist action. *Nature*, *538*(7623), 66–71. <https://doi.org/10.1038/nature19367>
- Mariuzza, R. A., Agnihotri, P., & Orban, J. (2020). The structural basis of T-cell receptor (TCR) activation: An enduring enigma. *Journal of Biological Chemistry*, *295*(4), 914–925. <https://doi.org/10.1074/jbc.REV119.009411>
- Markham, J. (1999). Parametric blind deconvolution: a robust method for the simultaneous estimation of image and blur. *Optical Society of America*, *16*(10), 2377–2391.
- Markwardt, F. (2021). Human P2X7 receptors – Properties of single ATP-gated ion channels. *Biochemical Pharmacology*, *187*, 114307. <https://doi.org/10.1016/j.bcp.2020.114307>

References

- Masopust, D., & Schenkel, J. M. (2013). The integration of T cell migration, differentiation and function. *Nature Reviews Immunology*, *13*(5), 309–320. <https://doi.org/10.1038/nri3442>
- Matsumoto, M., Fujii, Y., Baba, A., Hikida, M., Kurosaki, T., & Baba, Y. (2011). The Calcium Sensors STIM1 and STIM2 Control B Cell Regulatory Function through Interleukin-10 Production. *Immunity*, *34*(5), 703–714. <https://doi.org/10.1016/j.immuni.2011.03.016>
- McCarthy, A. E., Yoshioka, C., & Mansoor, S. E. (2019). Full-Length P2X7 Structures Reveal How Palmitoylation Prevents Channel Desensitization. *Cell*, *179*(3), 659-670.e13. <https://doi.org/10.1016/j.cell.2019.09.017>
- McHugh, S. M., Roman, S., Davis, B., Koch, A., Pickett, A. M., Richardson, J. C., Miller, S. R., Wetten, S., Cox, C. J., Karpe, F., Todd, J. A., & Bullmore, E. T. (2012). Effects of genetic variation in the *P2RX7* gene on pharmacodynamics of a P2X 7 receptor antagonist: A prospective genotyping approach. *British Journal of Clinical Pharmacology*, *74*(2), 376–380. <https://doi.org/10.1111/j.1365-2125.2012.04200.x>
- McNally, J. G., Karpova, T., Cooper, J., & Conchello, J. A. (1999). Three-dimensional imaging by deconvolution microscopy. *Methods: A Companion to Methods in Enzymology*, *19*(3), 373–385. <https://doi.org/10.1006/meth.1999.0873>
- Meldolesi, J. (2004). The development of Ca²⁺ indicators: A breakthrough in pharmacological research. *Trends in Pharmacological Sciences*, *25*(4), 172–174. <https://doi.org/10.1016/j.tips.2004.02.004>
- Moreschi, I., Bruzzone, S., Bodrato, N., Usai, C., Guida, L., Nicholas, R. A., Kassack, M. U., Zocchi, E., & De Flora, A. (2008). NAADP⁺ is an agonist of the human P2Y₁₁ purinergic receptor. *Cell Calcium*, *43*(4), 344–355. <https://doi.org/10.1016/j.ceca.2007.06.006>
- Moreschi, I., Bruzzone, S., Nicholas, R. A., Fruscione, F., Sturla, L., Benvenuto, F., Usai, C., Meis, S., Kassack, M. U., Zocchi, E., & De Flora, A. (2006). Extracellular NAD⁺ Is an Agonist of the Human P2Y₁₁ Purinergic Receptor in Human Granulocytes. *Journal of Biological Chemistry*, *281*(42), 31419–31429. [https://doi.org/10.1016/s0021-9258\(19\)84054-1](https://doi.org/10.1016/s0021-9258(19)84054-1)
- Moro, A. J., Cywinski, P. J., Körsten, S., & Mohr, G. J. (2010). An ATP fluorescent chemosensor based on a Zn(ii)-complexed dipicolylamine receptor coupled with a naphthalimide chromophore. *Chemical Communications*, *46*(7), 1085–1087. <https://doi.org/10.1039/b919661g>
- Moro, A. J., Schmidt, J., Doussineau, T., Lapresta-Fernandéz, A., Wegener, J., & Mohr, G. J. (2011). Surface-functionalized fluorescent silica nanoparticles for the detection of ATP. *Chemical Communications*, *47*(21), 6066–6068. <https://doi.org/10.1039/c1cc10419e>
- Müller, C. E., & Jacobson, K. A. (2011). Recent developments in adenosine receptor ligands and their potential as novel drugs. *Biochimica et Biophysica Acta - Biomembranes*,

References

- 1808(5), 1290–1308. <https://doi.org/10.1016/j.bbamem.2010.12.017>
- Murphy, K., Travers, P., & Walport, M. (2009). Janeway Immunologie. In *Janeway Immunologie*. <https://doi.org/10.1007/978-3-8274-2219-4>
- Nedellec, S., Sabourin, C., Bonneville, M., & Scotet, E. (2010). NKG2D Costimulates Human V γ 9V δ 2 T Cell Antitumor Cytotoxicity through Protein Kinase C θ -Dependent Modulation of Early TCR-Induced Calcium and Transduction Signals. *The Journal of Immunology*, 185(1), 55–63. <https://doi.org/10.4049/jimmunol.1000373>
- Neves, S. R., Ram, P. T., & Iyengar, R. (2002). G protein pathways. *Science*, 296(5573), 1636–1639. <https://doi.org/10.1126/science.1071550>
- North, R. A. (2002). Molecular physiology of P2X receptors. *Physiological Reviews*, 82(4), 1013–1067. <https://doi.org/10.1152/physrev.00015.2002>
- Oh-Hora, M., Komatsu, N., Pishyareh, M., Feske, S., Hori, S., Taniguchi, M., Rao, A., & Takayanagi, H. (2013). Agonist-Selected T Cell Development Requires Strong T Cell Receptor Signaling and Store-Operated Calcium Entry. *Immunity*, 38(5), 881–895. <https://doi.org/10.1016/j.immuni.2013.02.008>
- Oliveria, S. F., Dell'Acqua, M. L., & Sather, W. A. (2007). AKAP79/150 Anchoring of Calcineurin Controls Neuronal L-Type Ca²⁺ Channel Activity and Nuclear Signaling. *Neuron*, 55(2), 261–275. <https://doi.org/10.1016/j.neuron.2007.06.032>
- Oshima, A. (2014). Structure and closure of connexin gap junction channels. *FEBS Letters*, 588(8), 1230–1237. <https://doi.org/10.1016/j.febslet.2014.01.042>
- Oviedo-Orta, E., Hoy, T., & Evans, W. H. (2000). Intercellular communication in the immune system: Differential expression of connexin40 and 43, and perturbation of gap junction channel functions in peripheral blood and tonsil human lymphocyte subpopulations. *Immunology*, 99(4), 578–590. <https://doi.org/10.1046/j.1365-2567.2000.00991.x>
- Pankratov, Y., Lalo, U., Verkhratsky, A., & North, R. A. (2007). Quantal release of ATP in mouse cortex. *Journal of General Physiology*, 129(3), 257–265. <https://doi.org/10.1085/jgp.200609693>
- Pellegatti, P., Raffaghello, L., Bianchi, G., Piccardi, F., Pistoia, V., & Di Virgilio, F. (2008). Increased level of extracellular ATP at tumor sites: In vivo imaging with plasma membrane luciferase. *PLoS ONE*, 3(7), 1–9. <https://doi.org/10.1371/journal.pone.0002599>
- Petrenko, N., Khafizov, K., Tvrdonova, V., Skorinkin, A., & Giniatullin, R. (2011). Role of the ectodomain serine 275 in shaping the binding pocket of the ATP-gated P2X3 receptor. *Biochemistry*, 50(39), 8427–8436. <https://doi.org/10.1021/bi200812u>
- Pettmann, J., Santos, A. M., Dushek, O., & Davis, S. J. (2018). Membrane ultrastructure and T cell activation. *Frontiers in Immunology*, 9(SEP), 1–9. <https://doi.org/10.3389/fimmu.2018.02152>

References

- Picard, C., McCarl, C.-A., Papolos, A., Khalil, S., Lüthy, K., Hivroz, C., LeDeist, F., Rieux-Laucat, F., Rechavi, G., Rao, A., Fischer, A., & Feske, S. (2009). STIM1 Mutation Associated with a Syndrome of Immunodeficiency and Autoimmunity. *The New England Journal of Medicine*, *360*(19), 1971–1980.
- Poggio, T., Voorhees, H., & Yuille, A. (1988). A regularized solution to edge detection. *Journal of Complexity*, *4*(2), 106–123. [https://doi.org/10.1016/0885-064X\(88\)90024-6](https://doi.org/10.1016/0885-064X(88)90024-6)
- Prada, M. P., Syed, A. U., Buonarati, O. R., Reddy, G. R., Nystoriak, M. A., Ghosh, D., Simó, S., Sato, D., Sasse, K. C., Ward, S. M., Santana, L. F., Xiang, Y. K., Hell, J. W., Nieves-Cintrón, M., & Navedo, M. F. (2019). A Gs-coupled purinergic receptor boosts Ca²⁺ influx and vascular contractility during diabetic hyperglycemia. *ELife*, *8*, 1–37. <https://doi.org/10.7554/eLife.42214>
- Prasai, P., Stefos, G. C., & Becker, W. (2011). Extracellular ATP activates NFAT-dependent gene expression in neuronal PC12 cells via P2X receptors. *BMC Neuroscience*, *12*(1), 90. <https://doi.org/10.1186/1471-2202-12-90>
- Pulte, E. D., Broekman, M. J., Olson, K. E., Drosopoulos, J. H. F., Kizer, J. R., Islam, N., & Marcus, A. J. (2007). CD39/NTPDase-1 activity and expression in normal leukocytes. *Thrombosis Research*, *121*(3), 309–317. <https://doi.org/10.1016/j.thromres.2007.04.008>
- Rengarajan, J., Mowen, K. A., McBride, K. D., Smith, E. D., Singh, H., & Glimcher, L. H. (2002). Interferon regulatory factor 4 (IRF4) interacts with NFATc2 to modulate interleukin 4 gene expression. *Journal of Experimental Medicine*, *195*(8), 1003–1012. <https://doi.org/10.1084/jem.20011128>
- Rivas-Yáñez, E., Barrera-Avalos, C., Parra-Tello, B., Briceño, P., Roseblatt, M. V., Saavedra-Almarza, J., Roseblatt, M., Acuña-Castillo, C., Bono, M. R., & Sauma, D. (2020). P2X7 receptor at the crossroads of T cell fate. *International Journal of Molecular Sciences*, *21*(14), 1–22. <https://doi.org/10.3390/ijms21144937>
- Roger, S., Gillet, L., Baroja-Mazo, A., Surprenant, A., & Pelegrin, P. (2010). C-terminal calmodulin-binding motif differentially controls human and rat P2X7 receptor current facilitation. *Journal of Biological Chemistry*, *285*(23), 17514–17524. <https://doi.org/10.1074/jbc.M109.053082>
- Roggenkamp, H. G., Khansahib, I., Hernandez, C. L. C., Zhang, Y., Lodygin, D., Krüger, A., Gu, F., Möckl, F., Löhndorf, A., Wolters, V., Woike, D., Rosche, A., Bauche, A., Schetelig, D., Werner, R., Schlüter, H., Failla, A. V., Meier, C., Fliegert, R., Walseth, T. F., Flügel, A., Diercks, B. P., & Guse, A. H. (2021). HN1L/JPT2: A signaling protein that connects NAADP generation to Ca²⁺ microdomain formation. *Science Signaling*, *14*(675). <https://doi.org/10.1126/scisignal.abd5647>
- Ruan, Z., Orozco, I. J., Du, J., & Lü, W. (2020). Structures of human pannexin 1 reveal ion

References

- pathways and mechanism of gating. *Nature*, 584(7822), 646–651. <https://doi.org/10.1038/s41586-020-2357-y>
- Sage, D., Donati, L., Soulez, F., Fortun, D., Schmit, G., Seitz, A., Guiet, R., Vonesch, C., & Unser, M. (2017). DeconvolutionLab2: An open-source software for deconvolution microscopy. *Methods*, 115(2017), 28–41. <https://doi.org/10.1016/j.ymeth.2016.12.015>
- Sarder, P., & Nehorai, A. (2006). Deconvolution methods for 3-D fluorescence microscopy images. *IEEE Signal Processing Magazine*, 23(3), 32–45. <https://doi.org/10.1109/MSP.2006.1628876>
- Schaefer, L. H., Schuster, D., & Herz, H. (2001). Generalized approach for accelerated maximum likelihood based image restoration applied to three-dimensional fluorescence microscopy. *Journal of Microscopy*, 204(2), 99–107. <https://doi.org/10.1046/j.1365-2818.2001.00949.x>
- Schelten, K., Nowozin, S., Jancsary, J., Rother, C., & Roth, S. (2015). Interleaved regression tree field cascades for blind image deconvolution. *Proceedings - 2015 IEEE Winter Conference on Applications of Computer Vision, WACV 2015*, 494–501. <https://doi.org/10.1109/WACV.2015.72>
- Schenk, U., Frascoli, M., Proietti, M., Geffers, R., Traggi, E., Buer, J., Ricordi, C., Westendorf, A. M., & Grassi, F. (2011). ATP inhibits the generation and function of regulatory T cells through the activation of purinergic P2X receptors. *Science Signaling*, 4(162), 1–12. <https://doi.org/10.1126/scisignal.2001270>
- Schenk, U., Westendorf, A. M., Radaelli, E., Casati, A., Ferro, M., Fumagalli, M., Verderio, C., Buer, J., Scanziani, E., & Grassi, F. (2008). Purinergic control of T cell activation by ATP released through pannexin-1 hemichannels. *Science Signaling*, 1(39), 1–14. <https://doi.org/10.1126/scisignal.1160583>
- Schwaller, B. (2020). Cytosolic Ca²⁺ buffers are inherently Ca²⁺ signal modulators. *Cold Spring Harbor Perspectives in Biology*, 12(1). <https://doi.org/10.1101/cshperspect.a035543>
- Schwiebert, E. M., & Zsembery, A. (2003). Extracellular ATP as a signaling molecule for epithelial cells. *Biochimica et Biophysica Acta - Biomembranes*, 1615(1–2), 7–32. [https://doi.org/10.1016/S0005-2736\(03\)00210-4](https://doi.org/10.1016/S0005-2736(03)00210-4)
- Sheng, D., & Hattori, M. (2022). Recent progress in the structural biology of P2X receptors. *Proteins: Structure, Function, and Bioinformatics*, January, 1–7. <https://doi.org/10.1002/prot.26302>
- Siebert, A. P., Ma, Z., Grevet, J. D., Demuro, A., Parker, I., & Foskett, J. K. (2013). Structural and functional similarities of calcium homeostasis modulator 1 (CALHM1) ion channel with connexins, pannexins, and innexins. *Journal of Biological Chemistry*, 288(9), 6140–6153. <https://doi.org/10.1074/jbc.M112.409789>

References

- Sorge, R. E., Trang, T., Dorfman, R., Smith, S. B., Beggs, S., Ritchie, J., Austin, J. S., Zaykin, D. V., Meulen, H. Vander, Costigan, M., Herbert, T. A., Yarkoni-Abitbul, M., Tichauer, D., Livneh, J., Gershon, E., Zheng, M., Tan, K., John, S. L., Slade, G. D., Jordan, J., Woolf, C. J., Peltz, G., Maixner, W., Diatchenko, L., Seltzer, Z., Salter, M. W., & Mogil, J. S. (2012). Genetically determined P2X7 receptor pore formation regulates variability in chronic pain sensitivity. *Nature Medicine*, *18*(4), 595–599. <https://doi.org/10.1038/nm.2710>
- Sparagna, G. C., Gunter, K. K., Sheu, S. S., & Gunter, T. E. (1995). Mitochondrial calcium uptake from physiological-type pulses of calcium: A description of the rapid uptake mode. *Journal of Biological Chemistry*, *270*(46), 27510–27515. <https://doi.org/10.1074/jbc.270.46.27510>
- Stokes, L., Scurrah, K., Ellis, J. A., Cromer, B. A., Skarratt, K. K., Gu, B. J., Harrap, S. B., & Wiley, J. S. (2011). A loss-of-function polymorphism in the human P2X4 receptor is associated with increased pulse pressure. *Hypertension*, *58*(6), 1086–1092. <https://doi.org/10.1161/HYPERTENSIONAHA.111.176180>
- Sugiyama, T., Kawamura, H., Yamanishi, S., Kobayashi, M., Katsumura, K., & Puro, D. G. (2005). Regulation of P2X7-induced pore formation and cell death in pericyte-containing retinal microvessels. *American Journal of Physiology - Cell Physiology*, *288*(3 57-3), 568–576. <https://doi.org/10.1152/ajpcell.00380.2004>
- Taruno, A. (2018). ATP release channels. *International Journal of Molecular Sciences*, *19*(3). <https://doi.org/10.3390/ijms19030808>
- Tay, A. (2020). The Benefits of Going Small: Nanostructures for Mammalian Cell Transfection. *ACS Nano*, *14*(7), 7714–7721. <https://doi.org/10.1021/acsnano.0c04624>
- Taylor, K. A., Wright, J. R., & Mahaut-Smith, M. P. (2015). Regulation of Pannexin-1 channel activity. *Biochemical Society Transactions*, *43*, 502–507. <https://doi.org/10.1042/BST20150042>
- Thunberg, U., Tobin, G., Johnson, A., Söderberg, O., Padyukov, L., Hultdin, M., Klareskog, L., Enblad, G., Sundström, C., Roos, G., & Rosenquist, R. (2002). Polymorphism in the P2X7 receptor gene and survival in chronic lymphocytic leukaemia. *Lancet*, *360*(9349), 1935–1939. [https://doi.org/10.1016/S0140-6736\(02\)11917-9](https://doi.org/10.1016/S0140-6736(02)11917-9)
- Tittle, R. K., & Hume, R. I. (2008). Opposite effects of zinc on human and rat P2X2 receptors. *Journal of Neuroscience*, *28*(44), 11131–11140. <https://doi.org/10.1523/JNEUROSCI.2763-08.2008>
- Tokunaga, A., Tsukimoto, M., Harada, H., Moriyama, Y., & Kojima, S. (2010). Involvement of SLC17A9-dependent vesicular exocytosis in the mechanism of ATP release during T cell activation. *Journal of Biological Chemistry*, *285*(23), 17406–17416.

References

- <https://doi.org/10.1074/jbc.M110.112417>
- Trabanelli, S., Očadlíková, D., Gulinelli, S., Curti, A., Salvestrini, V., de Paula Vieira, R., Idzko, M., Di Virgilio, F., Ferrari, D., & Lemoli, R. M. (2012). Extracellular ATP Exerts Opposite Effects on Activated and Regulatory CD4⁺ T Cells via Purinergic P2 Receptor Activation. *The Journal of Immunology*, *189*(3), 1303–1310. <https://doi.org/10.4049/jimmunol.1103800>
- Trebak, M., & Kinet, J. P. (2019). Calcium signalling in T cells. *Nature Reviews Immunology*, *19*(3), 154–169. <https://doi.org/10.1038/s41577-018-0110-7>
- Tsien, R. Y. (1981). A non-disruptive technique for loading calcium buffers and indicators into cells. *Nature*, *290*(5806), 527–528. <https://doi.org/10.1038/290527a0>
- Ursu, D., Ebert, P., Langron, E., Ruble, C., Munsie, L., Zou, W., Fijal, B., Qian, Y. W., McNearney, T. A., Mogg, A., Grubisha, O., Merchant, K., & Sher, E. (2014). Gain and loss of function of P2X7 receptors: Mechanisms, pharmacology and relevance to diabetic neuropathic pain. *Molecular Pain*, *10*(1), 1–11. <https://doi.org/10.1186/1744-8069-10-37>
- Vaeth, M., & Feske, S. (2018). Ion channelopathies of the immune system. *Current Opinion in Immunology*, *52*, 39–50. <https://doi.org/10.1016/j.coi.2018.03.021>
- Vandenbeuch, A., Anderson, C. B., & Kinnamon, S. C. (2015). Mice lacking pannexin 1 release ATP and respond normally to all taste qualities. *Chemical Senses*, *40*(7), 461–467. <https://doi.org/10.1093/chemse/bjv034>
- Vial, C., Tobin, A. B., & Evans, R. J. (2004). G-protein-coupled receptor regulation of P2X1 receptors does not involve direct channel phosphorylation. *Biochemical Journal*, *382*(1), 101–110. <https://doi.org/10.1042/BJ20031910>
- Vig, M., & Kinet, J. P. (2009). Calcium signaling in immune cells. *Nature Immunology*, *10*(1), 21–27. <https://doi.org/10.1038/ni.f.220>
- Von Kügelgen, I., & Hoffmann, K. (2016). Pharmacology and structure of P2Y receptors. *Neuropharmacology*, *104*, 50–61. <https://doi.org/10.1016/j.neuropharm.2015.10.030>
- Vultaggio-Poma, V., Sarti, A. C., & Di Virgilio, F. (2020). Extracellular ATP: A Feasible Target for Cancer Therapy. *Cells*, *9*(11). <https://doi.org/10.3390/cells9112496>
- Wallace, W., Schaefer, L. H., & Swedlow, J. R. (2001). A workingperson's guide to deconvolution in light microscopy. *BioTechniques*, *31*(5), 1076–1097. <https://doi.org/10.2144/01315bi01>
- Wang, C. M., Ploia, C., Anselmi, F., Sarukhan, A., & Viola, A. (2014). Adenosine triphosphate acts as a paracrine signaling molecule to reduce the motility of T cells. *The EMBO Journal*, *33*(12), 1354–1364. <https://doi.org/10.15252/embj.201386666>
- Wang, J., Ma, M., Locovei, S., Keane, R. W., & Dahl, G. (2007). Modulation of membrane channel currents by gap junction protein mimetic peptides: Size matters. *American*

References

- Journal of Physiology - Cell Physiology*, 293(3). <https://doi.org/10.1152/ajpcell.00097.2007>
- Wang, Y., Martins, I., Ma, Y., Kepp, O., Galluzzi, L., & Kroemer, G. (2013). Autophagy-dependent ATP release from dying cells via lysosomal exocytosis. *Autophagy*, 9(10), 1624–1625. <https://doi.org/10.4161/auto.25873>
- Wang, Y., Tao, A., Vaeth, M., & Feske, S. (2020). Calcium regulation of T cell metabolism. *Current Opinion in Physiology*, 17(3), 207–223. <https://doi.org/10.1016/j.cophys.2020.07.016>
- Wange, R. L. (2000). LAT, the linker for activation of T cells: a bridge between T cell-specific and general signaling pathways. *Science's STKE: Signal Transduction Knowledge Environment*, 2000(63), 1–14. <https://doi.org/10.1126/stke.2000.63.re1>
- Weigert, M., Schmidt, U., Boothe, T., Müller, A., Dibrov, A., Jain, A., Wilhelm, B., Schmidt, D., Broaddus, C., Culley, S., Rocha-Martins, M., Segovia-Miranda, F., Norden, C., Henriques, R., Zerial, M., Solimena, M., Rink, J., Tomancak, P., Royer, L., Jug, F., & Myers, E. W. (2018). Content-aware image restoration: pushing the limits of fluorescence microscopy. *Nature Methods*, 15(12), 1090–1097. <https://doi.org/10.1038/s41592-018-0216-7>
- Wiley, J. S., Dao-Ung, L. P., Gu, B. J., Sluyter, R., Shemon, A. N., Li, C., Taper, J., Gallo, J., & Manoharan, A. (2002). A loss-of-function polymorphic mutation in the cytolytic P2X7 receptor gene and chronic lymphocytic leukaemia: A molecular study. *Lancet*, 359(9312), 1114–1119. [https://doi.org/10.1016/S0140-6736\(02\)08156-4](https://doi.org/10.1016/S0140-6736(02)08156-4)
- Woehrle, T., Yip, L., Elkhail, A., Sumi, Y., Chen, Y., Yao, Y., Insel, P. A., & Junger, W. G. (2010). Pannexin-1 hemichannel-mediated ATP release together with P2X1 and P2X4 receptors regulate T-cell activation at the immune synapse. *Blood*, 116(18), 3475–3484. <https://doi.org/10.1182/blood-2010-04-277707>
- Woelk, L. M., Kannabiran, S. A., Brock, V. J., Gee, C. E., Lohr, C., Guse, A. H., Diercks, B. P., & Werner, R. (2021). Time-Dependent Image Restoration of Low-SNR Live-Cell Ca²⁺ Fluorescence Microscopy Data. *International Journal of Molecular Sciences*, 22(21), 11792. <https://doi.org/10.3390/ijms222111792>
- Wolf, I. M. A., Diercks, B. P., Gattkowski, E., Czarniak, F., Kempinski, J., Werner, R., Schetelig, D., Mittrücker, H. W., Schumacher, V., Von Osten, M., Lodygin, D., Flügel, A., Fliegert, R., & Guse, A. H. (2015). Frontrunners of T cell activation: Initial, localized Ca²⁺ signals mediated by NAADP and the type 1 ryanodine receptor. *Science Signaling*, 8(398), 1–13. <https://doi.org/10.1126/scisignal.aab0863>
- Wucherpennig, K. W., Gagnon, E., Call, M. J., Huseby, E. S., & Call, M. E. (2010). Structural biology of the T-cell receptor: insights into receptor assembly, ligand recognition, and

References

- initiation of signaling. *Cold Spring Harbor Perspectives in Biology*, 2(4), 1–14. <https://doi.org/10.1101/cshperspect.a005140>
- Yip, L., Woehrle, T., Corriden, R., Hirsh, M., Chen, Y., Inoue, Y., Ferrari, V., Insel, P. A., & Junger, W. G. (2009). Autocrine regulation of T-cell activation by ATP release and P2X7 receptors. *The FASEB Journal*, 23(6), 1685–1693. <https://doi.org/10.1096/fj.08-126458>
- Yoshida, H., Nishina, H., Takimoto, H., Marengère, L. E. M., Wakeham, A. C., Bouchard, D., Kong, Y. Y., Ohteki, T., Shahinian, A., Bachmann, M., Ohashi, P. S., Penninger, J. M., Crabtree, G. R., & Mak, T. W. (1998). The transcription factor NF-ATc1 regulates lymphocyte proliferation and Th2 cytokine production. *Immunity*, 8(1), 115–124. [https://doi.org/10.1016/S1074-7613\(00\)80464-1](https://doi.org/10.1016/S1074-7613(00)80464-1)
- Young, I. T. (1989). Image Fidelity: Characterizing the Imaging Transfer Function. *Methods in Cell Biology*, 30(C), 1–45. [https://doi.org/10.1016/S0091-679X\(08\)60974-7](https://doi.org/10.1016/S0091-679X(08)60974-7)
- Zahiri, D., Burow, P., Großmann, C., Müller, C. E., Klapperstück, M., & Markwardt, F. (2021). Sphingosine-1-phosphate induces migration of microglial cells via activation of volume-sensitive anion channels, ATP secretion and activation of purinergic receptors. *Biochimica et Biophysica Acta - Molecular Cell Research*, 1868(2). <https://doi.org/10.1016/j.bbamcr.2020.118915>
- Zamaraeva, M. V., Sabirov, R. Z., Maeno, E., Ando-Akatsuka, Y., Bessonova, S. V., & Okada, Y. (2005). Cells die with increased cytosolic ATP during apoptosis: A bioluminescence study with intracellular luciferase. *Cell Death and Differentiation*, 12(11), 1390–1397. <https://doi.org/10.1038/sj.cdd.4401661>
- Zeng, L., Palaia, I., Šarić, A., & Su, X. (2021). Plcy1 promotes phase separation of t cell signaling components. *Journal of Cell Biology*, 220(6). <https://doi.org/10.1083/jcb.202009154>
- Zhang, L., Xu, H., Jie, Y., Gao, C., Chen, W., Yin, S., Samways, D. S. K., & Li, Z. (2014). Involvement of Ectodomain Leu 214 in ATP binding and channel desensitization of the P2X4 receptor. *Biochemistry*, 53(18), 3012–3019. <https://doi.org/10.1021/bi401711n>
- Zhang, X., Zhao, W., Zhao, Y., Zhao, Z., Lv, Z., Zhang, Z., Ren, H., Wang, Q., Liu, M., Qian, M., Du, B., & Qin, J. (2021). Inflammatory macrophages exacerbate neutrophil-driven joint damage through ADP/P2Y1 signaling in rheumatoid arthritis. *Science China Life Sciences*. <https://doi.org/10.1007/s11427-020-1957-8>
- Zheng, L., Stathopoulos, P. B., Schindl, R., Li, G. Y., Romanin, C., & Ikura, M. (2011). Auto-inhibitory role of the EF-SAM domain of STIM proteins in store-operated calcium entry. *Proceedings of the National Academy of Sciences of the United States of America*, 108(4), 1337–1342. <https://doi.org/10.1073/pnas.1015125108>
- Ziegler, S. F., Ramsdell, F., & Alderson, M. R. (1994). The activation antigen CD69. *Stem*

References

Cells, 12(5), 456–465. <https://doi.org/10.1002/stem.5530120502>

Figure Index

Figure 1.1	Illustration of TCR stimulation_____	2
Figure 1.2	Ca ²⁺ signaling in T cells_____	5
Figure 1.3	Purinergic signaling cascade_____	8
Figure 1.4	P2X monomer structure_____	10
Figure 1.5	Purinergic signaling after TCR/CD3 stimulation_____	13
Figure 1.6	Excitation spectra for 1 μ M Fura-2_____	14
Figure 1.7	Point-spread-function_____	15
Figure 3.1	Spatial image patterns were captured better by the “entropy-like” deconvolution algorithm (ER-Decon)_____	53
Figure 3.2	Extracellular orthosteric binding site _____	57

Oral and Poster Presentations

Brock VJ, Wolf IMA, Rissiek B, ER-Lukowiak M, Koch-Nolte F, Stähler T, Müller CE, Woelk LM, Werner R, Guse AH, Diercks BP (2021) P2X4 and P2X7 are essential players in basal T cell activity and Ca²⁺ signaling milliseconds after T cell activation. *The 2nd junior European Calcium Society meeting - Calcium research across kingdoms*, November 2021, virtual

Brock VJ, Wolf IMA, Rissiek B, ER-Lukowiak M, Koch-Nolte F, Stähler T, Müller CE, Woelk LM, Werner R, Guse AH, Diercks BP (2021) P2X4 and P2X7 are essential players in basal T cell activity and Ca²⁺ signaling milliseconds after T cell activation. *FASEB SRC - Calcium and Cell Function*, October 2021, virtual

Brock VJ, Wolf IMA, Rissiek B, Werner R, Koch-Nolte F, Guse AH, Diercks BP (2021) P2X4 and P2X7 are essential players in basal T cell activity and Ca²⁺ signaling milliseconds after T cell activation. *74th Annual Meeting of the Society of General Physiologists Ion Channels & Transporters in Immunity, Inflammation & Antitumor Immunity*, September 2021, virtual

Brock VJ, Wolf IMA, Rissiek B, ER-Lukowiak M, Koch-Nolte F, Stähler T, Müller CE, Woelk LM, Werner R, Guse AH, Diercks BP (2021) Purinergic cation channels P2X4 and P2X7 amplify the formation of initial Ca²⁺ microdomains in T cells. *FASEB SRC - The NAD⁺ Metabolism and Signaling Conference*, June 2021, virtual

Brock VJ, Diercks BP, Rissiek B, Koch-Nolte F, Tolosa E, Werner R, Guse AH, Wolf IMA (2020) Role of P2X4 and P2X7 cation channels in the formation of Ca²⁺ microdomains in T cells. *EMBO Symposium - Calcium signaling: Molecular mechanisms to role in health and diseases*, January 2020, Bangalore India

Eidesstattliche Versicherung

Eidesstattliche Versicherung

Name: Brock

Vorname: Valerie Johanna

Hiermit erkläre ich an Eides statt, dass ich die vorliegende Dissertationsschrift selbst verfasst und keine anderen als die angegebenen Quellen und Hilfsmittel benutzt habe.

Hamburg, 04.10.2022

Ort, Datum

U. Brock

Unterschrift

Acknowledgements

First of all, I would like to thank Prof. Dr. Andreas H. Guse for the opportunity to join his fabulous research group for the time-course of my PhD. I thank him for the numerous productive discussions during our Friday meetings, the scientific and technical exchange of ideas and the tireless motivation to finish my thesis successfully.

My special thanks go to my PI and supervisor Dr. Björn-Philipp Diercks, who provided me with the exciting project and gave me the opportunity to join the highly collaborative SFB1328 project, which was essential for the success of my research project. I thank him for his kind support, the scientific and experimental discussions and the guidance throughout my thesis.

I would like to thank Prof. Dr. Eva Tolosa for evaluating my thesis and for coordinating the integrated research training group (IRTG) of the SFB1328, which offered me the chance to participate in different workshops and present my research project at international conferences.

I would also like to thank our collaboration partners from the project A02 of the SFB1328, Dr. René Werner and Dr. Lena-Marie Woelk, from the Department of Computational Neuroscience of the UKE, which offered their expertise in computational data analysis and programming to improve our analysis-workflow and resolution of the images.

Moreover, I would like to thank Dr. Björn Rissiek from the Department of Neurology of the UKE for the provision with spleens of P2X-KO and WT Balb/C mice and his always thoughtful experimental advice.

I also thank the whole SFB1328, particularly our collaborators from the Department of Immunology of the UKE and the Department of Pharmacy of the University of Bonn, who provided me with compounds, nanobodies and their know-how to finish my research project successfully.

Special thanks go to the whole great Calcium Signaling Group for the very motivating and good working atmosphere. Especially, I thank my colleagues and good friends Lola Hernandez, Mariella Weiß, Franziska Möckl, Frederike Kulow and Friedericke Bönisch for their friendship, the fun we had and the support at any time that made the time-course of my PhD fly by.

Last but not least, I would like to thank my family, especially my mother, Annette Brock, my father, Dr. Ulrich Brock, my sisters, Dr. Ann-Cathrin Brock and Julie Brock, and my brother, Cornelius Brock, as well as my partner Tim Kozok. I am so happy to have you all by my side. Thank you for your unrestricted love, moral support and for the fantastic and wonderful moments we had and will have.

Erklärung

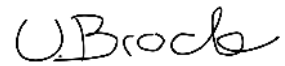
Ich versichere, dass dieses gebundene Exemplar der Dissertation und das in elektronischer Form eingereichte Dissertationsexemplar (über den Docata-Upload) und das bei der Fakultät (zuständiges Studienbüro bzw. Promotionsbüro Biologie) zur Archivierung eingereichte gedruckte gebundene Exemplar der Dissertationsschrift identisch sind.

Hamburg, 04.10.2022

Ort, Datum

Valerie Brock

Vorname Nachname, Unterschrift

Handwritten signature of Valerie Brock in black ink, written in a cursive style.